

Dissertation zur Erlangung des Doktorgrades
der Fakultät für Chemie und Pharmazie
der Ludwig-Maximilians-Universität München

Increasing the chemical diversity of MAX phases

Tobias Reinhold Rackl

aus

Lauf a. d. Pegnitz, Deutschland

2020

Erklärung

Diese Dissertation wurde im Sinne von §7 der Promotionsordnung vom 28. November 2011 von Herrn Prof. Dr. Dirk Johrendt betreut.

Eidesstattliche Versicherung

Diese Dissertation wurde eigenständig und ohne unerlaubte Hilfsmittel erarbeitet.

München, 18.06.2020

Tobias Rackl

Dissertation eingereicht am:	16.04.2020
1. Gutachter:	Prof. Dr. Dirk Johrendt
2. Gutachter:	PD Dr. Constantin Hoch
Mündliche Prüfung am:	26.05.2020

“If you try and take a cat apart to see how it works, the first thing you have on your hands is a non-working cat.”

— *Douglas Adams*

Danksagung

Mein erster Dank gilt Prof. Dr. Dirk Johrendt für die Betreuung und Finanzierung meiner Doktorarbeit. Besonders dankbar bin ich für die Möglichkeit meine Dissertation frei selbst zu gestalten und sie so zu meiner Eigenen zu machen.

PD Dr. Constantin Hoch danke ich für die spontane Übernahme des Zweitgutachtens und das Interesse an meiner Forschung. Für die Vervollständigung meiner Prüfungskommission danke ich außerdem Prof. Dr. Stefan Schwarzer, Prof. Dr. Thomas M. Klapötke, Prof. Dr. Konstantin Karaghiosoff und Prof. Dr. Achim Hartschuh.

Außerdem möchte ich allen AnalytikerInnen, Feinmechanikern und GalsbläserInnen des Departments danken, die durch ihre Servicemessungen und über Jahre erworbene Kompetenz die Forschung am Campus ermöglichen und verbessern. Ich danke Robin Niklaus für diverse DFT Rechnungen inklusive deren Interpretation und Lucien Eisenburger für die Durchführung und Auswertung von STEM Messungen. Danke Arthur für die Aufnahme zahlreicher Pulverdiffraktogramme am Einkristalldiffraktometer.

Meinen PraktikantInnen Micheal Gruhne, Josef Baumann, Dominik Werhahn, Benedikt Söldner und Martina Pfeiffer bin ich sehr dankbar für ihre fleißige Unterstützung, ihren Eifer, ihre Ideen und Fragen.

Für das Korrekturlesen dieser Dissertation bedanke ich mich bei Juliane Stahl, Bettina Rendenbach, Valentin Weippert, Arthur Haffner, Simon Kloß und Sebastian Vogel. Vielen Dank für eure konstruktiven Verbesserungsvorschläge.

Ich bedanke mich bei allen Mitgliedern des AK Johrendts die ich in den vergangenen Jahren kennenlernen durfte und die den Arbeitsalltag stets bereichert haben: Erwin Wiesenmayer, Christine Stürzer, Franziska Hummel, Roman Pobel, Ursula Pachmayr, Simon Pescke, Rudolf Schönmann, Catrin Löhnert, Juliane Stahl, Arthur Haffner, Bettina Rendenbach, Valentin Weippert und Marlo Schöneich. Danke Ursi, Juliane und Simon, dass ihr mich so toll im Labor aufgenommen habt und ich mich von Beginn an wohlfühlt habe. Danke Ursi für deine stets gute Laune. Danke Simon für deinen ausgezeichneten Musikgeschmack. Danke Juliane für Alles, ohne dich wäre die Zeit nur halb so schön, meine Grafiken hässlich und meine Nachmittage sehr einsam gewesen. Danke Muddi, dass du diesen Laden zusammenhältst und man bei dir immer eine offene Tür findet. Danke Arthur, dass du über alles Lachen kannst. Danke Betti für deine Freundschaft, schöne Pausen und dein Talent Sätze zu beenden.

Außerdem danke ich allen Mitgliedern der Arbeitskreise Schnick, Lotsch und Hoch die ich während meiner Zeit kennengelernt habe für eine tolle Arbeitsatmosphäre auf dem gesamten Stockwerk, für die schönen Erlebnisse und zahlreichen Freundschaften. Danke Tobi, dass ich deinen HF-Ofen so oft verwenden durfte. Danke Sebi für die mittäglichen Fußballstunden. Danke DJ Mad Malle für herausragende Musik.

Ein besonderer Dank geht an alle Mitglieder der WYB: Niklas, Vera, Juri, Steffi, Alan, Nisi, Ralf, Elli, Peter, Lara, Fion, Sinah, Flo, Michi und David. Danke für legendäre Urlaube, für zahlreiche Stunden an Seen, im Westpark oder an der Isar, für unvergessliche Abende, für unterhaltsame Semsteressen und besonders für eure Freundschaft auf die man sich immer verlassen kann.

Meiner Familie danke ich für den Rückhalt, die Unterstützung und Geborgenheit in meinen Leben. Danke Mama, dass du immer für mich da bist und stets an mich glaubst. Deine Offenheit und Toleranz gegenüber allen Menschen haben mich sehr geprägt und mir viele Freundschaften beschert. Danke Papa, dass du mir so viel beigebracht hast. Dir verdanke ich mein handwerkliches Geschick und mein Interesse an der Wissenschaft. Danke Sebbi, dass du als großer Bruder genauso bist wie du zu sein hast. Ich danke meinen Omas, Helga und Paula, für ihre Unterstützung und dafür, dass sie immer stolz auf mich sind.

Zuletzt möchte ich Lara, meiner Freundin, Verlobten und bald Frau danken. Du warst das gesamte Studium über an meiner Seite, hast mich unterstützt, mit mir gelitten, dich mit mir gefreut, viele tolle Reisen unternommen, schöne Konzerte besucht, entspannte Abende verbracht und die gesamte Zeit unschätzbar bereichert. Danke für Alles!

Table of Contents

1	Introduction	1
2	MAX phase borides.....	11
2.1	Syntheses and physical properties of the MAX phase boride Nb ₂ SB and the solid solutions Nb ₂ SB _x C _{1-x} ($x = 0 - 1$)	11
2.2	The MAX phase borides Zr ₂ SB and Hf ₂ SB.....	25
2.3	Further MAX phase borides – the solid solutions Nb ₂ A(B,C) (A = As, In, Sn)	35
3	M and A site substitutions in MAX phases	51
4	Intercalated MAX phases M ₃ P ₂ C (M = Nb, Ta)	67
5	Summary	75
6	Conclusion.....	79
A	Appendix	81
A. 1	Crystallographic data, Rietveld refinement, magnetization measurements and phonon DOS of Nb ₂ SB _x C _{1-x} ($x = 0 - 1$).....	82
A. 2	Crystallographic data and Rietveld refinement of Nb ₂ A(B,C) (A = As, In, Sn).....	88
A. 3	Starting materials, crystallographic data and Rietveld refinement of M ₂ A _x A' _{1-x} C (M = V, Nb; A, A' = In, Ge, Sn, P, As, S) and (V _x Nb _{1-x}) ₂ SC.....	94
A. 4	Rietveld refinement and magnetic measurements of M ₃ P ₂ C (M = Nb, Ta)	117

1 Introduction

“Graphene is a single plane of graphite that has to be pulled out of bulk graphite to show its amazing properties.”^[1] As simple as these words of the Noble prize winner Andre Geim sound, the synthesis of graphene was a big challenge for a long time. In 1962, Hanns-Peter Böhm reported about the adsorption behavior of thin carbon sheets.^[2] He also established the name graphene, but he did not achieve the synthesis of very thin layers.^[3] It was Andre Geim and Konstantin Novoselov, who first prepared graphene by the scotch tape method in 2004.^[4-5] This discovery resulted in a worldwide increase in research on two-dimensional materials. Especially since these often show a significantly different behavior compared to the corresponding 3D materials. The properties of two-dimensional materials have the potential to revolutionize technologies in energy conversion and storage, healthcare, spaceflight, information and communication (ICTs) and many more. Over the past 16 years, immense knowledge and various patents on two-dimensional materials were written. However, there are still very few commercial applications that are limited to graphene, such as touch screens or sports equipment like bicycle helmets and tennis rackets.^[6] To expand the field of application of two-dimensional materials, the investigation of further new compounds, and thus the increase of knowledge about them, is indispensable.

Which materials are to be considered as two-dimensional needs to be clarified first. A real two-dimensional layer cannot exist, since every layer of atoms has a certain thickness. Consequently, one can only approximate this state, and therefore such compounds are better described as quasi-two-dimensional or periodic in two non-collinear directions. Furthermore, a distinction is made between a quasi-two-dimensional crystal structure and the anisotropy of physical properties. A compound with a three-dimensional crystal structure can indeed exhibit properties only within a plane, such as electrical conductivity or mechanical behavior. For the emergence of the anisotropy, however, different types of bonds within the crystal structure are necessary.^[7-9] On the one hand, metal-metal bonds within a plane can cause an anisotropy of electrical and thermal conductivity, like in the layered MAX phases. On the other hand, decisive for the lubricity of graphite is the difference between the bond strength within the honeycomb network and the weak van der Waals (vdW) interaction between the layers. This leads to numerous applications such as in pencils or as lubricant in industry and is finally crucial for the existence of graphene, which is produced by the scotch tape method.^[10] A tape is stuck onto a piece of graphite, whereby a few micrometers thick layer of graphene forms during the peeling process. This process can be repeated to build very thin layers and finally graphene.^[4]

Several other so-called vdW layered materials are known, which can be transferred into quasi-two-dimensional compounds by mechanical exfoliation.^[11-12] Some of the three-dimensional vdW compounds have been known for a long time, but came back into the limelight since the discovery of the unique physical properties of graphene. Well studied examples of quasi-two-dimensional vdW materials are silicene^[13-14], borene^[15], black phosphorus (BP)^[16], h-BN^[17], transition metal oxides (MO_3)^[18], chalcogenides (MCh , MCh_2 , MCh_3 , M_2Ch_3)^[19-20] and halides (MH , MH_2 , MH_3)^[21-22], where M stands for various transition metals ($M = \text{Ti, Zr, Hf, V, Nb, Ta, Cr, Mo, W, Mn, Fe, Ru, Co, Ni, Pt and Cd}$), Ch for chalcogens ($Ch = \text{S, Se and Te}$) and H for halides ($H = \text{Cr, Br and I}$). Figure 1-1 characterize some of them utilizing the crystal structure. Exfoliation by the scotch tape method has some drawbacks, since the monolayers can be damaged and are limited by size. Therefore, chemical vapor deposition (CVD) is used to synthesize sheets with high quality and a relatively large surface. However, this method was only investigated for a few of these phases, for example, graphene and transition metal dichalcogenides (TMDC).^[23-25]

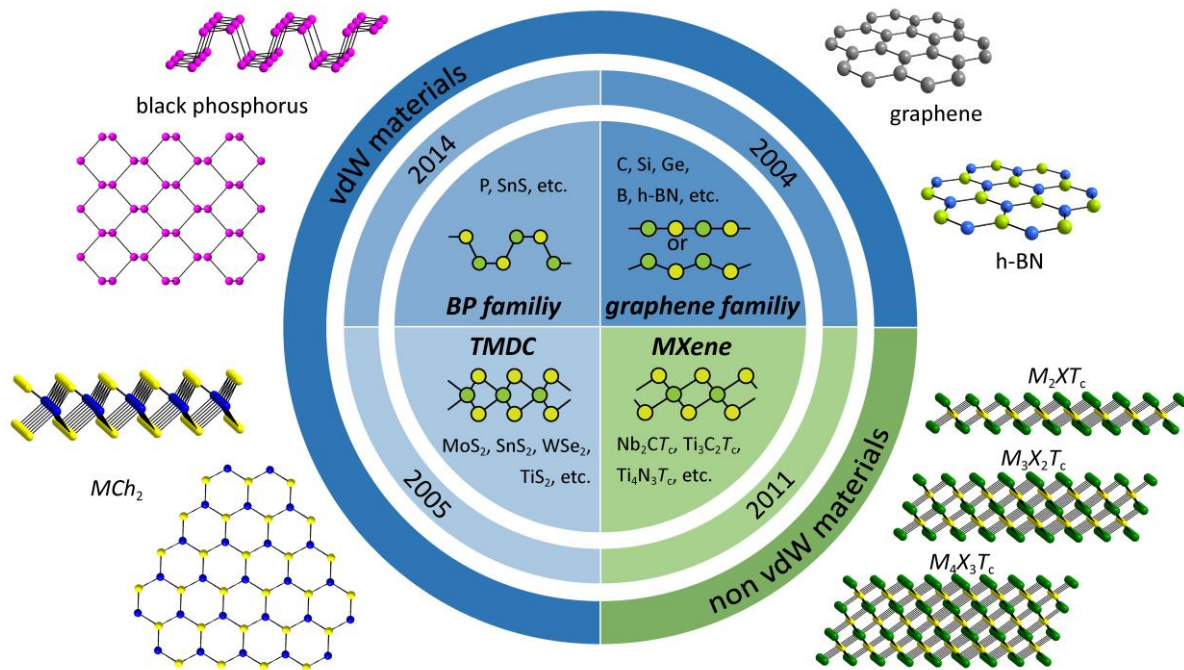


Figure 1-1: Overview of two-dimensional materials classified by the crystal structure of the monolayers, including the year of the first synthesis of a monolayer in this group and the classification to vdW materials.

Another group of quasi-two-dimensional compounds, which are no vdW materials, are the MXenes. These are compounds with the general formula $M_{n+1}X_nT_c$, in which M is an early transition metal (see Figure 1-2 green), X is carbon or nitrogen (see Figure 1-2 yellow), and T_c represents the surface termination (for example O, OH, F or Cl). Since the synthesis of the first

MXene ($Ti_3C_2T_c$) in 2011, the family is growing fast.^[26] They consist of layers of edge-sharing M_6X octahedra. The $M_{n+1}X_nT_c$ quasi-two-dimensional structure features a single layer of octahedra for $n = 1$, a double for $n = 2$, and a triple for $n = 3$ (see Figure 1-1). T_c terminates the metal surface.^[27-30] These materials show good electrical conductivities, stabilities, and large specific surfaces. Due to these properties, they are potential candidates for various applications like energy storage and conversion, catalytic degradation, photothermal treatment, biomedical applications, and environmental adsorption.^[31-35] Thereby they benefit from the possibility of surface modification by exchanging T_c . However, 70 % of the research in MXenes has focused on the first discovered compound, $Ti_3C_2T_c$.^[29] Figure 1-2 shows the already incorporated elements in MXenes. Considering this diversity and the different layer thicknesses n , the properties of these phases can easily be tuned and adjusted. Therefore, the application potential of these phases is evident. Despite similar properties and structure, MXenes are not vdW materials and, thus, cannot be mechanically exfoliated. The most common synthesis route for these phases is the etching of the A element starting from MAX phases.

MAX																		MXenes																																			
$M_{n+1}AX_n$																		$M_{n+1}X_nT_c$																																			
1	H																	2	He	5	B	6	C	7	N	8	O	9	F	10	Ne																						
3	Li	4	Be															13	Al	14	Si	15	P	16	S	17	Cl	18	Ar																								
11	Na	12	Mg															19	K	20	Ca	21	Sc	22	Ti	23	V	24	Cr	25	Mn	26	Fe	27	Co	28	Ni	29	Cu	30	Zn	31	Ga	32	Ge	33	As	34	Se	35	Br	36	Kr
37	Rb	38	Sr	39	Y	40	Zr	41	Nb	42	Mo	43	Tc	44	Ru	45	Rh	46	Pd	47	Ag	48	Cd	49	In	50	Sn	51	Sb	52	Te	53	I	54	Xe																		
55	Cs	56	Ba	La	72	Hf	73	Ta	74	W	75	Re	76	Os	77	Ir	78	Pt	79	Au	80	Hg	81	Tl	82	Pb	83	Bi	84	Po	85	At	86	Rn																			
87	Fr	88	Ra	Ac	104	Rf	105	Db	106	Sg	107	Bh	108	Hs	109	Mt	110	Ds	111	Rg	112	Cn	113	Nh	114	Fl	115	Mc	116	Lv	117	Ts	118	Og																			
57	La	58	Ce	59	Pr	60	Nd	61	Pm	62	Sm	63	Eu	64	Gd	65	Tb	66	Dy	67	Ho	68	Er	69	Tm	70	Yb	71	Lu																								
89	Ac	90	Th	91	Pa	92	U	93	Np	94	Pu	95	Am	96	Cm	97	Bk	98	Cf	99	Es	100	Fm	101	Md	102	No	103	Lr																								




	M only in MAX		Element only in solid solution
	X only in MAX		

Figure 1-2: Periodic table of elements showing the known metals (green), A group elements, and X elements (yellow) in MAX phases. Stripes mark elements that have not been etched to MXenes. Elements only known in solid solutions are signed (blue).

In these phases, layers of M_6X octahedra alternate with layers of A elements, whereas the number of possible M elements is even greater than in MXenes. The variety of A elements further increases the diversity of these phases (see Figure 1-2). The MAX phases, or $M_{n+1}AX_n$, exhibit layered, hexagonal crystal structures ($P6_3/mmc$), where M and X form a single layer of M_6X octahedra for $n = 1$ (Cr_2AlC type), a double layer $n = 2$ (Ti_3SiC_2 type), and a triple layer for $n = 3$ (Ti_4GaC_3 type) (Figure 1-3). To date, ~ 87 and, considering solid solutions, ~ 165 MAX phases are known.^[36-38] Several of the ternary phases were already synthesized in the 1960s by Nowotny's group in Vienna (referred to H -phases at this time).^[39-44]

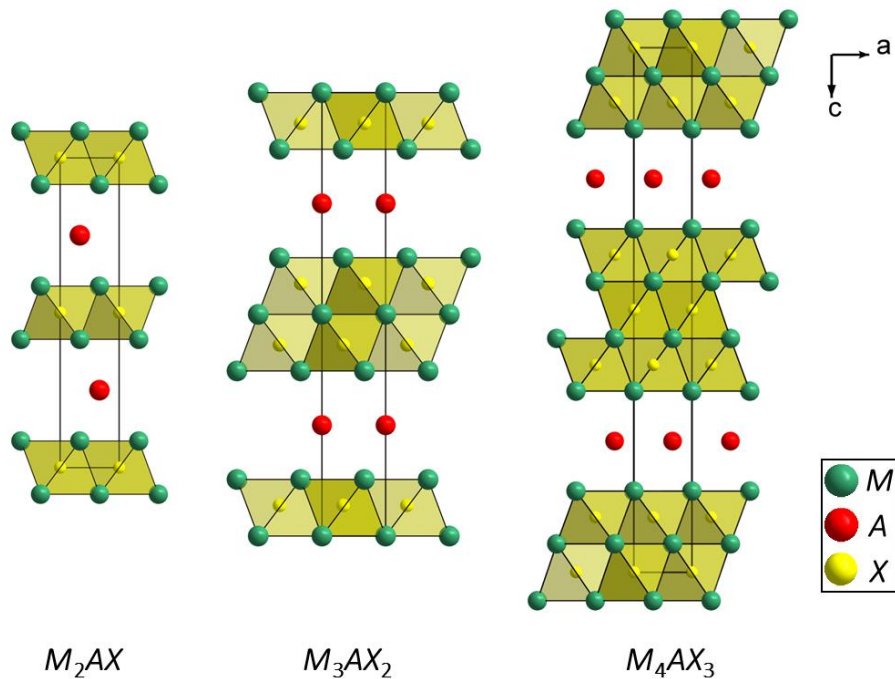


Figure 1-3: Crystal structure of $M_{n+1}AX_n$ in the hexagonal space group $P6_3/mmc$, 211-type (left), 312-type (middle) and 413-type (right).

However, they first came into limelight in 1996 when Barsoum and El-Raghy discovered their unique combination of metallic and ceramic properties.^[45] The $d-d$ orbital interaction of the metal atoms is dominant at the Fermi level. This results in a metallic behavior of the resistivity, while some of the MAX phases are even better conductors than the pure metals ($0.07 - 2 \mu\Omega\text{m}$ at rt).^[36, 46] For the same reason, they are good thermal conductors ($12 - 60 \text{WK}^{-1}\text{m}^{-1}$ at rt).^[47] They are easy to machine like metals, and at the same time, they deform by ripplocation nucleation applying external pressure, which in turn results in the formation of kink bands.^[48-50] Furthermore, they show a brittle to plastic transition at high temperatures, great damage and thermal shock tolerance, and are rather soft ($\text{VHN} = 1.4 - 8 \text{GPa}$). All MAX phases share these properties, but there are additional features that only occur in some of them. Certain compounds,

Ti_2AlC , Cr_2AlC , Ti_3SiC_2 , and Ti_3AlC_2 , are light, with densities $< 5 \text{ g}\cdot\text{cm}^{-3}$ and exhibit high stiffnesses, with Young's moduli $> 300 \text{ GPa}$ at the same time.^[51] Furthermore, Ti_3SiC_2 is fatigue-proof ($10 - 15 \text{ MPa}\cdot\text{m}^{0.5}$) and creep resistant.^[47, 52] Beyond that, some MAX phases can form protective layers. For example, compounds containing aluminum are particularly resistant to oxidation at high temperatures, due to Al_2O_3 passivation on the surface.^[53-56] Moreover, $\text{Nb}_2\text{Sn}(\text{B}, \text{C})$ builds a protective layer of Nb_3Sn in acidic environments which prevents further dissolution, as described in this thesis.

Altogether, the MAX phase family of early transition metal carbides and nitrides, is already extensive. Their unique combination of properties leads to several applications. Among them are protective coatings, sensors, microelectromechanical systems, electrical contacts, and especially high-temperature applications.^[57-59] They differ from other quasi-two-dimensional materials, especially by their chemical diversity and, therefore, by the possibility of tuning and creation of desired properties. Thus, the challenge of current research is to increase this diversity further and to investigate the resulting changed properties.

The first part of this thesis focuses on the investigation of boron as a new X element in MAX phases. A clear distinction must be made between MAX phase borides and the known so-called MAB phases. The latter show compositions and layered structures similar to MAX phases, but in contrast, the M_6B layers consist of edge-sharing trigonal prisms, and B — B bonds are formed. These layers alternate with layers of the A element, which is usually aluminum or silicon. The following structure types are known for MAB phases: Mn_2AlB_2 ($Cmmm$)^[60], MoAlB ($Cmcm$)^[61], Cr_3AlB_4 ($Immm$)^[62], Cr_4AlB_6 ($Cmmm$)^[63], Cr_4AlB_4 ($Immm$)^[64] and Ru_2ZnB_2 ($I4_1/amd$)^[65]. Similar to MAX phases, they exhibit high strengths, good thermal and electrical conductivity, and a pronounced anisotropy of the physical properties. Furthermore, the properties are comparable to those of the corresponding transition metal diborides, but the MAB phases show a significantly increased oxidation resistance due to the formation of Al_2O_3 protective layers. In addition, compared to carbides, the borides often show an increase in hardness and strength.^[66]

Although MAX borides were not synthesized yet, they have been theoretically predicted recently. Among them, most phases have negative formation enthalpies and, hence, should be synthesizable. Like the carbides and nitrides, they exhibit a combination of metallic and ceramic properties. The $d - d$ interaction of the metal atoms is dominant at the Fermi level and, therefore, reveal metallic behavior. Besides, calculations of the elastic constants show that the elastic properties can change significantly with the incorporation of boron.^[67-72] For example, V_2AlB is more ductile, and the compounds $M_2\text{AlB}$ ($M = \text{V}, \text{Nb}, \text{Ta}, \text{Cr}, \text{Mo}, \text{Zr}$) and Cr_2AB ($A = \text{Al}, \text{Si}, \text{P}$) are harder

than the corresponding carbides.^[67, 69-70] However, these trends cannot be transferred to all borides and, thus, need to be studied in more detail. The MAX phase borides are particularly promising materials for structural applications and wear-resistant coatings.

In this thesis, the syntheses of the first MAX phase borides are shown. These compounds increase the chemical diversity of the MAX phases and are the first candidates to investigate the changed properties compared to the carbides. The ternary 211 phases M_2SB ($M = \text{Zr, Hf, Nb}$), as well as the solid solutions $\text{Nb}_2\text{S}(\text{B,C})$ and $\text{Nb}_2\text{As}(\text{B,C})$, were synthesized. The change in crystal structure upon substitution of carbon by boron is discussed. The reduced absolute number of electrons in the borides shows a substantial impact on the M_6X octahedra. Besides structural changes, the effect on magnetic properties and resistivities is discussed.

The ability to form solid solutions has so far been realized in MAX phases mainly on the M and A site. This leads to magnetic properties by the incorporation of manganese or iron, for example, in $(\text{Cr,Mn})_2\text{AlC}$ or $(\text{V,Fe})_2\text{AlC}$.^[73-76] Furthermore, by A site substitution with palladium ($\text{Ti}_3(\text{Si,Pd})\text{C}_2$), copper ($\text{Ti}_3(\text{Al,Cu})\text{C}_2$), and bismuth ($\text{Zr}_2(\text{Al,Bi})\text{C}$), these elements were incorporated into the MAX phase family.^[77-79] The stoichiometric substitution of the M element can also result in ordered crystal structures both, in-plane (i -MAX phases) and out-of-plane (o -MAX phases), like in $(\text{Mo}_{2/3}\text{Sc}_{1/3})_2\text{AlC}$ and $(\text{Cr}_{2/3}\text{Ti}_{1/3})_3\text{AlC}_2$, respectively.^[80-81] Besides, solid solutions also form new MAX phase types, such as the 523-type $(\text{V}_{0.5}\text{Cr}_{0.5})_5\text{Al}_2\text{C}_3$ and the 514-type $(\text{Ti}_{0.5}\text{Nb}_{0.5})_5\text{AlC}_4$.^[38, 82-83]

Considering all these changes in solid solutions, the second part of this thesis analyzes the impact of substitution on niobium and vanadium MAX phases. In detail, the syntheses of several solid solutions $M_2A_xA'_{1-x}\text{C}$ ($M = \text{V, Nb}$; $A, A' = \text{In, Ge, Sn, P, As, S}$) and $(\text{V}_x\text{Nb}_{1-x})_2\text{SC}$ is described. Due to the stability of binary transition metal carbides and nitrides, the phase pure synthesis of MAX phases is often challenging. Thus, the systematic study of the synthesis of these solid solutions can show how high-quality samples can be produced. Besides, we approached V_2SC , which could not be produced until today, by substitution in the compounds $\text{V}_2(\text{P,S})\text{C}$, $\text{V}_2(\text{As,S})\text{C}$, and $(\text{V,Nb})_2\text{SC}$. Measurements of the susceptibility reveal the magnetic properties of the solid solutions.

The MAX phase family is still growing fast, which increase the diversity of properties, but also expands the structural diversity. Examples have already been shown above with the discovery of ordered crystal structures and the 514-, 523- and 615-type MAX phases.^[38, 82-84] In the last part of this thesis, the first intercalated MAX phases $M_3\text{P}_2\text{C}$ ($M = \text{Nb, Ta}$) are presented. They exhibit a new layer for MAX phases of $M_6\text{P}$ trigonal prisms and, therefore, increase their structural diversity. Magnetic and resistivity measurements reveal some physical properties of these compounds.

References

- [1] A. Geim, *Nature*, **2010**, doi:10.1038/news.2010.525.
- [2] H. P. Boehm, A. Clauss, G. O. Fischer, U. Hofmann, *Z. Anorg. Allg. Chem.* **1962**, *316*, 119-127.
- [3] V. Dhinakaran, M. Lavanya, K. Vigneswari, M. Ravichandran, M. D. Vijayakumar, *Materials Today: Proceedings* **2020**.
- [4] K. S. Novoselov, A. K. Geim, S. V. Morozov, D. Jiang, Y. Zhang, S. V. Dubonos, I. V. Grigorieva, A. A. Firsov, *Science* **2004**, *306*, 666.
- [5] A. K. Geim, *Phys. Scr.* **2012**, *T146*, 014003.
- [6] *2D materials applications*, <http://graphene.icfo.eu/> (accessed **20.02.2020**).
- [7] E. G. Tulsy, J. R. Long, *Chem. Mater.* **2001**, *13*, 1149-1166.
- [8] R. A. L. Morasse, T. Li, Z. J. Baum, J. E. Goldberger, *Chem. Mater.* **2014**, *26*, 4776-4780.
- [9] T. Li, J. E. Goldberger, *Chem. Mater.* **2015**, *27*, 3549-3559.
- [10] M. J. Allen, V. C. Tung, R. B. Kaner, *Chem. Rev.* **2010**, *110*, 132-145.
- [11] P. Ajayan, P. Kim, K. Banerjee, *Phys. Today* **2016**, *69*, 38-44.
- [12] D. L. Duong, S. J. Yun, Y. H. Lee, *ACS Nano* **2017**, *11*, 11803-11830.
- [13] A. J. Mannix, B. Kiraly, M. C. Hersam, N. P. Guisinger, *Nature Reviews Chemistry* **2017**, *1*, 0014.
- [14] A. Molle, J. Goldberger, M. Houssa, Y. Xu, S.-C. Zhang, D. Akinwande, *Nat. Mater.* **2017**, *16*, 163-169.
- [15] A. J. Mannix, X.-F. Zhou, B. Kiraly, J. D. Wood, D. Alducin, B. D. Myers, X. Liu, B. L. Fisher, U. Santiago, J. R. Guest, M. J. Yacamán, A. Ponce, A. R. Oganov, M. C. Hersam, N. P. Guisinger, *Science* **2015**, *350*, 1513.
- [16] M. Akhtar, G. Anderson, R. Zhao, A. Alruqi, J. E. Mroczkowska, G. Sumanasekera, J. B. Jasinski, *npj 2D Materials and Applications* **2017**, *1*, 5.
- [17] A. B. Preobrajenski, M. A. Nesterov, M. L. Ng, A. S. Vinogradov, N. Mårtensson, *Chem. Phys. Lett.* **2007**, *446*, 119-123.
- [18] G. C. Bond, S. Flamerz, R. Shukri, *Faraday Discussions of the Chemical Society* **1989**, *87*, 65-77.
- [19] T. Heine, *Acc. Chem. Res.* **2015**, *48*, 65-72.
- [20] K. Cho, J. Pak, S. Chung, T. Lee, *ACS Nano* **2019**, *13*, 9713-9734.
- [21] C. Huang, Y. Du, H. Wu, H. Xiang, K. Deng, E. Kan, *Phys. Rev. Lett.* **2018**, *120*, 147601.

- [22] M. A. McGuire, *Crystals* **2017**, *7*, 121.
- [23] J. G. Song, J. Park, W. Lee, T. Choi, H. Jung, C. W. Lee, S.-H. Hwang, J. M. Myoung, J. H. Jung, S.-H. Kim, C. Lansalot-Matras, H. Kim, *ACS Nano* **2013**, *7*, 11333-11340.
- [24] G. R. Bhimanapati, Z. Lin, V. Meunier, Y. Jung, J. Cha, S. Das, D. Xiao, Y. Son, M. S. Strano, V. R. Cooper, L. Liang, S. G. Louie, E. Ringe, W. Zhou, S. S. Kim, R. R. Naik, B. G. Sumpter, H. Terrones, F. Xia, Y. Wang, J. Zhu, D. Akinwande, N. Alem, J. A. Schuller, R. E. Schaak, M. Terrones, J. A. Robinson, *ACS Nano* **2015**, *9*, 11509-11539.
- [25] W. Choi, N. Choudhary, G. H. Han, J. Park, D. Akinwande, Y. H. Lee, *Mater. Today* **2017**, *20*, 116-130.
- [26] M. Naguib, M. Kurtoglu, V. Presser, J. Lu, J. Niu, M. Heon, L. Hultman, Y. Gogotsi, M. W. Barsoum, *Adv. Mater.* **2011**, *23*, 4248-4253.
- [27] M. Naguib, O. Mashtalir, J. Carle, V. Presser, J. Lu, L. Hultman, Y. Gogotsi, M. W. Barsoum, *ACS Nano* **2012**, *6*, 1322-1331.
- [28] M. Naguib, V. N. Mochalin, M. W. Barsoum, Y. Gogotsi, *Adv. Mater.* **2014**, *26*, 992-1005.
- [29] Y. Gogotsi, B. Anasori, *ACS Nano* **2019**, *13*, 8491-8494.
- [30] M. Khazaei, A. Mishra, N. S. Venkataramanan, A. K. Singh, S. Yunoki, *Curr. Opin. Solid State Mater. Sci.* **2019**, 164-178.
- [31] B. Anasori, M. R. Lukatskaya, Y. Gogotsi, *Nature Reviews Materials* **2017**, *2*, 16098.
- [32] J. Zheng, B. Wang, A. Ding, B. Weng, J. Chen, *J. Electroanal. Chem.* **2018**, *816*, 189-194.
- [33] N. Sun, Q. Zhu, B. Anasori, P. Zhang, H. Liu, Y. Gogotsi, B. Xu, *Adv. Funct. Mater.* **2019**, *29*, 1906282.
- [34] J. Chen, Q. Huang, H. Huang, L. Mao, M. Liu, X. Zhang, Y. Wei, *Nanoscale* **2020**, *12*, 3574-3592.
- [35] L. Agartan, K. Hantanasirisakul, S. Buczek, B. Akuzum, K. A. Mahmoud, B. Anasori, Y. Gogotsi, E. C. Kumbur, *Desalination* **2020**, *477*, 114267.
- [36] M. W. Barsoum, *Prog. Solid State Chem.* **2000**, *28*, 201-281.
- [37] Z. M. Sun, *Int. Mater. Rev.* **2011**, *56*, 143-166.
- [38] M. Sokol, V. Natu, S. Kota, M. W. Barsoum, *Trends Chem.* **2019**, *1*, 210-223.
- [39] W. Jeitschko, H. Nowotny, F. Benesovsky, *Monatsh. Chem.* **1964**, *95*, 156-157.
- [40] W. Jeitschko, H. Nowotny, F. Benesovsky, *Monatsh. Chem.* **1964**, *95*, 178-179.
- [41] H. Nowotny, W. Jeitschko, F. Benesovsky, *Planseeber. Pulvermetall.* **1964**, *12*, 31-43.
- [42] H. Boller, H. Nowotny, *Monatsh. Chem.* **1966**, *97*, 1053-1058.
- [43] H. Boller, H. Nowotny, *Monatsh. Chem.* **1966**, *97*, 1053-1058.

-
- [44] O. Beckmann, H. Boller, H. Nowotny, *Monatsh. Chem.* **1968**, *99*, 1580-1583.
- [45] M. W. Barsoum, T. El-Raghy, *J. Am. Ceram. Soc.* **1996**, *79*, 1953-1956.
- [46] X. H. Wang, Y. C. Zhou, *J. Mater. Sci. Technol.* **2010**, *26*, 385-416.
- [47] M. W. Barsoum, M. Radovic, *Ann. Rev. Mater. Res.* **2011**, *41*, 195-227.
- [48] M. W. Barsoum, X. Zhao, S. Shanazarov, A. Romanchuk, S. Koumlis, S. J. Pagano, L. Lamberson, G. J. Tucker, *Phys. Rev. Mater.* **2019**, *3*, 013602.
- [49] J. Griggs, A. C. Lang, J. Gruber, G. J. Tucker, M. L. Taheri, M. W. Barsoum, *Acta Mater.* **2017**, *131*, 141-155.
- [50] J. Gruber, A. C. Lang, J. Griggs, M. L. Taheri, G. J. Tucker, M. W. Barsoum, *Sci. Rep. - UK* **2016**, *6*, 33451.
- [51] M. W. Barsoum, T. El-Raghy, *American Scientist* **2001**, *89*, 334-343.
- [52] D. Chen, K. Shirato, M. W. Barsoum, T. El-Raghy, R. O. Ritchie, *J. Am. Ceram. Soc.* **2001**, *84*, 2914-2920.
- [53] X. H. Wang, Y. C. Zhou, *Oxid. Met.* **2003**, *59*, 303-320.
- [54] M. Sundberg, G. Malmqvist, A. Magnusson, T. El-Raghy, *Ceram. Int.* **2004**, *30*, 1899-1904.
- [55] S. Basu, N. Obando, A. Gowdy, I. Karaman, M. Radovic, *J. Electrochem. Soc.* **2011**, *159*, C90-C96.
- [56] M. Haftani, M. Saeedi Heydari, H. R. Baharvandi, N. Ehsani, *Int. J. Refract. Met. Hard Mater.* **2016**, *61*, 51-60.
- [57] P. Eklund, J. Rosen, P. O. A. Persson, *J. Phys. D: Appl. Phys.* **2017**, *50*, 113001.
- [58] P. Eklund, M. Beckers, U. Jansson, H. Högberg, L. Hultman, *Thin Solid Films* **2010**, *518*, 1851-1878.
- [59] M. Radovic, M. W. Barsoum, *Am. Ceram. Soc. Bull.* **2013**, *92*, 20-27.
- [60] W. Jeitschko, *Acta Crystallographica Section B* **1969**, *25*, 163-165.
- [61] W. Jeitschko, *Monatshefte für Chemie und verwandte Teile anderer Wissenschaften* **1966**, *97*, 1472-1476.
- [62] N. F. Chaban, Y. B. Kuz'ma, *Izvestiya Akademii Nauk SSSR, Neorganicheskie Materialy* **1973**, *9*, 1908-1911.
- [63] M. Ade, H. Hillebrecht, *Inorg. Chem.* **2015**, *54*, 6122-6135.
- [64] H. Zhang, F.-z. Dai, H. Xiang, Z. Zhang, Y. Zhou, *J. Mater. Sci. Technol.* **2019**, *35*, 530-534.
- [65] K. Petry, W. Jung, *Z. Kristallogr* **1988**, *182*, 153.
- [66] S. Kota, M. Sokol, M. W. Barsoum, *Int. Mater. Rev.* **2019**, 1-30.

- [67] A. Gencer, I. Yilmaz, U. Bayhan, G. Surucu, *Avrupa Bilim ve Teknoloji Dergisi* **2019**, 351-359.
- [68] G. Surucu, A. Gencer, X. Wang, O. Surucu, *J. Alloys Compd.* **2020**, 819, 153256.
- [69] K. Mohammad, A. Masao, S. Taizo, E. Mehdi, S. Yoshio, *J. Phys.: Condens. Matter* **2014**, 26, 505503.
- [70] P. Chakraborty, A. Chakrabarty, A. Dutta, T. Saha-Dasgupta, *Phys. Rev. Mater.* **2018**, 2, 103605.
- [71] A. Gencer, G. Surucu, *Mater. Res. Express* **2018**, 5, 076303.
- [72] G. Surucu, *Mater. Chem. Phys.* **2018**, 203, 106-117.
- [73] A. Mockute, P. O. Å. Persson, F. Magnus, A. S. Ingason, S. Olafsson, L. Hultman, J. Rosen, *phys, status solidi – R* **2014**, 8, 420-423.
- [74] C. M. Hamm, J. D. Bocarsly, G. Seward, U. I. Kramm, C. S. Birkel, *J. Mater. Chem. C* **2017**, 5, 5700-5708.
- [75] C. M. Hamm, M. Durrschnabel, L. Molina-Luna, R. Salikhov, D. Spoddig, M. Farle, U. Wiedwald, C. S. Birkel, *Mater. Chem. Front.* **2018**, 2, 483-490.
- [76] C.-C. Lai, Q. Tao, H. Fashandi, U. Wiedwald, R. Salikhov, M. Farle, A. Petruhins, J. Lu, L. Hultman, P. Eklund, J. Rosen, *APL Mater.* **2018**, 6, 026104.
- [77] G. W. Bentzel, M. Sokol, J. Griggs, A. C. Lang, M. W. Barsoum, *J. Alloys Compd.* **2019**, 771, 1103-1110.
- [78] M. Nechiche, T. Cabioc'h, E. N. Caspi, O. Rivin, A. Hoser, V. Gauthier-Brunet, P. Chartier, S. Dubois, *Inorg. Chem.* **2017**, 56, 14388-14395.
- [79] D. Horlait, S. C. Middleburgh, A. Chroncos, W. E. Lee, *Sci. Rep. - UK* **2016**, 6, 18829.
- [80] Q. Tao, M. Dahlqvist, J. Lu, S. Kota, R. Meshkian, J. Halim, J. Palisaitis, L. Hultman, M. W. Barsoum, P. O. Å. Persson, J. Rosen, *Nat. Commun.* **2017**, 8, 14949.
- [81] Z. Liu, E. Wu, J. Wang, Y. Qian, H. Xiang, X. Li, Q. Jin, G. Sun, X. Chen, J. Wang, M. Li, *Acta Mater.* **2014**, 73, 186-193.
- [82] L. Zheng, J. Wang, X. Lu, F. Li, J. Wang, Y. Zhou, *J. Am. Ceram. Soc.* **2010**, 93, 3068-3071.
- [83] Y. Zhou, F. Meng, J. Zhang, *J. Am. Ceram. Soc.* **2008**, 91, 1357-1360.
- [84] Z. Lin, M. Zhuo, Y. Zhou, M. Li, J. Wang, *J. Am. Ceram. Soc.* **2006**, 89, 3765-3769.

2 MAX phase borides

2.1 Syntheses and physical properties of the MAX phase boride Nb₂SB and the solid solutions Nb₂SB_xC_{1-x} ($x = 0 - 1$)

Tobias Rackl, Lucien Eisenburger, Robin Niklaus, and Dirk Johrendt

Published in: *Physical Review Materials* **2019**, 3, 054001.

Reproduced from Reference with permission from the American Physical Society.

Abstract

The MAX phase boride Nb₂SB and the solid solutions Nb₂SB_xC_{1-x} ($x = 0 - 1$) were synthesized via solid-state methods and characterized by X-ray powder diffraction. All phases crystallize in the hexagonal Cr₂AlC type with the space group $P6_3/mmc$. The lattice parameters increase with the boron content [$a = 3.278(1) - 3.334(1)$ Å (+1.7 %), $c = 11.49(1) - 11.54(1)$ Å (+0.5 %)] and the distortions of the Nb₆(B,C) octahedra slightly decrease. Magnetic susceptibility and dc resistivity measurements confirm that Nb₂SC is a superconductor, while Nb₂SB shows no superconducting transition above 1.9 K. The solid solutions Nb₂SB_xC_{1-x} are metals and superconductors for $x = 0 - 0.6$ with critical temperatures of $T_c = 4.8 - 2.6$ K, which decrease with increasing boron content. First-principles density-functional theory calculations confirm the metallic state and a lower electronic density of states at the Fermi energy in the boride. The calculated elastic constants, phonon density of states, and Debye temperatures of Nb₂SB are similar to Nb₂SC and are probably not the reason for the absence of superconductivity in the boride. We therefore suggest that the lower $N(\varepsilon_F)$ of the boride reduces the interaction strength and thus the superconducting critical temperature.

Introduction

The MAX phases are a large family of layered ternary compounds with the chemical formula $M_{1+n}AX_n$ ($n = 1 - 3$), where M is an early transition metal, A is a main group element, and X is either carbon or nitrogen. Their hexagonal crystal structures consist of $M_{1+n}X_n$ layers interleaved

with A -group element layers. Strong $M - X$ bonds and weaker $M - A$ bonds result in a nano-laminated structure. First synthesized by Nowotny *et al.* in the 1960s, they still attract great interest due to their unified metallic and ceramic properties.^[1] This outstanding combination makes them promising candidates for a wide range of uses like sensors, electric contacts, and especially high-temperature applications.^[2-5]

More than 60 ternary MAX phases and many solid solutions exist. Notably, the substitution of the M and A sites yielded various compounds, for example $(\text{Nb}, \text{Zr})_2\text{AlC}$, $(\text{Ti}, \text{V})_2\text{SC}$, $(\text{Ti}, \text{Hf})_2\text{SC}$, $\text{V}_2(\text{Al}, \text{Ga})\text{C}$, $\text{Ti}_2(\text{Si}, \text{Ge})\text{C}$, and $\text{Cr}_2(\text{Al}, \text{Ge})\text{C}$.^[3, 6-12] In contrast, X -site solid solutions are mostly limited to carbonitrides $M_{n+1}A(\text{C}, \text{N})_n$ up to now. One example is $\text{Ti}_2\text{AlC}_{0.5}\text{N}_{0.5}$, with enhanced hardness and stiffness compared to Ti_2AlC and the nitride Ti_2AlN .^[13-14] Oxygen can also incorporate into MAX phases, by either the reaction with gaseous O_2 or with Al_2O_3 .^[15-16] However, the oxygen saturation content in $M_{n+1}A(\text{C}, \text{O})_n$ is not known.^[2]

Even though the importance of the X atom on the properties of MAX phases is accepted, potential elements are currently restricted to carbon, nitrogen, and possibly oxygen. Recently, MAX borides have been theoretically predicted.^[17-18] Among them, some $M_2\text{AlB}$ ($M = \text{Sc}, \text{Ti}, \text{Cr}, \text{Zr}, \text{Nb}, \text{Mo}, \text{Hf},$ and Ta) phases should be metastable. Theoretical analysis of the mechanical properties showed that the predicted Ta_2AlB , Cr_2AlB , and Mo_2AlB exhibit high shear and Young's moduli, while Zr_2AlB is a great candidate for structural applications. Furthermore, ab initio calculations showed that among the M_2AB ($M = \text{Ti}, \text{Zr}, \text{Hf}; A = \text{Al}, \text{Ga}, \text{In}$) phases, Hf_2InB is the most stable, although all compounds have negative formation enthalpies and should, therefore, be synthesizable.^[19] A recent study compares V_2AlC with hypothetical V_2AlB and predicts that boron-based MAX phases are more ductile due to weaker $V - B$ bonds.^[20]

A family of compounds closely related to the MAX phases is called the MAB phases, wherein M is a transition metal, A is Al or Si, and B is boron. Although MAB and MAX phases show different structural motifs, they share the two-dimensionality and the combination of covalent and metallic interactions. MAB phases form layered structures in different orthorhombic space groups. Layers of face-sharing BM_6 trigonal prisms alternate with Al or Si.^[21-31] The BM_6 prism is the common coordination polyhedra for binary transition-metal borides, for example, in Cr_2B_3 , NbB_2 , Nb_3B_4 , ZrB_2 , and many more.^[32-35]

In this paper, we report the syntheses of the MAX phase boride Nb_2SB and its solid solutions with the carbide $\text{Nb}_2\text{SB}_x\text{C}_{1-x}$ ($x = 0 - 1$). These are the first MAX phase borides. The change of the crystal structure was studied by Rietveld refinement of X-ray powder diffraction patterns. The substitution of carbon by boron can be tracked by the change of lattice parameters as well as by the distortion of the $\text{Nb}_6(\text{B}, \text{C})$ octahedra. We show that the compounds $\text{Nb}_2\text{SB}_x\text{C}_{1-x}$ ($x = 0 - 1$) are metallic conductors and exhibit superconductivity for $x = 0 - 0.6$.

Experimental

Polycrystalline samples of $\text{Nb}_2\text{SB}_x\text{C}_{1-x}$ ($x = 0 - 1$) were synthesized by solid-state reaction of the elements niobium (99.99 %, ~325 mesh, Alfa Aesar), sulfur (≥ 99 %, flakes, Sigma Aldrich), boron (99 %, powder, Koch-Light- Laboratories), and graphite (100 %, powder, ACROS Organics). For microwave reaction, a homogenized mixture of niobium and sulfur with the ratio 2:1 was filled in an alumina crucible and sealed in an argon-filled silica tube. The ampoule was placed in an alumina crucible, which was filled with 25 g granular graphite. An insulating housing surrounded the setup. The reaction took place at 600 W for 20 min. After cooling down to room temperature, the obtained black powder was homogenized and used for the following reactions. A mixture of the pre-reacted niobium-sulfur, boron, and carbon was homogenized and pressed to a pellet with a diameter of 5 mm (2 t, 120 s). The pellet was welded in an argon-filled niobium crucible and then sealed in an argon-filled silica tube. The reaction mixture was heated to 1200 °C within 6 h, and a 65 h dwell time. The crucibles were allowed to cool down to room temperature by shutting off the oven. The procedure was repeated 2 – 5 times to increase the homogeneity of the samples. The products were black powders with purities of 92 – 99 wt.%.

Powder X-ray diffraction was carried out using a Huber G670 diffractometer with $\text{Cu-K}\alpha_1$ radiation ($\lambda = 1.54059\text{\AA}$) and Ge-111 monochromator. Structural parameters were determined by Rietveld refinement using the TOPAS software package.^[36] Magnetic and resistivity measurements were performed with a Quantum Design PPMS-9. The magnetization was determined using the vibrating sample magnetometer option. Zero-field-cooled and field-cooled measurements were carried out between 1.9 and 20 K with an applied field of 15 Oe. The isothermal magnetization was determined at 1.9 K with variable fields of $H = \pm 50$ kOe. For resistivity measurements, the samples were pressed to pellets with a diameter of 5 mm and a thickness of ~ 1 mm. The pellets were sintered at 1000 °C for 48 h and contacted using the Wimbush press contact assembly for van der Pauw measurements.^[37]

For scanning transmission electron microscopy (STEM), a small volume of the sample was ground in absolute ethanol. The resulting suspension was applied to a copper grid covered with a holey carbon film (Plano GmbH, Germany). The grid was mounted on a double-tilt holder and transferred into a C_s dodecapole corrector probe-corrected Titan Themis 300 (FEI, USA) TEM equipped with an extreme field emission gun, a post-column filter (Enfinium ER-799), an US1000XP/FT camera system (Gatan, Germany), and a windowless four-quadrant Super-X energy dispersive X-ray spectroscopy detector. TEM images were recorded using a $4\text{k} \times 4\text{k}$ FEI Ceta complementary metal-oxide-semiconductor camera. The microscope was operated at 300 kV accelerating voltage for SAED and STEM-HAADF (convergence angle of 16.6 mrad, 50 μm

aperture, detector inner half angle 63 mrad for 100 mm camera length). For evaluation of the TEM data Digital Micrograph (Fourier filtering of STEM images) was used.

Electronic structure calculations were performed using the Vienna Ab initio Simulation Package (VASP), which is based on density-functional theory (DFT) and plane-wave basis sets.^[38-39] Projector-augmented waves (PAW) were used, and contributions of correlation and exchange were treated in the generalized gradient approximation.^[40-41] The PAW eigenstates were afterward projected onto localized crystal orbitals using LOBSTER.^[42] Elastic tensors were determined by performing finite distortions and deriving the elastic constants from the strain-stress relationship. The bulk moduli were calculated using the Voigt approximation $B = (1/9)[(C_{11}+C_{12})+4C_{13}+C_{33}]$ or from energy vs volume calculations, which yielded the same results. Debye temperatures Θ_D were estimated from the bulk modules and Poisson's ratios using a quasi-harmonic model.^[43] For phonon calculations of $2 \times 2 \times 2$ supercells were calculated with a k-mesh sampling of $8 \times 8 \times 3$. Force sets and lattice vibrations were subsequently calculated using the PHONOPY program.^[44-45] Further details are provided in the appendix chapter A.1.3.

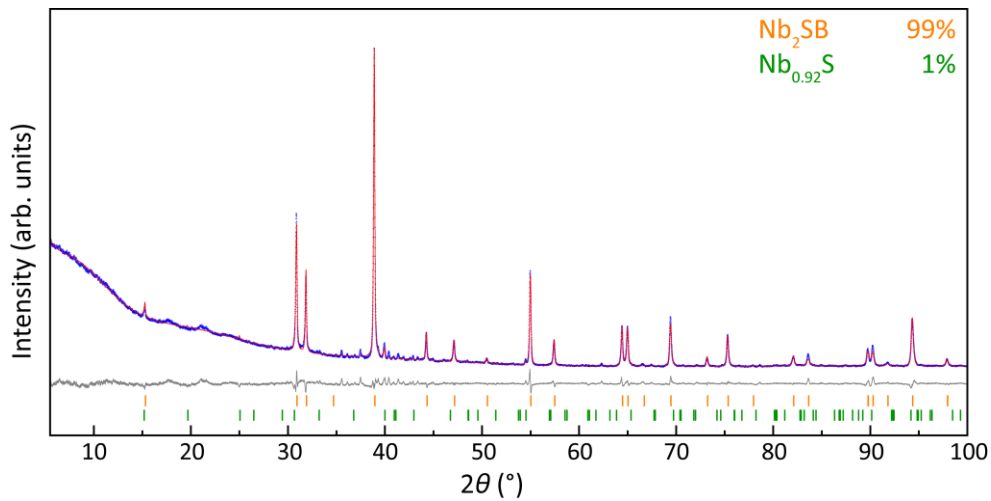


Figure 2-1: X-ray powder pattern of Nb₂SB (blue) with Rietveld fit (red) and difference curve (gray).

Results and discussion

Synthesis and crystal structure

Nb₂SB and its solid solutions with carbon Nb₂SB_xC_{1-x} ($x = 0 - 1$) can be synthesized at 1200 °C via solid-state reaction. It turned out that the use of a pre-reacted mixture of niobium and sulfur in the ratio of 2:1 leads faster to the product than the direct use of the elements. The pre-reaction

took place in a microwave oven, as a fast and efficient way to prepare precursors. Besides the pre-reaction, a rapid cooling rate also prefers the formation of Nb_2SX ($X = \text{B}, \text{C}$) phases. Samples with broad reflections in the PXRD pattern or a significant amount of impurity phases were homogenized and heated again under the same conditions. The $\text{Nb}_2\text{SB}_x\text{C}_{1-x}$ ($x = 0 - 1$) phases prepared by this procedure are black powders. The proportions of the products are > 92 wt.% with the impurity phases NbC and NbB. Minor unidentified impurities occur for $x \geq 0.80$.

Figure 2-1 shows the Rietveld refinement of the powder diffraction pattern of Nb_2SB starting from the Nb_2SC structure. Nb_2SB crystallizes in the hexagonal space group $P6_3/mmc$ (see Table 2-1) just as the solid solutions $\text{Nb}_2\text{SB}_x\text{C}_{1-x}$ ($x = 0 - 1$). Layers of edge-sharing $\text{Nb}_6(\text{C},\text{B})$ octahedra alternate with sulfur layers (Figure 2-4). The unit-cell A-site substitution effects in MAX phases dimensions of Nb_2SB are slightly enlarged with $a = 3.335(1) \text{ \AA}$, $c = 11.55(1) \text{ \AA}$, and $V = 111.2(1) \text{ \AA}^3$ compared to Nb_2SC ($a = 3.278(1) \text{ \AA}$, $c = 11.49(1) \text{ \AA}$, and $V = 107.0(1) \text{ \AA}^3$).

Table 2-1: Crystallographic data of Nb_2SB .

Chemical formula	Nb_2SB				
M ($\text{g}\cdot\text{mol}^{-1}$)	228.69				
Crystal system, Space group	hexagonal, $P6_3/mmc$ (194)				
T (K)	293				
a (Å), c (Å)	3.335(1), 11.55(1)				
V (Å^3)	111.2(1)				
Z	2				
Radiation type	Cu- $\text{K}\alpha_1$, $\lambda = 1.54056 \text{ \AA}$				
Diffractometer	Huber G670				
Monochromator	Ge-111				
R_p	2.290				
R_{wp}	3.447				
Goodness of fit	3.709				
Atom positions and equivalent isotropic displacement parameters (Å^2)					
Atom	x	y	z	U_{eq}	occ
Nb	1/3	2/3	0.60172(6)	0.5	1
S	1/3	2/3	1/4	1	1
B	0	0	0	3	1
Selected interatomic distances (Å)					
B — 6×Nb 2.2557(4) S — 6×Nb 2.5772(5) Nb — 3×Nb 3.0383(8)					

Figure 2-2 shows a STEM-HAADF image of Nb₂SB perpendicular to [100]. The brightest intensity can be assigned to niobium atoms, and the crystal structure is superimposed to the image. The “zigzag” stacking of the layers of M₆B octahedra is characteristic for MAX phases.^[2]

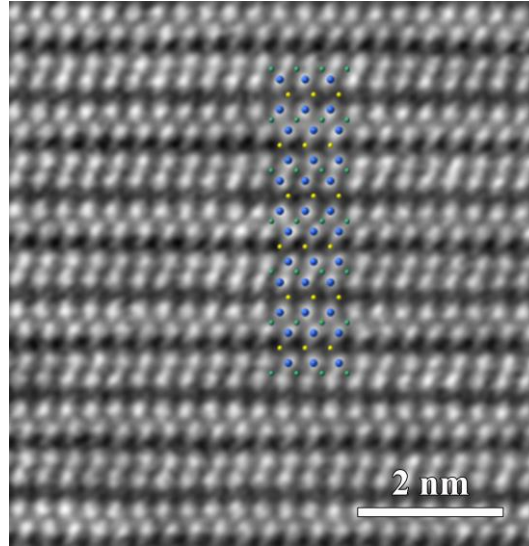


Figure 2-2: STEM-HAADF image of Nb₂SB perpendicular to [100]. The inset of the structure of Nb₂SB indicates the position of Nb- (blue), S- (yellow), and B (green) atoms.

Nb₂SC_x ($x = 0.66 - 1$) is different from most ternary MAX phases, because it shows significant vacancies at the C site, which shortens the *a*-axis with decreasing *x*.^[46] It might be that the vacancies in his system open the opportunity to substitute carbon by boron.

Since it is not possible to determine a C/B mixed occupancy at the *X* site with the Rietveld method, different parameters are necessary to track the degree of substitution in Nb₂SB_xC_{1-x}. One option is the change of the unit-cell dimensions. In solid solutions Nb₂SB_xC_{1-x} ($x = 0 - 1$) the *a*-axis increases by 1.7 % with the boron content from 3.278(1) to 3.335(1) Å. In comparison, the elongation of the *c*-axis from 11.49(1) to 11.55(1) Å ($\cong 0.5$ %) is less pronounced. The change of the *a*- and *c*-axis results in an increase of the cell volume by 3.9 % from 107.0(1) Å³ to 111.2(1) Å³ (see Figure 2-3).

$$\alpha_r = \frac{d_1}{d_2} = \frac{\sqrt{3}}{2\sqrt{4z_M^2 \left(\frac{c}{a}\right)^2 + \frac{1}{12}}} \quad \text{Equation 2-1}$$

Another quantity to describe the change of the crystal structure is the distortion of the M₆X octahedron. Barsoum and co-workers described the degree of distortion (α_t) by the ratio of the

distance of two opposite faces, not in the basal plane (d_1) and the distances of two opposite faces in the basal plane (d_2) (see Figure 2-4).^[47] By rearranging the formula, the ratio depends on the coordinate z_M of the M atom and the c/a ratio (see equation 2-1).

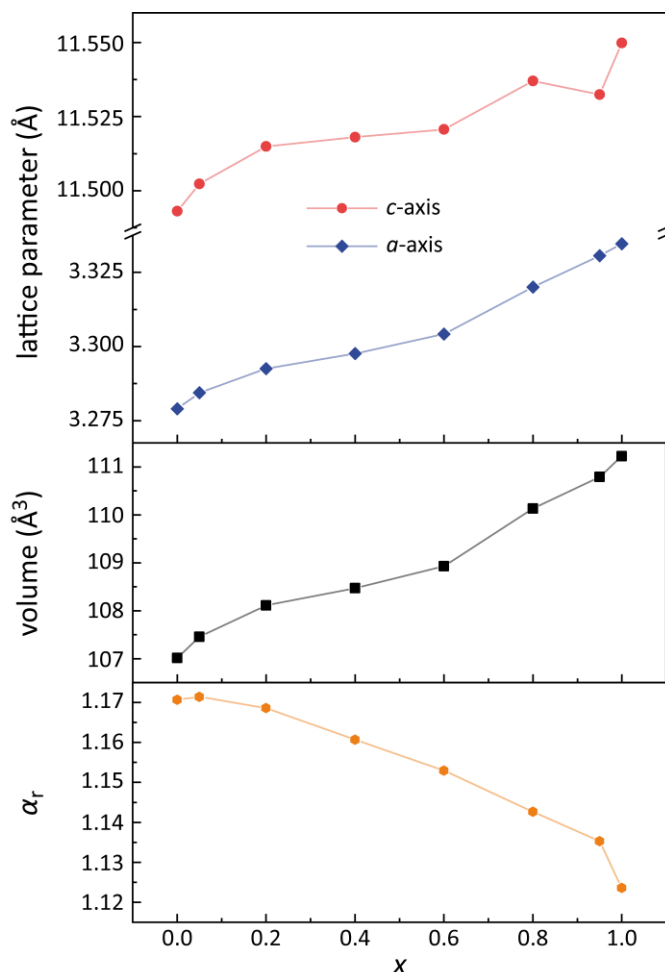


Figure 2-3: Lattice parameters (top), unit-cell volume (middle), and octahedron aspect ratio (bottom) of $\text{Nb}_2\text{SB}_x\text{C}_{1-x}$ ($x = 0 - 1$) as a function of the boron content x .

Figure 2-3 displays the values α_r for the solid solutions $\text{Nb}_2\text{SB}_x\text{C}_{1-x}$ ($x = 0 - 1$). The octahedra become less distorted with increasing boron content, resulting in values of α_r from 1.171 to 1.123, which is a reduction of the distortion by 4.1 %. The d_1/d_2 ratios are greater than 1, which means that the faces in the basal plane are closer together than the faces not in the basal plane. Since z_M increases by 5.8 % while the c/a ratio decreases by 1.2 %, the relaxation of the octahedron is a result of the z_M parameter of the Nb site and not the lattice parameters. The substitution of carbon by boron reduces the Nb — Nb distance by 2.3 % and thus the layer distances. The combination of both the octahedron relaxation and the layer compression leads to an almost unchanged c -axis.

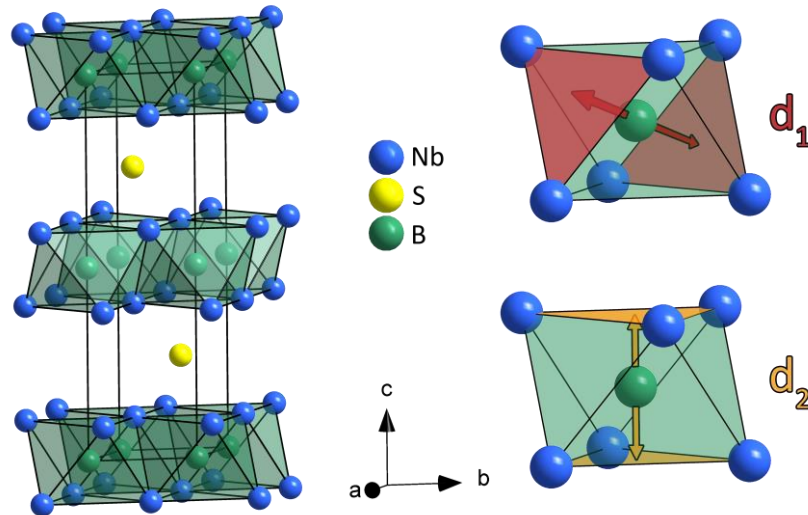


Figure 2-4: Crystal structure of Nb₂SB (left). The plane distances d_1 (faces not parallel to the basal plane) and d_2 (faces parallel to the basal plane) used for the calculation of the octahedral distortion are displayed on the right.

Magnetic properties

The susceptibility of Nb₂SB_xC_{1-x} ($x = 0 - 1$) was measured in an external field of $H = 15$ Oe between 1.9 and 20 K. Isothermal magnetization plots at $T = 1.9$ K at variable fields of $H = \pm 50$ kOe are given in the appendix (Figure A-9 – A-12). Figure 2-5 shows the susceptibility of Nb₂SB_xC_{1-x} ($x = 0 - 1$). Bulk superconductivity occurs in Nb₂SC at the critical temperature $T_c = 4.0$ K, which is slightly lower than given in the literature.^[46] T_c decreases from 4.0 to 2.6 K, with increasing boron content from $x = 0 - 0.40$. For compounds with a higher boron content ($x \geq 0.60$), no bulk superconductivity is observed. For $x = 0.80, 0.95,$ and 1.0 , the susceptibility drops slightly between 4 and 5 K, which indicates small amounts of unidentified superconducting impurities.

Resistivity

Figure 2-6 shows the temperature-dependent resistivity of the solid solutions Nb₂SB_xC_{1-x} ($x = 0 - 1$). The values at room temperature are in the range of $1.3 - 4.5 \times 10^{-6} \Omega\text{m}$ with Nb₂SB showing the lowest resistivity, which is slightly higher than typical values of other MAX phases around $0.2 - 0.7 \times 10^{-6} \Omega\text{m}$.^[2, 48] We also see no trend with the boron content x . However, resistivities of compacted polycrystalline samples strongly depend on hardly controllable grain-boundary effects, which make absolute values often unreliable. Between 50 and 300 K, the resistivity decreases linearly with decreasing temperature, which is typical for metallic conductors.

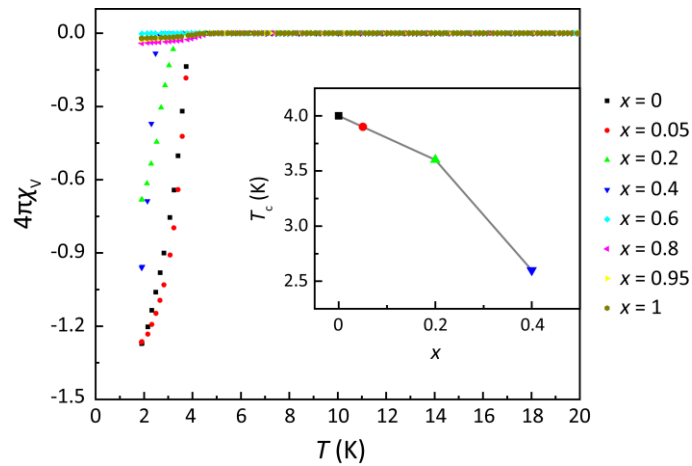


Figure 2-5: Low-field (15 Oe) magnetic susceptibilities of $\text{Nb}_2\text{SB}_x\text{C}_{1-x}$ ($x = 0 - 1$) in the temperature range of 1.9 and 20 K. Inset: Critical temperature T_c as a function of the boron content in the solid solutions $\text{Nb}_2\text{SB}_x\text{C}_{1-x}$ ($x = 0 - 1$).

The drop of resistance at low temperatures confirms the superconductivity of $\text{Nb}_2\text{SB}_x\text{C}_{1-x}$ ($x = 0 - 0.40$), which was also found in the magnetic measurements. The inset in Figure 2-6 shows the dependence of T_c on x . As for the susceptibility data (Figure 2-5), the critical temperature decreases with increasing boron content. However, all values are slightly higher than those from the susceptibility data. $\text{Nb}_2\text{SB}_{0.6}\text{C}_{0.4}$ still exhibits superconductivity at $T_c = 2.6$ K. For $x = 0.80$ and 1.0 , a drop occurs, but zero resistivity is not reached. This drop is a sign of superconducting impurity phases, which confirms the findings of the magnetic measurements.

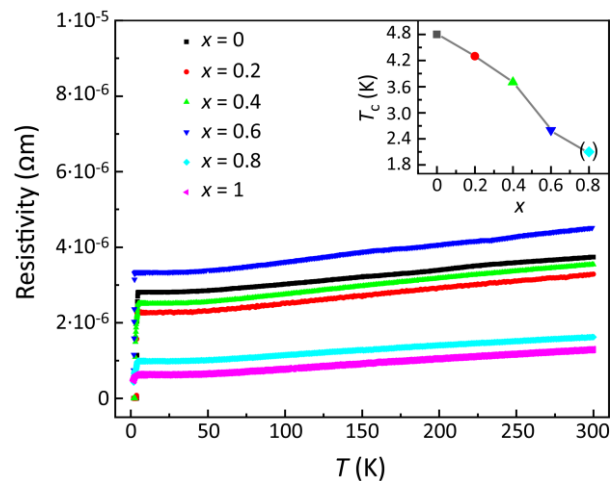


Figure 2-6: Resistivities determined by van der Pauw measurements in the temperature range of 1.9 and 300 K. Inset: Critical temperature T_c as a function of the boron content in the solid solutions $\text{Nb}_2\text{SB}_x\text{C}_{1-x}$ ($x = 0 - 1$).

Superconductivity in MAX phases is a rare phenomenon, and there are conflicting reports on whether some of them, for example, Nb_2SnC , are superconductors or not.^[49] Measurements of superconductivity are sensitive to impurity phases, which was shown in detail by Anasori *et al.*^[50] Studies in systems containing niobium are especially problematic since the metal and some of its compounds, for example, NbC , exhibit superconductivity. Our measurements clearly show Nb_2SC is a superconductor as described in the literature, while Nb_2SB it not superconducting above 1.9 K.

Electronic and elastic properties

First-principles DFT band-structure calculations confirm the metallic state of Nb_2SB . Figure 2-7 top shows the total and atom-resolved density of states. The Nb 4*d* states dominate the density of state (DOS) at Fermi energy, while contributions from sulfur and boron are small. Niobium states spread over more than 15 eV, which indicates strong covalent interactions with the boron and sulfur neighbors. Integration of the atom-resolved DOS gives the charges $(\text{Nb}^{+0.9})_2\text{S}^{-0.6}\text{B}^{-1.2}$, which covers the complete electron density thanks to the projection of the PAW eigenstates onto localized orbitals.^[42]

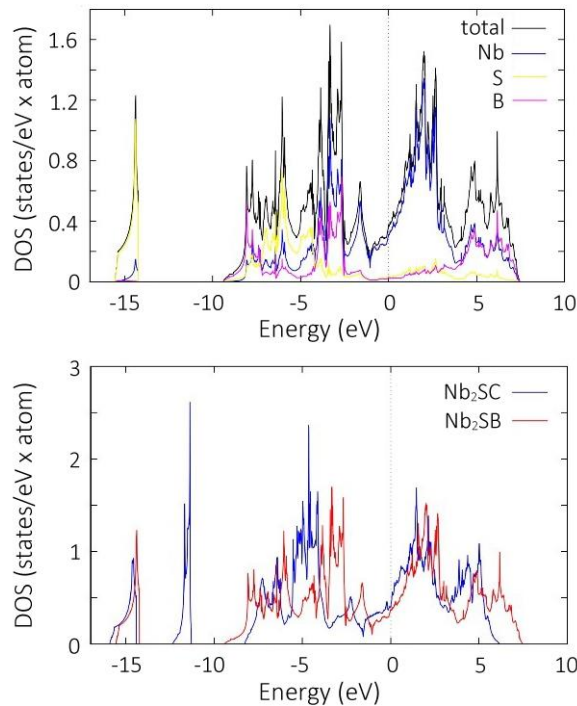


Figure 2-7: top: Total and atom-resolved density of states of Nb_2SC . bottom Total DOS of Nb_2SB in comparison with Nb_2SC , showing the lower DOS at the Fermi level in the boride. The energy zeros are taken at the Fermi level.

Figure 2-7 bottom compares the total DOS of Nb₂SB and Nb₂SC. The band filling is larger in the carbide due to two additional electrons in the unit cell. Since the Fermi level is at a rising edge of the Nb dominated area, an increasing band filling also increases the density of states at the Fermi level $N(\varepsilon_F)$. By assuming that Nb₂SC is a conventional superconductor, the decreasing $N(\varepsilon_F)$ with boron substitution may be responsible for the lower critical temperatures of Nb₂SB_xC_{1-x} and, finally, the absence of superconductivity in Nb₂SB. However, T_c of conventional superconductors also depends on the electron-phonon coupling strengths and the Debye temperature. These properties are linked to the elastic constants, which are available for Nb₂SC in the literature.^[51-52] We have calculated the elastic constants, bulk moduli, linear compressibility ratios $f = k_c/k_a$, and the Debye temperatures for Nb₂SC and Nb₂SB. A comparison of the results is given in Table 2-2.

Table 2-2: Elastic constants C_{ij} (GPa), bulk moduli B (GPa), compressibility ratios f , and Debye temperatures Θ_D (K) of Nb₂SC and Nb₂SB.

	C_{11}	C_{12}	C_{13}	C_{33}	C_{44}	B	f	Θ_D	Ref.
Nb ₂ SC	304	117	155	316	88	221	0.69	-	[51]
	320	101	153	327	126	197	0.66	530	[52]
	301	105	157	314	116	194	0.59	521	This thesis
Nb ₂ SB	316	95	131	317	143	186	0.80	573	This thesis

The values for Nb₂SC from the literature and our calculation agree within 5 – 10 %, which is probably due to the usage of different program packages, parameters, or potentials. Our results for Nb₂SC and Nb₂SB are comparable because they were calculated with the identical procedure. The elastic constants of the boride and carbide are similar, only the C_{44} values differ by 20 %. The boride has a slightly smaller bulk module but a higher Debye temperature compared to the carbide. From this, one would expect a slightly higher superconducting T_c in the boride, which contradicts the experimental finding. The compressibility ratio f shows that the a -axis is softer in both compounds. This anisotropy is weaker in the boride, where the f parameter is closer to 1.

Figure 2-8 shows the phonon density of states of Nb₂SB and Nb₂SC. The peaks at high frequencies between 500 and 700 cm⁻¹ are caused by boron and carbon; sulfur modes are around 300 cm⁻¹, and the broad feature around 100–250 cm⁻¹ are niobium modes (for plots of the atom-projected phonon DOS see Figure A-13).

All modes of the boride slightly shift to higher energies, which agrees with the higher calculated Debye temperature. This should increase T_c of the boride, which contradicts the experiments. A

further analysis requires calculations of the electron-phonon coupling constants λ . Reference classifies Nb₂SC as moderately coupled superconductor and estimates $\lambda = 0.49$ from the calculated

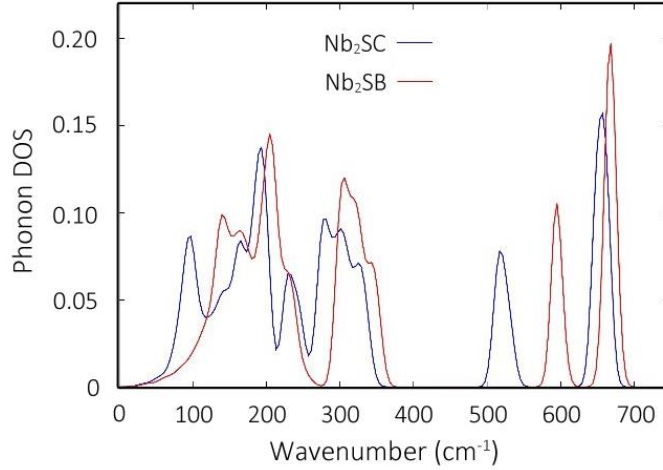


Figure 2-8: Phonon density of states of Nb₂SC (blue) and Nb₂SB (red).

$\Theta_D = 540$ K and the experimental $T_c = 4.8$ K using McMillan's formula.^[52-53] Given that a T_c of Nb₂SB is below 1.9 K, the same formula with $\Theta_D = 570$ K gives $\lambda \leq 0.4$ as the upper limit for the boride. However, current methods to calculate λ still comprise approximations, which make it very difficult to reliably discriminating a T_c difference of 3 K, especially in compounds with anisotropic crystal structures.^[54] In the present case, the Debye temperatures differ by only 10 %, which is within the uncertainty of the calculation, and would anyway change T_c by less than 0.5 K. On the other hand, $N(\epsilon_F)$ is unambiguously smaller in the boride because it is an inevitable consequence of the lower band filling [Figure 2-7 (b)]. Given that λ roughly corresponds to the interaction strength $N(\epsilon_F)V$ (V is the pairing potential), we suggest that the lower T_c of the boride is finally a consequence of the lower density of states at the Fermi level.^[53]

Conclusion

Nb₂SB and the solid solutions Nb₂SB_{*x*}C_{1-*x*} ($x = 0 - 1$) were successfully synthesized via solid-state methods. These are the first MAX phase borides. They crystallize in a layered hexagonal structure (Cr₂AlC type), which is characteristic for these phases. The carbon substitution by boron leads to increasing cell dimensions and less distorted Nb₆(B,C) octahedra. Nb₂SB is not a superconductor, while Nb₂SC is superconducting below 5 K, as described in the literature.^[47, 55] The solid solutions Nb₂SB_{*x*}C_{1-*x*} are metallic conductors and exhibit superconductivity for $x = 0 - 0.60$, while T_c decreases with the boron content from 4.8 to 2.6 K. DFT calculations indicate the lowering of the density of states with increasing boron content, which we believe is

the main reason for the decreasing critical temperatures. The elastic constants and Debye temperatures of the boride are similar and cannot account for the absence of superconductivity in the boride. We therefore suggest that the lower $N(\varepsilon_F)$ of the boride reduces the interaction strength and thus the superconducting critical temperature. Since $\text{Nb}_2\text{SB}_x\text{C}_{1-x}$ ($x = 0 - 1$) are among the first boron-containing MAX phases, the effects of boron on other properties like stiffness, thermal conductivity, shock resistance, damage tolerance, and electron-phonon coupling will be tasks for further investigations.

2.2 The MAX phase borides Zr₂SB and Hf₂SB

Tobias Rackl and Dirk Johrendt

Solid State Sciences, 2020, 106316

Abstract

Zr₂SB and Hf₂SB were synthesized via solid-state reactions, and the crystal structures were determined by Powder X-ray diffraction. Both compounds crystallize in the hexagonal Cr₂AlC-type structure ($P6_3/mmc$; $Z = 2$; Zr₂SB $a = 3.5001(1)$ Å, $c = 12.2712(2)$ Å; Hf₂SB $a = 3.4671(1)$ Å, $c = 12.1046(2)$ Å). The lattice parameters and bond lengths are slightly longer, and the M_6X octahedra are less distorted compared to the known carbides. Resistivity and magnetic measurements reveal that Zr₂SB and Hf₂SB are good metallic conductors and Pauli paramagnets. Ab-initio DFT calculations of the electronic structure confirm the metallic state and show mainly ionic bonds, which are weaker than in the carbides. The elastic constants indicate that Zr₂SB and Hf₂SB are brittle and exhibit a less two-dimensional character compared to other MAX phases.

Introduction

The MAX phases are a group of transition metal carbides and nitrides, which share unified properties of ceramics and metals. They exhibit good thermal and electronic conductivity, high damage, and thermal shock tolerance, are easy to machine and rather soft.^[56-58] Furthermore, they deform by ripplation nucleation under external pressure, and show a brittle to plastic transition at high temperatures.^[59-62] The elemental composition at the M and A site is highly variable, resulting in more than 150 different compounds composed of 32 different elements. However, this variety is confined to the M - and A -components, while the X -elements of the MAX phases are either carbon or nitrogen so far. Another potential X -element is boron, as predicted from DFT calculations.^[17-19, 62] Related compounds are the so-called MAB phases, not to be confused with MAX phase borides. MAB phases likewise exhibit laminated structures, but the M atom coordination is prismatic instead of octahedral, and in particular, MAB compounds contain B — B bonds.^[63] Therefore, a clear distinction has to be made between MAB phases and MAX phase borides.

We recently reported on the MAX phase boride Nb₂SB and the solid solutions Nb₂S(B_xC_{1-x}) as the first examples for the incorporation of boron in the Cr₂AlC-type structure.^[64] Replacing carbon by boron in Nb₂SC increases the lattice parameters only slightly, but the physical properties change significantly. Especially, the superconductivity of Nb₂SC vanishes upon boron substitution for $x > 0.6$ in Nb₂S(B_xC_{1-x}).^[64] Here we report on the synthesis, crystal structure, chemical bonding, and physical properties of Zr₂SB and Hf₂SB, which extend the MAX phase borides beyond Nb₂SB.

Experimental Section

Zr₂SB and Hf₂SB were synthesized via solid-state reactions starting from stoichiometric mixtures of the elements (Zr 99.8 %, rod, abcr; Hf 99.8 %, powder, Alfa Aesar; S \geq 99 %, flakes, Sigma Aldrich; B 99 %, powder, Koch-Light-Laboratories). All preparation steps took place in an argon-filled glovebox. The starting materials were homogenized and pressed into pellets with a diameter of 5 mm (2 t, 120 s). The choice of the right crucible is important, since metallic crucibles (Nb, Ta, W) react with sulfur and boron, while oxidic crucibles (Al₂O₃ or ZrO₂) result in the formation of the corresponding metal oxide. An induction furnace was used for the heating. After each reaction step, the samples were homogenized, and the reaction progress was checked by PXRD.

The Zr₂SB pellet was welded in a niobium crucible on a tungsten plate and heated to 350 °C within 10 min with a dwell time of 10 h, before the temperature was increased to 1600 °C within 4 h. After a reaction time of 4 h, the temperature was decreased to 1000 °C within 4 h prior to shutting off the induction furnace. To improve the phase homogeneity, the sample was heated again at 1600 °C for 4 h. Zr₂SB was obtained as black polycrystalline powder, which is stable in air.

Similar reaction conditions were applied for the synthesis of Hf₂SB. However, the hafnium compound was prepared directly in the niobium crucible and already formed at 1400 °C. In addition, three reaction steps with a dwell time of 10 h each were necessary for the synthesis of black polycrystalline Hf₂SB, which is also stable in air.

Powder X-ray diffraction was performed using a Huber G670 diffractometer equipped with an oscillating plate sample holder, Cu-K α radiation ($\lambda = 1.54059 \text{ \AA}$), and a Ge-111 monochromator. Structural parameters and sample compositions were determined by Rietveld refinement using the TOPAS software package.^[56] Resistivity and magnetization measurements were performed with a Quantum Design PPMS-9. The vibrating sample magnetometer option was used for the determination of the magnetic properties. Temperature-dependent measurements were con-

ducted between 2 and 300 K with applied fields of 0.05 kOe and 30 kOe. For resistivity measurements, the samples were pressed into pellets with a diameter of 5 mm and a thickness of ~ 1 mm. The pellets were sintered at 1000 °C for 48 h and contacted using the Wimbush press contact assembly for van-der-Pauw measurements.^[37]

First principle calculations were performed with the VASP package using DFT with plane-wave basis sets and the generalized-gradient approximation (GGA) for contributions of correlation and exchange.^[38-41] LOBSTER was used to project the PAW eigenstates onto localized crystal orbitals.^[42] Chemical bonding was analyzed by the COHP method.^[65] The Bader analysis implemented by Henkelman et al. was used to extract charges from the electron density distributions.^[66-67] Elastic tensors were calculated by finite distortions of the crystal structure.^[68] Bulk (B) and Shear (G) moduli were determined using the Voigt-Reuss-Hill approximations.^[69-71] Young's moduli (E) and Poisson's ratios (ν) were calculated from B and G .^[17, 51] The Debye temperatures (Θ_D) were determined from the average sound velocity of polycrystalline samples, which can be derived from B and G .^[72]

Results and Discussion

Synthesis and Crystal structure

Zr₂SB and Hf₂SB were synthesized via solid-state reactions at high temperatures in an induction furnace. Zr₂SB forms a crystalline black powder, which is stable in air. Rietveld refinement of the powder diffraction data confirmed the Cr₂AlC-type structure and revealed a sample composition of 85 wt.-% Zr₂SB and 15 wt.-%, ZrB₂ (Figure 2-9 left). The pattern shows weak additional unidentified reflections. Most likely, sulfur reacted with the crucible materials niobium and tungsten.

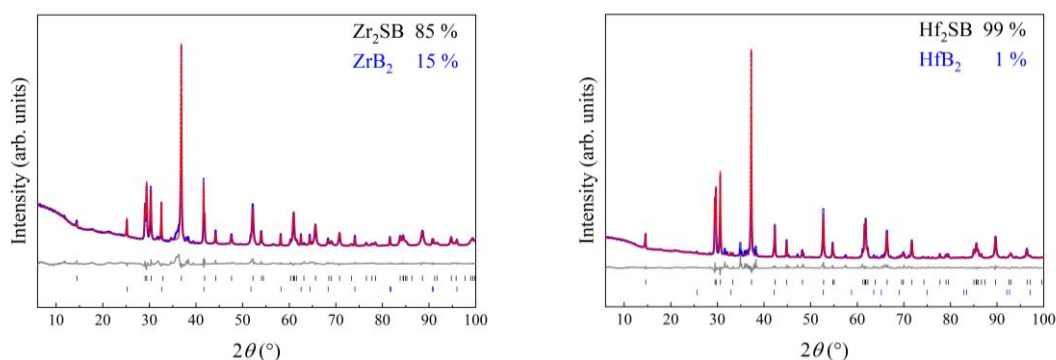


Figure 2-9: Powder X-ray diffraction pattern (blue) of Zr₂SB (left) and Hf₂SB (right) including Rietveld fit (red), difference curve (grey) and reflection positions for Zr₂SB, ZrB₂ and Hf₂SB, HfB₂. Phase fractions are given in wt.-%.

Hf₂SB samples are likewise black crystalline powders. Rietveld refinements indicate higher purity of 99 wt.-% Hf₂SB with 1 wt.-% HfB₂ and again traces of unidentified impurity phases (Figure 2-9 right). Crystallographic data and relevant interatomic distances are compiled in Table 2-3.

Given that the MAX phase sulfur-carbides M_2SC exist with $M = \text{Ti, Zr, Hf, Nb}$, one may expect all analogous borides with these elements. Nb₂SB was recently reported, and this work adds Zr₂SB and Hf₂SB. However, attempts to synthesize Ti₂SB remained unsuccessful so far.^[64]

Table 2-3: Crystallographic data of Zr₂SB and Hf₂SB.

Chemical formula	Zr ₂ SB	Hf ₂ SB			
M (g·mol ⁻¹)	225.32	399.96			
Crystal system, Space group	hexagonal, $P6_3/mmc$ (194)				
T (K)	293				
a (Å), c (Å)	3.5001(1), 12.2712(2)	3.4671(1), 12.1046(2)			
V (Å ³)	130.187(5)	126.012(3)			
Z	2				
Radiation type	Cu-K α_1 ; $\lambda = 1.54059$ Å				
Diffractometer	Huber G670				
Monochromator	Ge-111				
R_p	4.886	2.604			
R_{wp}	6.526	3.748			
Goodness of fit	1.780	1.838			
Z_M	0.6060(1)	0.6047(1)			
α_r	1.086	1.102			
Selected interatomic distances (Å)					
S — 6 x M	2.6844(3)	2.6643(3)			
B — 6 x M	2.4032(4)	2.3688(2)			
M — 3 x M	3.5001(1)	3.4666(1)			
Atom positions and equivalent isotropic displacement parameters (Å ²)					
Atom	x	y	z	U_{eq}	occ
M	1/3	2/3	z_M	0.5	1
S	1/3	2/3	1/4	1	1
B	0	0	0	3	1

Zr₂SB and Hf₂SB crystallize in the hexagonal space group $P6_3/mmc$ (Table 2-3), where layers of edge-sharing M_6B ($M = \text{Hf, Zr}$) octahedra alternate with layers of sulfur. For a direct comparison of the crystal structures, we have reproduced the analogous carbides Zr₂SC ($a = 3.4117(1) \text{ \AA}$, $c = 12.1452(2) \text{ \AA}$, $z_{\text{Zr}} = 0.6013(1)$) and Hf₂SC ($a = 3.3695(1) \text{ \AA}$, $c = 12.0172(2) \text{ \AA}$, $z_{\text{Hf}} = 0.6004(1)$).^[73-74] The borides exhibit slightly larger unit cells. The a -axes of Zr₂SB and Hf₂SB are 2.6 % and 2.9 % longer compared to the carbides, respectively. The c -axes increase by 1.0 % in the case of Zr₂SB and 0.7 % for Hf₂SB. These changes are similar to the recently published findings for Nb₂SB_xC_{1-x}, even though the enlargement of the unit cells are bigger in the Hf- and Zr-borides compared to the Nb-compound.^[64] Selected interatomic distances are listed in Table 2-3. While the $M - \text{S}$ distances do not change significantly (Zr₂SB +0.5 %; Hf₂SB +0.6 %), the $M - X$ (Zr₂SB +3.5 %; Hf₂SB +3.5 %) and the $M - M$ (Zr₂SB +2.6 %; Hf₂SB +2.9 %) distances increase compared to the carbides.^[75] The distortion of the M_6X ($M = \text{Hf, Zr}$; $X = \text{B, C}$) octahedra is quantified by the value α_r .^[47]

$$\alpha_r = \frac{\sqrt{3}}{2 \sqrt{4 z_M^2 (c/a)^2 + 1/12}} \quad \text{Equation 2-2}$$

An ideal octahedron gives $\alpha_r = 1$. In Zr₂SX ($X = \text{B, C}$), α_r is 1.114 for the carbide and 1.086 for the boride. The same trend occurs for the hafnium compounds, where α_r is 1.121 for Hf₂SC and 1.102 for Hf₂SB. Thus, the octahedra are less distorted in the borides than in the carbides, which confirms the results of Nb₂SX ($X = \text{B, C}$).

Physical Properties

The MAX phases show a unique combination of ceramic and metallic properties. The latter emerge from d-orbital interactions of the M elements at the Fermi level. Therefore, these phases are good electronic and thermal conductors, which sometimes are even better than the pure M elements.^[48, 56-57, 76-77]

The electrical dc resistivities of Zr₂SB and Hf₂SB were determined in the temperature range of 2 - 300 K (Figure 2-10 left). Both MAX phases show a linear increase of the resistivity with the temperature from 100 K to 300 K and therefore are metallic conductors. The resistivity of the Zr₂SB sample at room temperature ($9.9 \cdot 10^{-6} \text{ \Omega m}$) is larger than for Hf₂SB ($1.2 \cdot 10^{-6} \text{ \Omega m}$). This is unexpected since zirconium and hafnium compounds usually have similar properties. Even though the sample preparation and the measurement method were identical, other factors can

affect the data. The absolute values of the resistivity are highly sensitive to grain-boundary effects, which might also explain the difference to typical values of other MAX phases ($2 - 7 \cdot 10^{-7} \Omega\text{m}$).^[48, 77] Furthermore, impurities in the Zr_2SB sample probably affects the resistivity data.

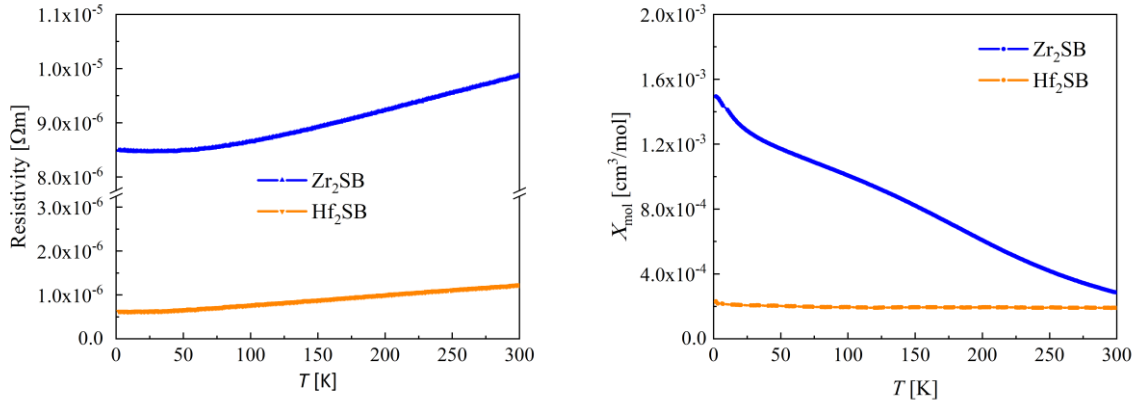


Figure 2-10: Left: Resistivities determined by van der Pauw measurements in the temperature range 2 – 300 K for Zr_2SB (blue) and Hf_2SB (orange). Right Magnetic susceptibilities of Zr_2SB and Hf_2SB in the temperature range of 2 – 300 K at an applied field of 3 T.

The molar magnetic susceptibilities of Zr_2SB and Hf_2SB at an applied field of 3 T between 2 and 300 K are shown in Figure 2-10 right. Hf_2SB exhibits small positive values, which are temperature independent. Therefore, the hafnium boride is a Pauli paramagnet. The trend of Zr_2SB shows an almost linear increase of the molar susceptibility with decreasing temperature. Furthermore, the absolute values are larger than those for Hf_2SB . Nevertheless, it is not the trend of a Curie-Weiss paramagnet, and the values are still rather small. The deviating susceptibility of the Zr_2SB sample is most likely affected by impurity phases.

Electronic Structure and elastic Properties

Ab-initio calculations of the electronic structures of Zr_2SB and Hf_2SB reveal similar results. Figure 2-11 shows the band structure and density-of-states of Zr_2SB , which conforms to the metallic state. The bands crossing at the Fermi-level have mainly Zr-4d character with small contributions of B-2p , showing that the metallic property of Zr_2SB emerges in the layers of $\text{Zr}_{6/3}\text{B}$ octahedra as typical for MAX phases. Sulfur is the most electronegative component, and the $\text{S-3s}/3\text{p}$ states are largely occupied (Figure 2-11), which indicates a rather ionic bonding character between the layers of sulfur atoms and the Zr_2B layers.

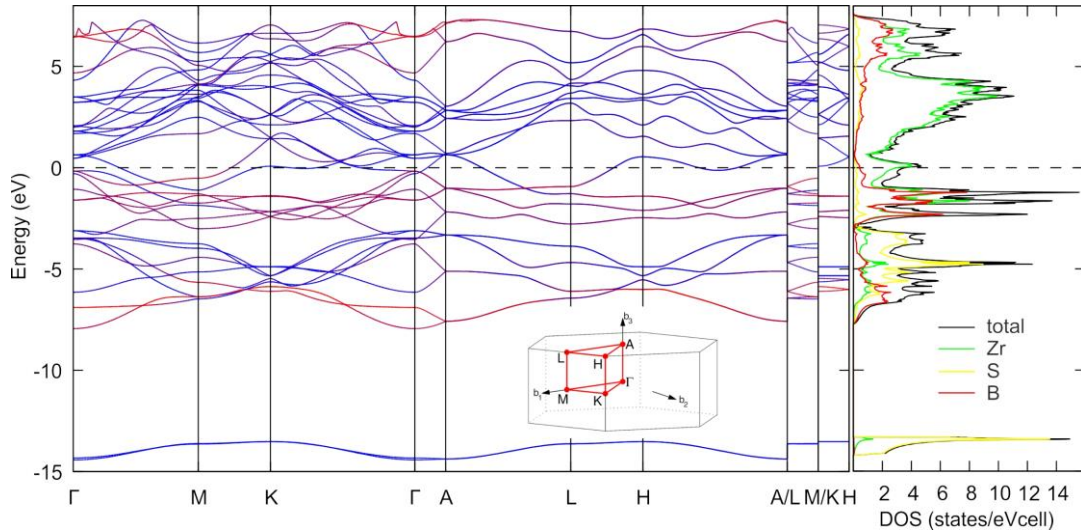


Figure 2-11: Band structure and density-of-states of Zr_2SB . The red component in the bands plot is proportional to the boron contribution. The total and atom-resolved DOS represents an LCAO projection of the PAW eigenstates.

Table 2-4 shows the results of the structure relaxations, atom charges, and bond energies. For comparison, we have calculated the data for Zr_2SC . The PBE functional reproduces the experimental lattice parameters within 1 %. The relatively high atom charges indicate a predominant ionic bonding character. The X atoms carry the highest negative charges, which means that the $M-X$ bonds are the strongest from an electrostatic point of view. The $M-X$ bonds also reveal the largest ICOHP bonding energy. The charges and bond energies are similar for both borides and the carbide. Thus, this analysis allows no big differences in the bonding characteristics between the borides and the carbide.

Table 2-4: Calculated lattice parameters and coordination of the metal atom z_M (experimental values are given in brackets below), atom charges, and ICOHP bond energies of M_2SB ($M = Zr, Hf$) and Zr_2SC .

	Structure		z_M	Atom charges			ICOHP energies (eV/bond)		
	a (Å)	c (Å)		q_M	q_S	q_B	$M-X$	$M-S$	$M-M$
Zr_2SB	3.519 [3.5001]	12.317 [12.2712]	0.6055 [0.6060]	+1.29 ^D +1.64 ^B	-0.88 ^D -1.32 ^B	-1.70 ^D -1.96 ^B	-0.81	-0.49	-0.07
Hf_2SB	3.482 [3.4671]	12.137 [12.1046]	0.6038 [0.6047]	+1.46 ^D +1.67 ^B	-0.91 ^D -1.33 ^B	-2.02 ^D -2.00 ^B	-0.79	-0.54	-0.09
Zr_2SC	3.423 [3.4117]	12.226 [12.138]	0.6006 [0.6013]	+1.20 ^D +1.71 ^B	-0.92 ^D -1.33 ^B	-1.48 ^D -2.09 ^B	-0.83	-0.49	-0.10

^D from DOS integrations

^B from Bader analysis

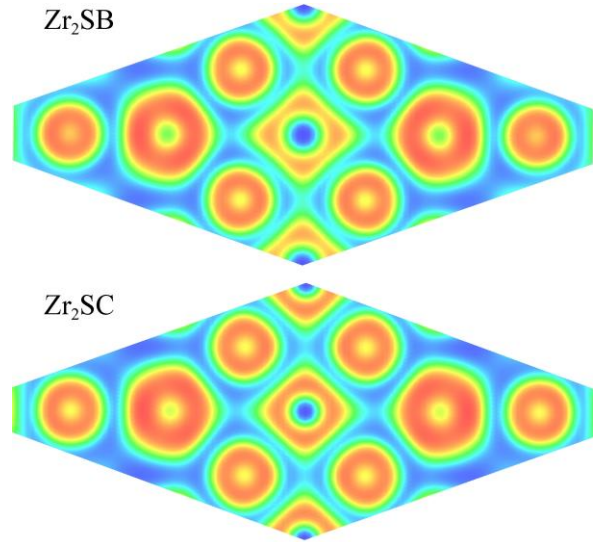


Figure 2-12: Electron localization function (ELF) plotted on the $(1 \ -1 \ 3.3123)$ planes of Zr_2SB (top) and Zr_2SC (bottom). Four zirconium atoms surround the X atoms (B or C) in the center. The largest circles are the sulfur atoms with the highest localization intensity.

Figure 2-12 shows the electron localization functions (ELF) of Zr_2SB and Zr_2SC plotted on a layer intersecting the Zr_6X octahedra with the X atoms in the centers of the plots surrounded by four zirconium atoms. The mainly ionic bonding character becomes evident by the rather spherical localization areas around all atoms. A higher localization is discernable around the carbon atoms, which indicates a stronger electrostatic $Zr - X$ interaction.

The elastic tensors were determined from finite distortions of the lattice, and the elastic constants were derived from the strain-stress relationship for Zr_2SB and Hf_2SB . Tables 2-5 and 2-6 show the results together with data for Nb_2SB from the literature. Hexagonal systems exhibit five independent elastic constants C_{11} , C_{12} , C_{13} , C_{33} , and C_{44} (Table 2-5).^[68] All compounds satisfy the mechanical stability criteria for hexagonal crystals: $C_{11} > |C_{12}|$, $C_{44} > 0$, and $(C_{11} + C_{12}) C_{33} - 2C_{13}^2 > 0$.^[78]

Table 2-5: Elastic constants C_{ij} (GPa) of M_2SB ($M = Nb, Zr, Hf$).

	C_{11}	C_{12}	C_{13}	C_{33}	C_{44}	Ref.
Nb_2SC	301	105	157	314	116	[64]
Nb_2SB	316	95	131	317	143	[64]
Zr_2SC	326	103	119	351	160	[75]
Zr_2SB	261	79	80	282	117	This work
Hf_2SC	344	116	138	369	175	[75]
Hf_2SB	286	79	84	296	122	This work

Bulk (B) and Shear (G) moduli were estimated using the Voigt (V) and Reuss (R) schemes, where V is the upper and R the lower limit.^[69-72] The mean of these values gives the final B and G , respectively, which were used to calculate the Young's moduli (E) and the Poisson's ratios (ν) (Table 2-6). The strength of the $M - X$ and $M - S$ bonds affect the elastic constants and thus the Bulk, Shear, and Young's moduli.^[79] All borides show smaller values of B , G , and E compared to the corresponding carbides, whereat B distinctly decreases for the zirconium and hafnium compounds (Table 2-6). This confirms the results from previous calculations for example of M_2AlX ($M = Sc, Ti, Zr, Hf, V, Nb, Ta, Cr, Mo; X = B, C, N$) and M_2AB ($M = Ti, Zr, Hf; A = Al, Ga, In$).^[17, 19] The ductility or brittleness of materials can be deduced from the B/G ratios. Ductile compounds exhibit values above 1.75, while lower values indicate brittleness.^[80-81] All M_2SX compounds ($M = Zr, Hf, Nb; X = C, B$) are brittle, which is slightly more pronounced in the borides (Table 2-6). The Debye temperature is a quantity for the melting point and the thermal conductivity.^[82] Contrary to Nb_2SX ($X = B, C$), M_2SX ($M = Zr, Hf; X = C, B$) exhibits lower Debye temperatures (Θ_D) for the borides, which indicates lower thermal conductivities and melting points.

The Poisson's ratio gives a general estimate of the bonding characteristics. Common values of covalent compounds are approximately 0.1, of ionic 0.25 and of metallic 0.33.^[51, 81, 83-84] The Poisson's ratios of M_2SX ($M = Zr, Hf, Nb; X = C, B$) are given in Table 2-6 and show that the bonding character in these materials is essentially ionic, which agrees with the results from the charge and ELF analysis.

Table 2-6: Bulk moduli B (GPa), Shear Moduli G (GPa), Young's moduli E (GPa), Poisson's ratios ν , B/G ratios, linear compressibility ratios f and Debye temperature Θ of M_2SX ($M = Zr, Hf, Nb; X = C, B$).

	B	G	E	ν	B/G	f	Θ_D	Ref.
Nb_2SC	194	97	249	0.285	1.99	0.59	521	[64]
Nb_2SB	186	116	287	0.241	1.60	0.80	573	[64]
Zr_2SC	187	128	313	0.221	1.46*	0.82*	603	[75]
Zr_2SB	142	102	247	0.211	1.39	0.89	548	This work
Hf_2SC	204	134	330	0.231	1.52*	0.80*	463	[75]
Hf_2SB	151	111	267	0.206	1.36	0.93	426	This work

*calculated by literature values

The linear compressibility ratio $f = k_c/k_a$ characterizes the anisotropy. For an isotropic crystal, the f index is 1. If $f < 1$, the compressibility along a -axis is larger than along the c -axis and vice versa for $f > 1$.^[85] For layered materials, this can be used as a measure of anisotropy. A large f index indicates a strong bonding in the ab plane, while a value close to 1 rather supports a three-

dimensional structure. The linear compressibility ratios of Zr_2SB and Hf_2SB are smaller than unity, and, therefore, these MAX phases are stiffer along the c -axis than in the ab plane. This indicates a strong $M-A$ interaction and a less pronounced two-dimensionality compared to the carbides.

Conclusions

The new MAX phase borides Zr_2SB and Hf_2SB form by heating the elements at 1400 – 1600 °C. X-ray powder diffraction data confirm the Cr_2AlC -type structure ($P6_3/mmc$) with larger unit cells and less distorted M_6X octahedra compared to the known carbides. The new borides are metallic conductors and Pauli paramagnets. DFT calculations confirm the metallic state and reveal predominantly ionic bonds, which are slightly weaker than in the carbides. The elastic constants indicate that Zr_2SB and Hf_2SB are brittle and exhibit a less two-dimensional character compared to other MAX phases. The bulk moduli are slightly smaller than in the carbides in agreement with the weaker bonding.

2.3 Further MAX phase borides – the solid solutions $\text{Nb}_2\text{A}(\text{B,C})$ ($\text{A} = \text{As, In, Sn}$)

Abstract

The MAX phase borides $\text{Nb}_2\text{A}(\text{B,C})$ ($\text{A} = \text{As, In, Sn}$) crystallize in the hexagonal space group $P6_3/mmc$ (Cr_2AlC -type). While the solid solutions $\text{Nb}_2\text{As}(\text{B,C})$ were synthesized via solid-state reaction, $\text{Nb}_2\text{A}(\text{B,C})$ ($\text{A} = \text{Sn, In}$) were synthesized using a flux of excess tin and indium, respectively. Although the incorporation of boron in $\text{Nb}_2\text{AB}_xC_{1-x}$ ($\text{A} = \text{As, In, Sn}$) was proven, we have not been able to determine x yet. Magnetic measurements reveal that none of the synthesized phases show superconductivity. Instead, the boundary phases Nb_2AC ($\text{A} = \text{As, In, Sn}$) and the solid solutions are Pauli paramagnets. Further, $\text{Nb}_2\text{SnB}_xC_{1-x}$ can form a protective layer of Nb_3Sn , which provides a thin superconducting surface with $T_c = 18$ K and makes it remarkably inert against strong acids.

Introduction

$M_{n+1}AX_n$ is the chemical formula of a large group of compounds called the MAX phases. M is an early transition metal (24 different elements known), and A is an A-group element (18 different elements known), and X is boron, carbon, or nitrogen. This variety of elements leads to 87 known ternary combinations, of which some were found quite recently.^[86-91] The possibility of forming solid solutions further extends the group of MAX phases. Furthermore, they enable the optimization of desired properties and is, therefore, the subject of current research.

The variety of potential solid solutions is very large at the M and A site.^[92-99] With the X site, on the other hand, only a few examples are known. $\text{Ti}_2\text{Al}(\text{C}_x\text{N}_{1-x})_y$ ($x = 0 - 1$; $y < 0.2$) and $\text{Ti}_3\text{Al}(\text{C}_{0.5}\text{N}_{0.5})_2$ are the only two representatives of those.^[12-13, 62, 100-101] The MAX phase borides described in chapter 2.1 and 2.2 open up the possibility for further solid solutions, especially since elementary boron is easier to handle than nitrogen or oxygen.

A difficulty in the synthesis of solid solutions containing boron, could be the existents of another group of compounds, the MAB phases, which are closely related to the MAX phases. Beside comparable physical properties, they share a similar elemental composition. Both the Cr_2AlC (MAX phases) and the Mn_2AlB_2 (MAB phases) structure type exhibit layered crystal structures, but the coordination polyhedron of the X atom is different. While in MAX phases the M_6X polyhedron is an octahedron, MAB phases form layers of trigonal prisms with B – B

bonds.^[27-28, 31, 63, 102] Therefore, it is questionable whether solid solutions of carbon and boron are possible or whether the formation of two different phases is preferred.

This chapter focuses on the substitution of carbon by boron in superconducting MAX phases, $\text{Nb}_2\text{A}(\text{B,C})$ ($\text{A} = \text{As, In, Sn}$). Superconductivity in MAX phases is a less examined phenomena. The critical temperatures ($T_{c,\text{max}} = 10 \text{ K}$, Nb_2GeC) of these phases are rather low.^[46, 55, 86, 103-107] As shown in chapter 2.1, T_c decreases with the boron content in $\text{Nb}_2\text{S}(\text{B,C})$. DFT calculations indicate that this decrease in the critical temperature is due to the decrease of the electron density at the Fermi level (ε_F). The change of the phonon density plays a minor role.^[64]

Subsequently, the synthesis of the solid solutions $\text{Nb}_2\text{A}(\text{B,C})$ ($\text{A} = \text{In, Sn, As}$) is described. The products were characterized by means of PXRD using Rietveld refinement. Although boron was likely incorporated into these compounds, the current data does not reveal the amount of boron in the phases.

Experimental

For the synthesis of $\text{Nb}_2\text{A}(\text{B,C})$ ($\text{A} = \text{As, In, Sn}$), different methods were applied. $\text{Nb}_2\text{As}(\text{B,C})$ were synthesized via solid-state reaction of the elements. Stoichiometric mixtures of niobium (99.99 %, ~325 mesh, Alfa Aesar), arsenic (99.999 %, lump, Alfa Aesar), graphite (100 %, powder, ACROS Organics) and boron (99%, powder, Koch-Light-Laboratories) were homogenized and pressed to pellets with a diameter of 5 mm (2 t, 5 min). The samples were placed in an alumina crucible and sealed in an argon-filled silica tube. The reaction took place in a chamber furnace. Within 4 h, the mixtures were heated to 1200 °C. After a reaction time of 15 h, they were allowed to cool down to room temperature in the oven.

For flux synthesis of $\text{Nb}_2\text{A}(\text{B,C})$ ($\text{A} = \text{In, Sn}$), the elements niobium (99.99 %, ~325 mesh, Alfa Aesar), boron (99 %, powder, Koch-Light- Laboratories) and graphite (100 %, powder, ACROS Organics) were stoichiometrically weighed and transferred into an alumina crucible. An excess of indium (99.99 %, balls, Alfa Aesar) or tin (99.8 %, balls, Alfa Aesar), about four times more, was added. The reaction mixtures were sealed in an argon-filled silica tube. The samples were heated to 1100 or 1200 °C at 200 °C/h and reacted for 130 h at this temperature. Then they were slowly cooled (10 °C/h) to 900 °C and to room temperature at 200 °C/h. The excess of indium or tin was dissolved in concentrated hydrochloric acid. The products were washed twice each with water and ethanol and then dried in air.

The reaction progress was checked by PXRD. If necessary, the sample was reacted again under the same conditions. In the case of In and Sn, the corresponding metal was again added as flux.

$\text{Nb}_2\text{A}(\text{B,C})$ ($\text{A} = \text{As, In, Sn}$) were obtained as black powders with phase fractions of 48 – 100 wt.%.

PXRD patterns were recorded using a Huber G670 diffractometer with $\text{Cu-K}_{\alpha 1}$ radiation ($\lambda = 1.54059 \text{ \AA}$) and a Ge-111 monochromator. Rietveld refinement and the TOPAS software package were used to examine the change in crystal structure.^[108] The magnetic properties were determined using either a Quantum Design PPMS-9 with VSM option or an AC susceptometer. The measurements were performed in a temperature range of 1.9 to 30 K and external magnetic fields of 3 or 15 Oe.

Results and discussion

Synthesis and crystal structure

The synthesis of Nb_2AsC was first described by Beckmann *et al.*, whereby the desired product was obtained from the elements by means of a solid-state reaction at 1150 °C.^[109] Later it was prepared by hot isostatic pressing of niobium, arsenic, and graphite powders at 1300 °C at a pressure of 50 MPa.^[110] Herein, we report on the syntheses of $\text{Nb}_2\text{AsB}_x\text{C}_{1-x}$ ($x = 0 - 0.8$) via solid-state reaction at 1200 °C, starting from the elements. Although the MAX phases were already the main components of the samples after the first reaction step, they were annealed three more times at the same temperature to increase the phase fraction.

Table 2-7: Results of the Rietveld refinement of $\text{Nb}_2\text{AsB}_x\text{C}_{1-x}$ ($x = 0 - 0.8$).

x	MAX Phase (wt.%)	Impurity phase(s) (wt.%)
0	Nb_2AsC (100)	
0.2	$\text{Nb}_2\text{AsB}_{0.2}\text{C}_{0.8}$ (85)	NbC (10), NbAs (3), $\text{Nb}_3\text{As}_2\text{C}$ (2)
0.4	$\text{Nb}_2\text{AsB}_{0.4}\text{C}_{0.6}$ (79)	NbAs (8), NbC (7), NbB (5), $\text{Nb}_3\text{As}_2\text{C}$ (2)
0.6	$\text{Nb}_2\text{AsB}_{0.6}\text{C}_{0.4}$ (73)	NbAs (12), NbB (12), $\text{Nb}_3\text{As}_2\text{C}$ (3)
0.8	$\text{Nb}_2\text{AsB}_{0.8}\text{C}_{0.2}$ (48)	NbAs (24), NbB (24), $\text{Nb}_3\text{As}_2\text{C}$ (4)

The results of the Rietveld refinement are listed in Table 2-17. $\text{Nb}_2\text{AsB}_x\text{C}_{1-x}$ ($x = 0 - 0.8$) were black powders with phase fractions of 48 – 100 wt.%, which decreases with increasing boron content. Targeting the corresponding ternary boride Nb_2AsB , the reaction of the elements resulted in the formation of NbAs and NbB.

The B/C mixed occupancy at the X site cannot be refined from PXRD data. As shown in chapter 2.3, the change in crystal structure could be a good criterion for the degree of substitution. Figure 2-13 displays that the a -axis increases with the boron content, while the c/a ratio decreases (see Figure 2-13). The latter is due to the almost unchanged length of the c -axis. Besides the cell dimensions, the position of the niobium atom z_M also shifted. This shift causes a change in the distortion of the M_6X octahedra, which can be traced utilizing the α_r value. For a detailed explanation of this value, see chapter 2.1.

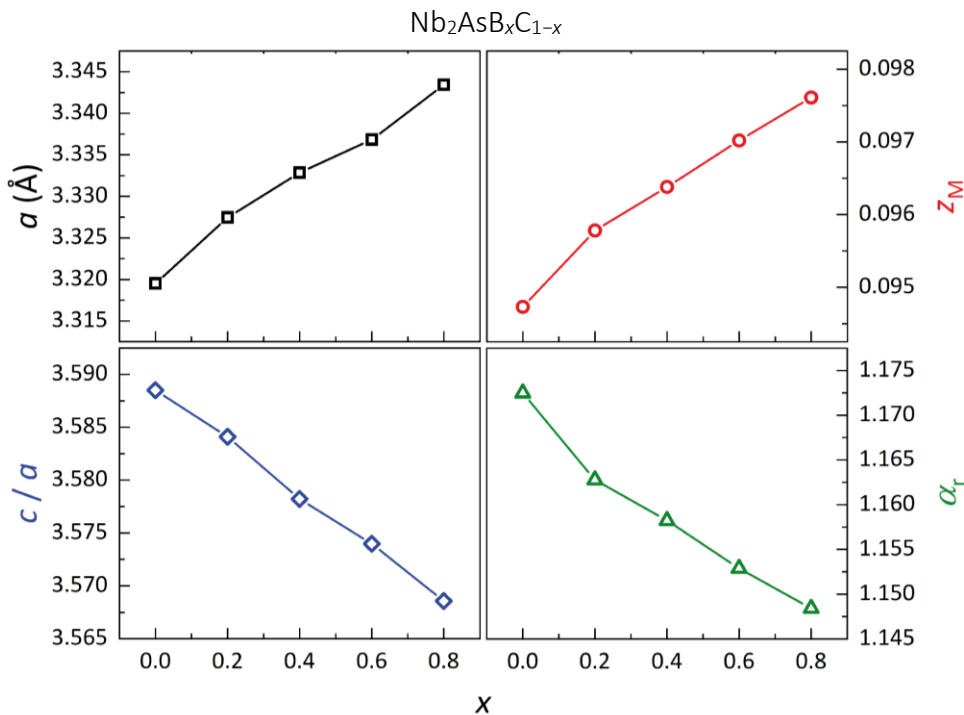


Figure 2-13: Change of the crystal structure in $\text{Nb}_2\text{AsB}_x\text{C}_{1-x}$ ($x = 0 - 0.8$) displayed by the a -axis (black), the z coordinate of the metal M (red), the c/a -axes ratio (blue) and the value for the degree of distortion of the M_6X octahedra α_r (green). The error bars are smaller than the spot sizes.

For an ideal octahedron $\alpha_r = 1$, which means that the distortion decreases with the boron content (see Figure 2-13 green). This results in a shortened $M - A$ distance and thus in a stronger $M - A$ interaction, indicating an increased three-dimensionality in the boron MAX phases. These trends, those of cell dimensions and M_6X distortion, are consistent with the results for $\text{Nb}_2\text{S}(\text{B,C})$, Zr_2SB , and Hf_2SB . Nevertheless, x in $\text{Nb}_2\text{AsB}_x\text{C}_{1-x}$ could have a large error since there are boron-containing impurity phases for $x \geq 0.4$, and the boundary phase Nb_2AsB could not be synthesized.

For the syntheses of $\text{Nb}_2\text{A}(\text{B,C})$ ($\text{A} = \text{Sn, In}$), another method was chosen. Even though Nb_2AC ($\text{A} = \text{Sn, In}$) can also be synthesized via solid-state reaction as described in the literature, we found that the reactivity increases by using a tin and indium excess as flux, respectively.^[1, 104, 106] This results in an increased phase proportion of the MAX phase within the same reaction time.

Table 2-8: Phase proportions determined from Rietveld refinement for the samples of $\text{Nb}_2\text{AB}_x\text{C}_{1-x}$ ($\text{A} = \text{Sn, In}$; $x = 0 - 0.8$) and the yield for $\text{Nb}_2\text{InB}_x\text{C}_{1-x}$ ($x = 0 - 0.8$).

x	MAX Phase (wt.%)	Impurity phase(s) (wt.%)	Yield (%)
0	Nb_2SnC (100)		-
0.2	$\text{Nb}_2\text{SnB}_{0.2}\text{C}_{0.8}$ (100)		-
0.4	$\text{Nb}_2\text{SnB}_{0.4}\text{C}_{0.6}$ (97)	NbB (3)	-
0.6	$\text{Nb}_2\text{SnB}_{0.6}\text{C}_{0.4}$ (95)	NbB (5)	-
0.8	$\text{Nb}_2\text{SnB}_{0.8}\text{C}_{0.2}$ (71)	NbB (22), NbO (7)	-
0	Nb_2InC (94)	NbC (4), NbO (2)	72
0.2	$\text{Nb}_2\text{InB}_{0.2}\text{C}_{0.8}$ (94)	NbC (3), NbO (3)	76
0.4	$\text{Nb}_2\text{InB}_{0.4}\text{C}_{0.6}$ (100)		74
0.6	$\text{Nb}_2\text{InB}_{0.6}\text{C}_{0.4}$ (100)		83
0.8	$\text{Nb}_2\text{InB}_{0.8}\text{C}_{0.2}$ (-)	unknown	70

The powders were analyzed by PXRD, and the data was refined using the Rietveld method. The MAX phases were synthesized with phase proportions ranging from 71 to 100 wt.% (see Table 2-8 and Figure A-14 – A-23). The remaining tin or indium was dissolved in concentrated hydrochloric acid. During this dissolution process, possibly contained impurity phases might also be dissolved. In the case of $\text{Nb}_2\text{InB}_{0.8}\text{C}_{0.2}$, additional reflections with high intensities were observed, which could not be assigned to a known compound (Figure A-18). These reflections are very broad, which indicates a poor crystallinity. Therefore, it is likely that this impurity formed during the dissolution.

For the synthesis of $\text{Nb}_2\text{A}(\text{B,C})$ ($\text{A} = \text{Sn, In}$) the use of flux has another advantage. Due to the higher mobility of the reaction components in the liquid tin and indium, respectively, the homogeneity increases. This is proven by a decreased width of the reflections in the PXRD patterns (Figure 2-14). For $\text{Nb}_2\text{Sn}(\text{B,C})$, the FWHM decreases by about 48% and for $\text{Nb}_2\text{In}(\text{B,C})$, about 24 %, if using a flux for the synthesis.

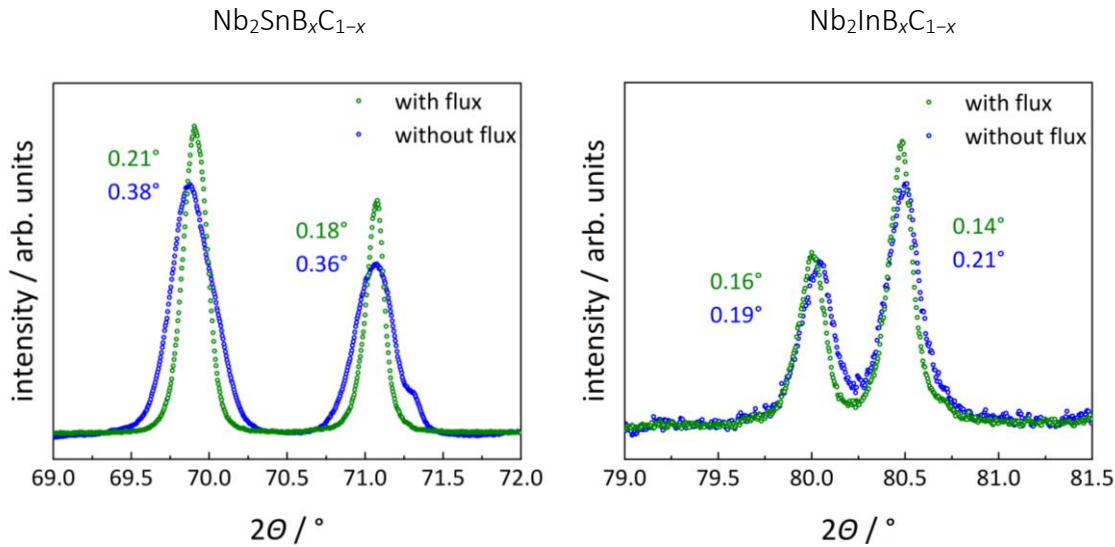


Figure 2-14: Comparison of peak broadening in the PXRD pattern after synthesis with and without flux with an indication of the half-value widths next to the reflections. [019] and [116] reflections of $\text{Nb}_2\text{SnB}_{0.4}\text{C}_{0.6}$ (left) and of $\text{Nb}_2\text{InB}_{0.2}\text{C}_{0.8}$ (right).

For $\text{Nb}_2\text{SnB}_x\text{C}_{1-x}$ ($x = 0 - 0.8$), the same trend as for $\text{Nb}_2\text{SB}_x\text{C}_{1-x}$ and $\text{Nb}_2\text{AsB}_x\text{C}_{1-x}$ is found. An increased a -axis, as well as an increased ξ_M parameter of the metal site, leads to less distorted M_6X octahedra, which can be traced by the α_r value (see Figure 2-15). Nevertheless, the changes in the tin compounds are distinctly smaller compared to other boron carbides. Furthermore, the solid solution $\text{Nb}_2\text{SnB}_{0.8}\text{C}_{0.2}$ differs from the linear trend of $\text{Nb}_2\text{SnB}_x\text{C}_{1-x}$ ($x = 0 - 0.6$). The c -axis shortens, while the length of the a -axis and the ξ_M parameter increase more than the trend indicates. A stronger distorted M_6X octahedron causes this. The sudden change of the structure from $x = 0.6$ to $x = 0.8$ shows that the boron limit, which can be incorporated into the MAX phase structure, has been reached and maybe the reason why Nb_2SnB cannot be synthesized. Additionally, the large amount of NbB (22 wt.%) suggests that the nominal stoichiometry with $x = 0.8$ was not achieved.

For $\text{Nb}_2\text{InB}_x\text{C}_{1-x}$ ($x = 0 - 0.8$), no change in cell dimensions or distortion of the M_6X octahedron with increasing boron content was observed (see Figure 2-16). Therefore, it is questionable whether boron incorporates into Nb_2InC or whether the change of the unit cell is suitable here for tracing the substitution.

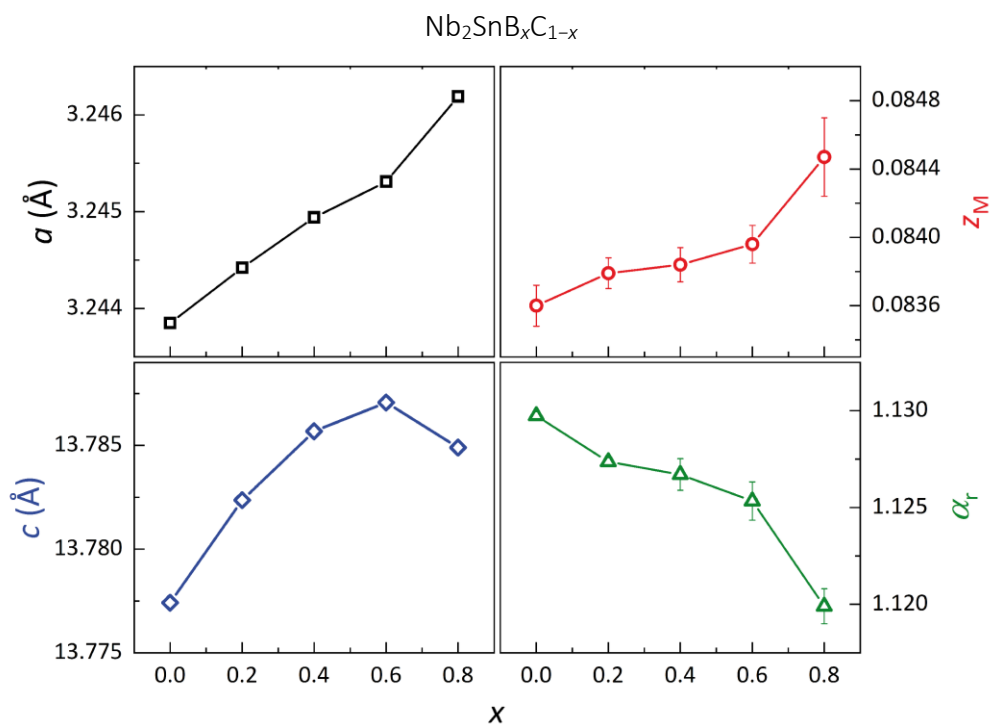


Figure 2-15: Change of the crystal structure in $\text{Nb}_2\text{SnB}_x\text{C}_{1-x}$ ($x = 0 - 0.8$) displayed by the a -axis (black), the z coordinate of the metal M (red), the c -axis (blue) and the value for the degree of distortion of the M_6X octahedra α_r (green). If the error bars are not shown, they are smaller than the spot sizes.

Nevertheless, the successful syntheses are shown by the yields of the reactions (see Table 2-8). These are in the range of 70 – 83 % and show no dependence on x , which indicates a systematic error within the synthesis method. Working steps where parts of the product may have been lost include incomplete emptying of the crucible, the dissolving process, and the subsequent washing steps, as well as residues in mortars and other tools. For example, on the assumption that no boron incorporates into the compound, a yield of only 40 % product could be achieved in the synthesis of $\text{Nb}_2\text{InB}_{0.6}\text{C}_{0.4}$. However, since the measured yield of 83 % is more than twice as high, the product must be a boron carbide. Therefore, the high phase proportions from the Rietveld refinement in combination with the high yields thus cause a mixed B/C occupancy on the X site. However, the exact proportion of boron in the solid solution cannot be determined.

Consequently, the incorporation of boron into the tin compound and especially into the indium only has a minor impact on the crystal structure of the MAX phase. As shown by calculations for $M_2\text{SB}$ ($M = \text{Zr}, \text{Hf}, \text{Nb}$) in chapters 2.1 and 2.2, the substitution with boron comes with a strengthening of the $M - A$ interaction. Maybe this interaction cannot change in $\text{Nb}_2A(\text{B},\text{C})$ ($A = \text{Sn}, \text{In}$) and, therefore, the system can only incorporate a limited amount of boron. In summary, a successful synthesis of $\text{Nb}_2A(\text{B},\text{C})$ ($A = \text{Sn}, \text{In}$) was confirmed, but the boron content in these solid solutions remains uncertain, as for $\text{Nb}_2\text{As}(\text{B},\text{C})$.

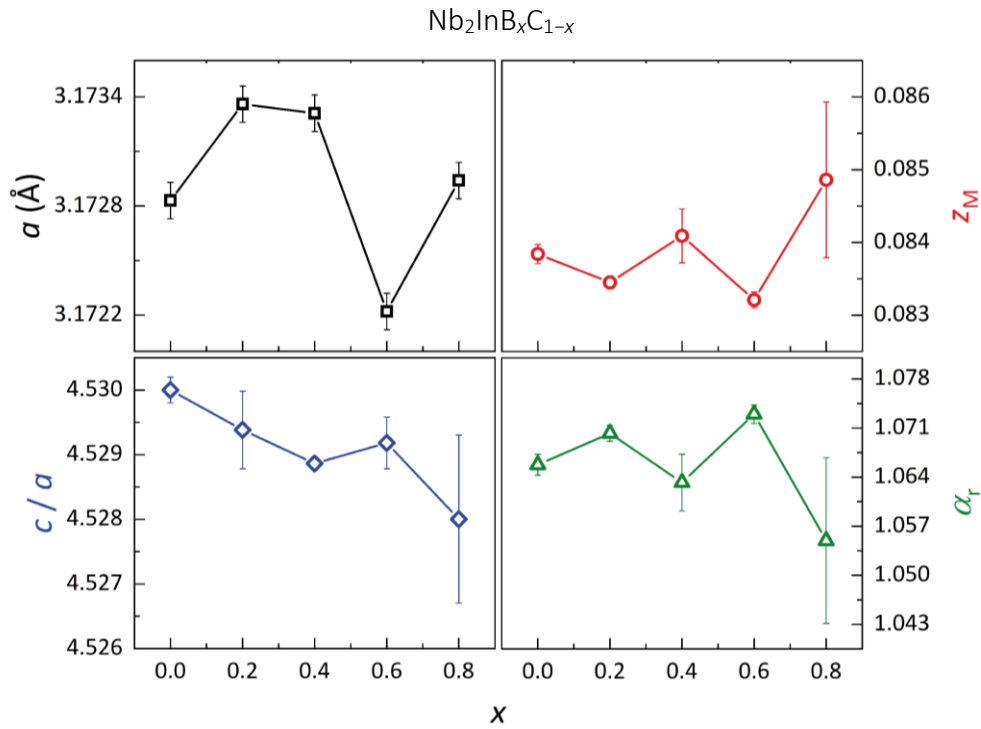


Figure 2-16: Change of the crystal structure in $\text{Nb}_2\text{InB}_x\text{C}_{1-x}$ ($x = 0 - 0.8$) displayed by the a -axis (black), the z coordinate of the metal M (red), the c/a -axes ratio (blue) and the value for the degree of distortion of the M_6X octahedra α_r (green). If the error bars are not shown, they are smaller than the spot sizes.

Magnetic properties

Superconductivity is a rather rare phenomenon among the MAX phases. However, it occurs more often in compounds with niobium as M element. Nb_2SnC , for example, shows a magnetic behavior, which depends on the synthesis method. Samples prepared at 2.5 GPa have a critical temperature of 7.8 K, whereas samples prepared under ambient pressure are not superconducting.^[106]

Also Nb_2SnC , synthesized by flux synthesis, does not show superconductivity (see Figure 2-13). The solid solutions $\text{Nb}_2\text{SnB}_x\text{C}_{1-x}$ exhibit two or three transitions one at $T_c = 18\text{K}$, which can be assigned to Nb_3Sn , one at $T_c = 3.8\text{K}$, which is due to undissolved tin and one at $T_c = 2.4\text{K}$. The latter cannot be assigned to the MAX phase due to the low volume fraction and the unchanged transition temperature for all solid solutions.

The decrease of the volume susceptibility at 18 K is too large, since the PXRd data show no presence of Nb_3Sn (see Table 2-8 and Figure A-19 – A-23). We assume that this is due to the dissolution process in concentrated hydrochloric acid, which decomposes the MAX phase on the

surface and forms Nb_3Sn . Consequently, this passivates the particle from the acid. In the magnetic field, this superconducting layer shields the entire particle, which leads to a virtual superconducting volume fraction. The measurements of the susceptibility in Figure 2-13 right prove this passivation. For these, the samples were homogenized with mortar and pestle after the dissolution process. This treatment cracks the passivized particles and, consequently, the volume fractions of the Nb_3Sn transitions significantly reduce. Passivation was also found for the MAX phases Ti_2AlC and Cr_2AlC , which can form Al_2O_3 protective layers and therefore withstand temperatures up to $1350\text{ }^\circ\text{C}$ in air.

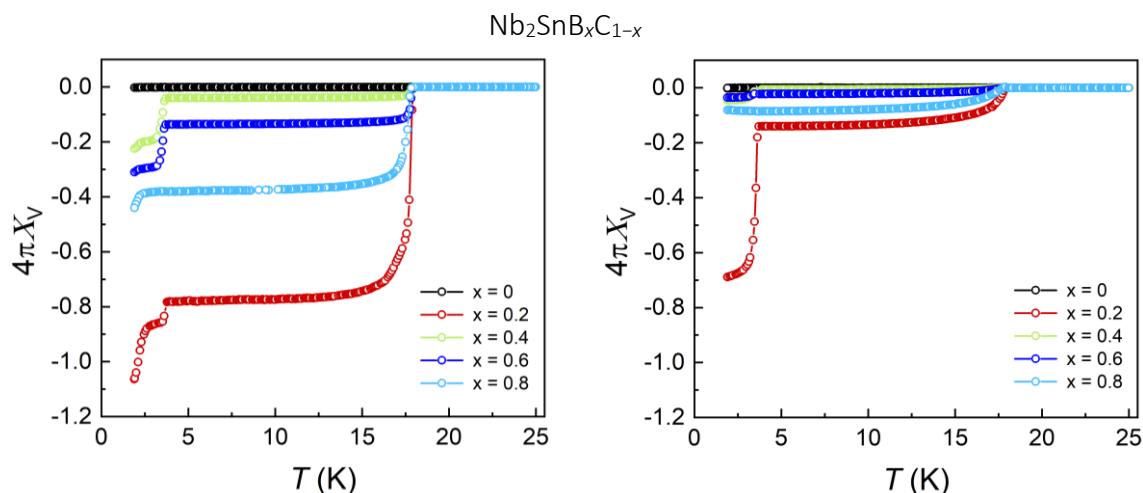


Figure 2-17: Susceptibility measurements of $\text{Nb}_2\text{SnB}_x\text{C}_{1-x}$ ($x = 0 - 0.8$) after being washed with concentrated hydrochloric acid (left) and of the same samples homogenized using a mortar and pestle (right).

The magnetic measurements of the solid solutions $\text{Nb}_2\text{AB}_x\text{C}_{1-x}$ ($A = \text{As, In}$; $x = 0 - 0.8$) exhibit no bulk superconductivity of the MAX phases. While Nb_2AsC shows a transition at 7.3 K with a volume fraction of $< 1\text{ vol.}\%$, the susceptibility of the corresponding solid solutions is independent of the temperature. Samples of $\text{Nb}_2\text{InB}_x\text{C}_{1-x}$ exhibit a decrease of volume susceptibility between 5 and 6 K with $< 2\text{ vol.}\%$. Therefore, all observed transitions for $\text{Nb}_2\text{AB}_x\text{C}_{1-x}$ ($A = \text{As, In}$) can be explained by the impurity phase NbC with $T_c = 3.5 - 11.5\text{ K}$, where the critical temperature depends on the carbon content and the synthesis method.^[111-114] Since Nb_2AsC ($T_c = 2\text{ K}$) and Nb_2InC ($T_c = 7.5\text{ K}$) are described as superconductors in the literature, the occurrence of this phenomenon in MAX phases might depend on the synthesis method as well.

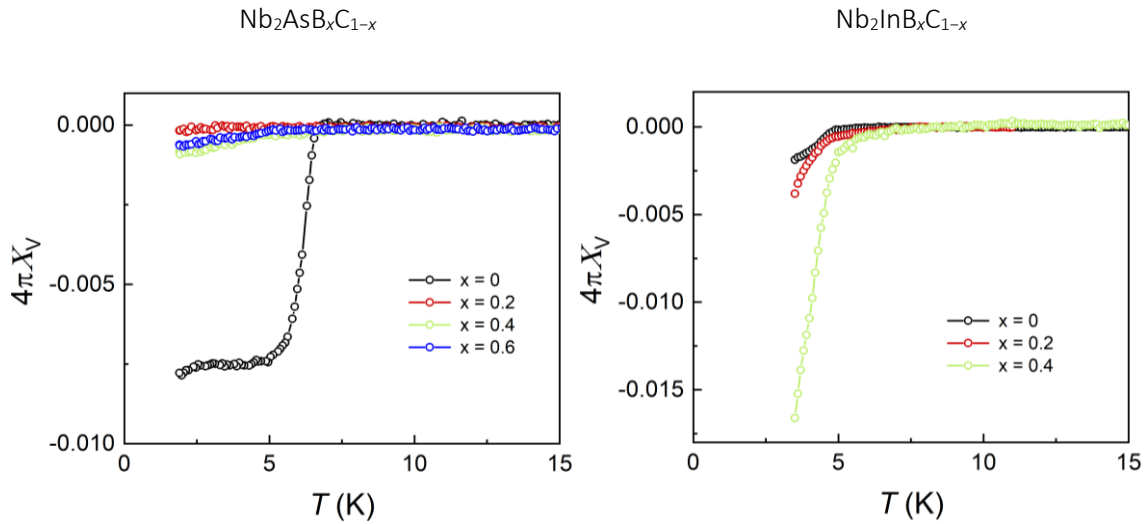


Figure 2-18: Susceptibility measurements of $\text{Nb}_2\text{AsB}_x\text{C}_{1-x}$ ($x = 0 - 0.6$) performed at a PPMS using the VSM option at 15 Oe (left) and of $\text{Nb}_2\text{InB}_x\text{C}_{1-x}$ ($x = 0 - 0.4$) performed at an AC susceptometer at 3 Oe (right).

Conclusion

$\text{Nb}_2\text{As(B,C)}$ were successfully synthesized via solid-state reaction and $\text{Nb}_2\text{A(B,C)}$ ($\text{A} = \text{Sn, In}$) using the flux method. For the latter, we were able to shorten the reaction time by adding an excess of tin or indium.

The crystal structures were determined by means of PXRD. All solid solutions crystallize in the Cr_2AlC -type ($P6_3/mmc$). $\text{Nb}_2\text{As(B,C)}$ show the same trends for the lattice parameters and the M_6X octahedron distortion as $M_2S(B,C)$ ($M = \text{Zr, Hf, Nb}$). $\text{Nb}_2\text{Sn(B,C)}$ exhibit smaller changes of the crystal structure, but is still consistent with previous results. Furthermore, the tin phases show a distinct saturation at a stoichiometry of $\text{Nb}_2\text{SnB}_{0.8}\text{C}_{0.2}$. For $\text{Nb}_2\text{In(B,C)}$, the unit cell does not change with increasing boron content. Nevertheless, the high phase fractions of the MAX phases determined from Rietveld refinement together with product yields of 70 – 80 % required an incorporation of boron. The boundary phases Nb_2AB ($\text{A} = \text{As, Sn, In}$) were not obtained. We were not able to determine the degree of substitution x in $\text{Nb}_2\text{AB}_x\text{C}_{1-x}$ ($\text{A} = \text{As, Sn, In}$; $x = 0 - 0.8$).

Magnetic measurements reveal that all synthesized compounds, including the boundary phases Nb_2AC ($\text{A} = \text{As, Sn, In}$), are not superconducting above 1.9 K. In the temperature range 1.9 – 300 K, the MAX phase borides show Pauli-paramagnetism. Further, the passivation of $\text{Nb}_2\text{SnB}_x\text{C}_{1-x}$ by a thin layer of Nb_3Sn was shown. This protective layer makes these MAX Phases remarkably inert to strong acids and provides a superconductive surface ($T_c = 18\text{K}$).

References

- [1] H. Nowotny, *Prog. Solid State Chem.* **1971**, *5*, 27-70.
- [2] P. Eklund, M. Beckers, U. Jansson, H. Högberg, L. Hultman, *Thin Solid Films* **2010**, *518*, 1851-1878.
- [3] T. Cabioch, P. Eklund, V. Mauchamp, M. Jaouen, M. W. Barsoum, *J. Eur. Ceram. Soc.* **2013**, *33*, 897-904.
- [4] M. Radovic, M. W. Barsoum, *Am. Ceram. Soc. Bull.* **2013**, *92*, 20-27.
- [5] A. S. Ingason, M. Dahlgvist, J. Rosen, *J. Phys.: Condens. Matter* **2016**, *28*, 433003.
- [6] J. C. Schuster, H. Nowotny, C. Vaccaro, *J. Solid State Chem.* **1980**, *32*, 213-219.
- [7] M. W. Barsoum, I. Salama, T. El-Raghy, J. Golczewski, H. J. Seifert, F. Aldinger, W. D. Porter, H. Wang, *Metall. Mater. Trans. A* **2002**, *33*, 2775-2779.
- [8] I. Salama, T. El-Raghy, M. W. Barsoum, *J. Alloys Compd.* **2002**, *347*, 271-278.
- [9] S. Gupta, M. W. Barsoum *J. Electrochem. Soc.* **2004**, *151*, D24-D29.
- [10] M. Radovic, M. W. Barsoum, A. Ganguly, T. Zhen, P. Finkel, S. R. Kalidindi, E. Lara-Curzio, *Acta Mater.* **2006**, *54*, 2757-2767.
- [11] H. Yang, B. Manoun, R. T. Downs, A. Ganguly, M. W. Barsoum, *J. Phys. Chem. Solids* **2006**, *67*, 2512-2516.
- [12] B. Manoun, S. K. Saxena, G. Hug, A. Ganguly, E. N. Hoffman, M. W. Barsoum, *J. Appl. Phys.* **2007**, *101*, 113523.
- [13] M. A. Pietzka, J. C. Schuster, *J. Am. Ceram. Soc.* **1996**, *79*, 2321-2330.
- [14] M. W. Barsoum, T. El-Raghy, M. Ali, *Metall. Mater. Trans. A* **2000**, *31*, 1857-1865.
- [15] O. Wilhelmsson, J. P. Palmquist, E. Lewin, J. Emmerlich, P. Eklund, P. O. Å. Persson, H. Högberg, S. Li, R. Ahuja, O. Eriksson, L. Hultman, U. Jansson, *J. Cryst. Growth* **2006**, *291*, 290-300.
- [16] J. Rosen, P. O. Å. Persson, M. Ionescu, A. Kondyurin, D. R. McKenzie, M. M. M. Bilek, *Appl. Phys. Lett.* **2008**, *92*, 064102.
- [17] K. Mohammad, A. Masao, S. Taizo, E. Mehdi, S. Yoshio, *J. Phys.: Condens. Matter* **2014**, *26*, 505503.
- [18] A. Gencer, G. Surucu, *Mater. Res. Express* **2018**, *5*, 076303.
- [19] G. Surucu, *Mater. Chem. Phys.* **2018**, *203*, 106-117.
- [20] P. Chakraborty, A. Chakrabarty, A. Dutta, T. Saha-Dasgupta, *Phys. Rev. Mater.* **2018**, *2*, 103605.

- [21] M. Ade, H. Hillebrecht, *Inorg. Chem.* **2015**, *54*, 6122-6135.
- [22] Y. Bai, X. Qi, A. Duff, N. Li, F. Kong, X. He, R. Wang, W. E. Lee, *Acta Mater.* **2017**, *132*, 69-81.
- [23] Z. Guo, J. Zhou, Z. Sun, *J. Mater. Chem. A* **2017**, *5*, 23530-23535.
- [24] S. Kota, M. Agne, E. Zapata-Solvas, O. Dezellus, D. Lopez, B. Gardiola, M. Radovic, M. W. Barsoum, *Phys. Rev. B: Condens. Matter* **2017**, *95*, 144108.
- [25] J. Lu, S. Kota, M. W. Barsoum, L. Hultman, *Mater. Res. Lett.* **2017**, *5*, 235-241.
- [26] Y. Zhou, H. Xiang, F.-Z. Dai, Z. Feng, *Mater. Res. Lett.* **2017**, *5*, 440-448.
- [27] S. Hirt, F. Hilfinger, H. Hillebrecht, *Z. Kristallogr. - Cryst. Mater.* **2018**, *233*, 295.
- [28] S. Kota, Y. Chen, J. Wang, S. J. May, M. Radovic, M. W. Barsoum, *J. Eur. Ceram. Soc.* **2018**, *38*, 5333-5340.
- [29] L. Verger, S. Kota, H. Roussel, T. Ouisse, M. W. Barsoum, *J. Appl. Phys.* **2018**, *124*, 205108.
- [30] Y. Bai, D. Sun, N. Li, F. Kong, X. Qi, X. He, R. Wang, Y. Zheng, *Int. J. Refract. Met. Hard Mater.* **2019**, *80*, 151-160.
- [31] H. Zhang, F.-z. Dai, H. Xiang, Z. Zhang, Y. Zhou, *J. Mater. Sci. Technol.* **2019**, *35*, 530-534.
- [32] R. Kessling, *Acta Chem. Scand.* **1949**, *3*, 90.
- [33] J. T. Norton, H. Blumenthal, S. J. Sindeband, *Trans. Am. Inst. Min., Metall. Pet. Eng.* **1949**, *1*, 749-751.
- [34] H. Nowotny, F. Benesovsky, R. Kieffer, *Z. Metallkd.* **1959**, *50*, 417-423.
- [35] S. Okada, T. Atoda, I. Higashi, Y. Takahashi, *J. Less-Common Met.* **1985**, *113*, 331-339.
- [36] A. Coelho, *TOPAS-Academic, Coelho Software* **2007**, *Version 4.1*.
- [37] L. J. v. d. Pauw, *Philips Tech. Rev.* **1958**, *20*, 220-224.
- [38] G. Kresse, J. Furthmüller, *Comput. Mater. Sci.* **1996**, *6*, 15-50.
- [39] G. Kresse, D. Joubert, *Phys. Rev. B: Condens. Matter* **1999**, *59*, 1758-1775.
- [40] P. E. Blöchl, *Phys. Rev. B: Condens. Matter* **1994**, *50*, 17953-17979.
- [41] J. P. Perdew, K. Burke, M. Ernzerhof, *Phys. Rev. Lett.* **1996**, *77*, 3865-3868.
- [42] S. Maintz, V. L. Deringer, A. L. Tchougréeff, R. Dronskowski, *J. Comput. Chem.* **2013**, *34*, 2557-2567.
- [43] J. Brgoch, S. P. DenBaars, R. Seshadri, *J. Phys. Chem. C* **2013**, *117*, 17955-17959.
- [44] V. L. Deringer, R. P. Stoffel, A. Togo, B. Eck, M. Meven, R. Dronskowski, *CrystEngComm* **2014**, *16*, 10907-10915.

-
- [45] A. Togo, I. Tanaka, *Scripta Mater.* **2015**, *108*, 1-5.
- [46] K. Sakamaki, H. Wada, H. Nozaki, Y. Ōnuki, M. Kawai, *Solid State Commun.* **1999**, *112*, 323-327.
- [47] G. Hug, M. Jaouen, M. W. Barsoum, *Phys. Rev. B: Condens. Matter* **2005**, *71*, 024105.
- [48] T. H. Scabarozi, S. Amini, P. Finkel, O. D. Leaffer, J. E. Spanier, M. W. Barsoum, M. Drulis, H. Drulis, W. M. Tambussi, J. D. Hettinger, S. E. Lofland, *J. Appl. Phys.* **2008**, *104*, 033502.
- [49] P. Eklund, J. Rosen, P. O. A. Persson, *J. Phys. D: Appl. Phys.* **2017**, *50*, 113001.
- [50] B. Anasori, M. Dahlgqvist, J. Halim, E. J. Moon, J. Lu, B. C. Hosler, E. a. N. Caspi, S. J. May, L. Hultman, P. Eklund, J. Rosén, M. W. Barsoum, *J. Appl. Phys.* **2015**, *118*, 094304.
- [51] I. R. Shein, A. L. Ivanovskii, *Phys. Status Solidi B* **2011**, *248*, 228-232.
- [52] M. T. Nasir, A. K. M. A. Islam, *Comput. Mater. Sci.* **2012**, *65*, 365-371.
- [53] W. L. McMillan, *Phys. Rev.* **1968**, *167*, 331-344.
- [54] F. Giustino, *Rev. Mod. Phys.* **2017**, *89*, 015003.
- [55] K. Sakamaki, H. Wada, H. Nozaki, Y. Onuki, M. Kawai, *Mol. Cryst. Liq. Cryst. Sci. Technol. Sect. A* **2000**, *341*, 99-104.
- [56] M. W. Barsoum, *Prog. Solid State Chem.* **2000**, *28*, 201-281.
- [57] X. H. Wang, Y. C. Zhou, *J. Mater. Sci. Technol.* **2010**, *26*, 385-416.
- [58] M. W. Barsoum, M. Radovic, *Ann. Rev. Mater. Res.* **2011**, *41*, 195-227.
- [59] J. Gruber, A. C. Lang, J. Griggs, M. L. Taheri, G. J. Tucker, M. W. Barsoum, *Sci. Rep. - UK* **2016**, *6*, 33451.
- [60] J. Griggs, A. C. Lang, J. Gruber, G. J. Tucker, M. L. Taheri, M. W. Barsoum, *Acta Mater.* **2017**, *131*, 141-155.
- [61] M. W. Barsoum, X. Zhao, S. Shanazarov, A. Romanchuk, S. Koumlis, S. J. Pagano, L. Lamberson, G. J. Tucker, *Phys. Rev. Mater.* **2019**, *3*, 013602.
- [62] M. Sokol, V. Natu, S. Kota, M. W. Barsoum, *Trends Chem.* **2019**, *1*, 210-223.
- [63] S. Kota, M. Sokol, M. W. Barsoum, *Int. Mater. Rev.* **2019**, 1-30.
- [64] T. Rackl, L. Eisenburger, R. Niklaus, D. Johrendt, *Phys. Rev. Mater.* **2019**, *3*, 054001.
- [65] R. Dronskowski, P. E. Bloechl, *The Journal of Physical Chemistry* **1993**, *97*, 8617-8624.
- [66] R. F. W. Bader, *Atoms in Molecules - A quantum theory*, Oxford University Press, London, **1990**.
- [67] G. Henkelman, A. Arnaldsson, H. Jónsson, *Comput. Mater. Sci.* **2006**, *36*, 354-360.

- [68] L. Fast, J. M. Wills, B. Johansson, O. Eriksson, *Phys. Rev. B: Condens. Matter* **1995**, *51*, 17431-17438.
- [69] W. Voigt, *Lehrbuch der Kristallphysik, Vol. 962*, Teubner Leipzig, **1928**.
- [70] A. Reuss, *ZAMM - Z. Angew. Math. Me.* **1929**, *9*, 49-58.
- [71] R. Hill, *P. Phys. Soc. A* **1952**, *65*, 349-354.
- [72] O. L. Anderson, *J. Phys. Chem. Solids* **1963**, *24*, 909-917.
- [73] H. Rohde, H. Kudielka, in *Z. Kristallogr. - Cryst. Mater., Vol. 114*, **1960**, p. 447.
- [74] S. R. Kulkarni, N. A. Phatak, S. K. Saxena, Y. Fei, J. Hu, *J. Phys.: Condens. Matter* **2008**, *20*, 135211.
- [75] A. Bouhemadou, R. Khenata, *Phys. Lett. A* **2008**, *372*, 6448-6452.
- [76] M. W. Barsoum, T. El-Raghy, *J. Am. Ceram. Soc.* **1996**, *79*, 1953-1956.
- [77] P. Eklund, M. Beckers, U. Jansson, H. Högberg, L. Hultman, *Thin Solid Films* **2010**, *518*, 1851-1878.
- [78] J. F. Nye, *Physical properties of crystals: their representation by tensors and matrices*, Oxford university press, **1985**.
- [79] J. Y. Wang, Y. C. Zhou, *J. Phys.: Condens. Matter* **2004**, *16*, 2819-2827.
- [80] M. Mattesini, M. Magnuson, F. Tasnádi, C. Höglund, I. A. Abrikosov, L. Hultman, *Phys. Rev. B: Condens. Matter* **2009**, *79*, 125122.
- [81] Z. J. Yang, L. Tang, A. M. Guo, X. L. Cheng, Z. H. Zhu, X. D. Yang, *J. Appl. Phys.* **2013**, *114*, 083506.
- [82] M. Foata-Prestavoine, G. Robert, M.-H. Nadal, S. Bernard, *Phys. Rev. B: Condens. Matter* **2007**, *76*, 104104.
- [83] J Haines, a. JM Léger, G. Bocquillon, *Ann. Rev. Mater. Res.* **2001**, *31*, 1-23.
- [84] V. V. Brazhkin, A. G. Lyapin, R. J. Hemley, *Philos. Mag. A* **2002**, *82*, 231-253.
- [85] J. Wang, Y. Zhou, T. Liao, Z. Lin, *Appl. Phys. Lett.* **2006**, *89*, 021917.
- [86] S. Kuchida, T. Muranaka, K. Kawashima, K. Inoue, M. Yoshikawa, J. Akimitsu, *Phys. C* **2013**, *494*, 77-79.
- [87] D. T. Cuskelly, E. R. Richards, E. H. Kisi, V. J. Keast, *J. Solid State Chem.* **2015**, *230*, 418-425.
- [88] H. Fashandi, M. Dahlqvist, J. Lu, J. Palisaitis, S. I. Simak, I. A. Abrikosov, J. Rosen, L. Hultman, M. Andersson, A. Lloyd Spetz, P. Eklund, *Nat. Mater.* **2017**, *16*, 814-818.
- [89] C.-C. Lai, H. Fashandi, J. Lu, J. Palisaitis, P. O. Å. Persson, L. Hultman, P. Eklund, J. Rosen, *Nanoscale* **2017**, *9*, 17681-17687.

-
- [90] T. Lapauw, B. Tunca, T. Cabioc'h, J. Vleugels, K. Lambrinou, *J. Eur. Ceram. Soc.* **2017**, *37*, 4539-4545.
- [91] M. Li, J. Lu, K. Luo, Y. Li, K. Chang, K. Chen, J. Zhou, J. Rosen, L. Hultman, P. Eklund, P. O. Å. Persson, S. Du, Z. Chai, Z. Huang, Q. Huang, *J. Am. Chem. Soc.* **2019**, *141*, 4730-4737.
- [92] D. Horlait, S. Grasso, A. Chroneos, W. E. Lee, *Mater. Res. Lett.* **2016**, *4*, 137-144.
- [93] J. Yang, M. Naguib, M. Ghidui, L.-M. Pan, J. Gu, J. Nanda, J. Halim, Y. Gogotsi, M. W. Barsoum, *J. Am. Ceram. Soc.* **2016**, *99*, 660-666.
- [94] C. M. Hamm, J. D. Bocarsly, G. Seward, U. I. Kramm, C. S. Birkel, *J. Mater. Chem. C* **2017**, *5*, 5700-5708.
- [95] C.-C. Lai, A. Petruhins, J. Lu, M. Farle, L. Hultman, P. Eklund, J. Rosen, *Mater. Res. Lett.* **2017**, *5*, 533-539.
- [96] E. Zapata-Solvas, S.-R. G. Christopoulos, N. Ni, D. C. Parfitt, D. Horlait, M. E. Fitzpatrick, A. Chroneos, W. E. Lee, *J. Am. Ceram. Soc.* **2017**, *100*, 1377-1387.
- [97] E. Zapata-Solvas, M. A. Hadi, D. Horlait, D. C. Parfitt, A. Thibaud, A. Chroneos, W. E. Lee, *J. Am. Ceram. Soc.* **2017**, *100*, 3393-3401.
- [98] C.-C. Lai, Q. Tao, H. Fashandi, U. Wiedwald, R. Salikhov, M. Farle, A. Petruhins, J. Lu, L. Hultman, P. Eklund, J. Rosen, *APL Mater.* **2018**, *6*, 026104.
- [99] G. W. Bentzel, M. Sokol, J. Griggs, A. C. Lang, M. W. Barsoum, *J. Alloys Compd.* **2019**, *771*, 1103-1110.
- [100] T. Scabarozzi, A. Ganguly, J. D. Hettinger, S. E. Lofland, S. Amini, P. Finkel, T. El-Raghy, M. W. Barsoum, *J. Appl. Phys.* **2008**, *104*, 073713.
- [101] T. Cabioc'h, P. Eklund, V. Mauchamp, M. Jaouen, *J. Eur. Ceram. Soc.* **2012**, *32*, 1803-1811.
- [102] Y. Zhou, H. Xiang, F.-Z. Dai, Z. Feng, *J. Mater. Sci. Technol.* **2018**, *34*, 1441-1448.
- [103] A. D. Bortolozzo, O. H. Sant'Anna, C. A. M. dos Santos, A. J. S. Machado, *Solid State Commun.* **2007**, *144*, 419-421.
- [104] A. D. Bortolozzo, Z. Fisk, O. H. Sant'Anna, C. A. M. d. Santos, A. J. S. Machado, *Phys. C* **2009**, *469*, 256-258.
- [105] A. D. Bortolozzo, G. Serrano, A. Serquis, D. Rodrigues, C. A. M. dos Santos, Z. Fisk, A. J. S. Machado, *Solid State Commun.* **2010**, *150*, 1364-1366.
- [106] A. D. Bortolozzo, O. H. Sant'Anna, M. S. da Luz, C. A. M. dos Santos, A. S. Pereira, K. S. Trentin, A. J. S. Machado, *Solid State Commun.* **2006**, *139*, 57-59.
- [107] S. E. Lofland, J. D. Hettinger, T. Meehan, A. Bryan, P. Finkel, S. Gupta, M. W. Barsoum, G. Hug, *Phys. Rev. B: Condens. Matter* **2006**, *74*, 174501.
- [108] A. Coelho, in *TOPAS-Academic, Vol. Version 4.1*, Version 4.1 ed., Coelho Software, Brisbane, **2007**.

- [109] O. Beckmann, H. Boller, H. Nowotny, *Monatsh. Chem.* **1968**, *99*, 1580-1583.
- [110] R. S. Kumar, S. Rekhi, A. L. Cornelius, M. W. Barsoum, *Appl. Phys. Lett.* **2005**, *86*, 111904.
- [111] F. J. Darnell, P. E. Bierstedt, W. O. Forshey, R. K. Waring, *Phys. Rev.* **1965**, *140*, A1581-A1585.
- [112] B. W. Roberts, *J. Phys. Chem. Ref. Data* **1976**, *5*, 581-822.
- [113] A. I. Gusev, A. A. Rempel, *Phys. Status Solidi B* **1989**, *151*, 211-224.
- [114] R. Jha, V. P. S. Awana, *J. Supercond. Nov. Magn.* **2012**, *25*, 1421-1425.

3 M and A site substitutions in MAX phases

Abstract

The solid solutions $M_2A_xA'_{1-x}C$ ($M = V, Nb$; $A, A' = In, Ge, Sn, P, As, S$) and $(V_xNb_{1-x})_2SC$ were synthesized via solid-state reaction of the elements at high temperatures (1100 – 1280 °C). The crystal structures were determined by powder X-ray diffraction and Rietveld refinement. All solid solutions crystallize in the hexagonal Cr_2AlC -type. The structural changes within each quaternary system are linear with the degree of substitution. EDX measurements verified the stoichiometries of the solid solutions. Magnetic measurements reveal that the superconductivity in $Nb_2As_xS_{1-x}C$ has a maximum critical temperature at $x = 0.2$ ($T_c = 5.2$ K). $Nb_2(In_xSn_{1-x})C$ and $Nb_2(Ge_xAs_{1-x})C$ do not exhibit superconductivity as expected from the properties of the boundary phases. The other examined solid solutions are Pauli paramagnets.

Introduction

The group of ternary MAX phases itself shows a great diversity, but what makes it even more diverse is the potential to form solid solutions. The variety of solid solutions is immense, as almost all elements known in these phases can be combined, and elements that do not form ternary MAX phases can also be incorporated. Table 3-1 shows an extract of known solid solutions in the 211-type. Here it is conspicuous that the group of compounds substituted on the M site is the largest, followed by those substituted on the A site and, beyond this thesis, only one substitution of the X site.^[1-3] A possible explanation for this is that only carbon and nitrogen were known at the X site so far. A stoichiometric weighing with nitrogen requires a nitrogen compound as precursor. However, since the transition metal nitrides are very stable, they are only suitable as educts in certain cases. Furthermore, substitution on the M site is more attractive than on the A site, since the A element is lost by exfoliation to MXenes. Thus, the properties cannot be transferred to MXenes, which have various potential applications such as energy storage, water purification, sensors, and many more.^[4-5]

The substitution is not only suitable for tuning of properties, but it can also result in stacking variations, like the 514-type in $(Ti_{0.5}Nb_{0.5})_5AlC_4$ and the 523-type in $(V_{0.5}Cr_{0.5})_5Al_2C_3$, which can only be obtained in solid solutions.^[6-7] Further, magnetic order can be induced in MAX phases by substitution with iron and manganese.^[8-11] This adds another property to this compound class, which mostly shows Pauli paramagnetism, and provides the possibility for magnetic MXenes.

Recently, however, compounds with *A* site substitution came into focus when it was discovered that gold, bismuth, and copper could be incorporated. This led for the first time to a symmetry reduction from $P6_3/mmc$ to $C2/c$ within the MAX phases.^[12-14]

Table 3-1: Excerpt of 211-type solid-solution MAX phases. If not stated otherwise the solid solutions are described with $x = 0 - 1$. Especially for *M* site solid solutions, many more compounds are known. Solid solutions that are part of this chapter are in blue and solid solutions part of previous chapters 2.1, and 2.3 in green.

<i>M</i> site	<i>A</i> site	<i>X</i> site
$(Ti_xZr_{1-x})_2InC$ ^[15]	$Zr_2(Al_xSn_{1-x})C$ ^[22, 29]	$Ti_2Al(C_xN_{1-x})_y$ ($y < 0.2$) ^[34-35]
$(Ti_xHf_{1-x})_2InC$ ^[16]	$Zr_2(Al_xPb_{1-x})C$ ($x = 0.65$) ^[29]	$Nb_2In(B_xC_{1-x})$ ($x < 0.8$)*
$(Ti_xV_{1-x})_2AlC$ ^[17]	$Zr_2(Al_xBi_{1-x})C$ ($x = 0.58$) ^[13, 29]	$Nb_2Sn(B_xC_{1-x})$ ($x < 0.8$)*
$(Ti_xNb_{1-x})_2AlC$ ^[17]	$Zr_2(Al_xSb_{1-x})C$ ($x = 0.7$) ^[29]	$Nb_2As(B_xC_{1-x})$ ($x < 0.8$)*
$(Ti_xTa_{1-x})_2AlC$ ^[18]	$V_2(Al_xGa_{1-x})C$ ($0.43 < x < 0.6$) ^[30]	$Nb_2S(B_xC_{1-x})$ * ^[36]
$(Ti_xCr_{1-x})_2AlC$ ^[17, 19]	$Cr_2(Al_xSi_{1-x})C$ ($x = 0.03$) ^[31]	
$(Ti_xMo_{1-x})_2AlC$ ($x < 0.2$) ^[20]	$Cr_2(Al_xGe_{1-x})C$ ^[32]	
$(Zr_xNb_{1-x})_2AlC$ ^[21-22]	$Mo_2(Ga_{0.33}Fe_{0.5}Au_{0.16})C$ ^[33]	
$(V_xNb_{1-x})_2AlC$ ^[21, 23]	$V_2(Ge_xP_{1-x})C$ *	
$(V_xCr_{1-x})_2AlC$ ^[17, 24]	$V_2(Ge_xAs_{1-x})C$ *	
$(V_xCr_{1-x})_2GeC$ ($x = 0.5$) ^[25]	$V_2(P_xAs_{1-x})C$ *	
$(V_xMn_{1-x})_2AlC$ ($x = 0.04$) ^[26]	$V_2(P_xS_{1-x})C$ *	
$(Nb_xSc_{1-x})_2AlC$ ($x = 1/3$) ^[27]	$V_2(As_xS_{1-x})C$ *	
$(Cr_xMn_{1-x})_2AuC$ ($x = 0.5$) ^[28]	$Nb_2(In_xSn_{1-x})C$ *	
$(Cr_xMn_{1-x})_2AlC$ ($x < 0.1$) ^[10-11]	$Nb_2(Ge_xAs_{1-x})C$ *	
$(Cr_xMn_{1-x})_2GaC$ ($x = 0.5$) ^[12]	$Nb_2(P_xAs_{1-x})C$ *	
$(Cr_xMn_{1-x})_2GeC$ ^[8-9]	$Nb_2(As_xS_{1-x})C$ *	
$(Cr_xFe_{1-x})_2AlC$ ($x < 0.02$) ^[11]		
$(V_xNb_{1-x})_2SC$ *		

*described within this thesis

Recently it was stated by Lapauw et al., that the formation of a solid solution is likely when the distortion of the AM_6 prism reduces. The degree of distortion p_d is given by the quotient of d_{M-M}/d_{M-A} , with d_{M-M} being equal to the *a*-axis. The distortion minimizes when the *M* and the *A* element have similar radii. This theory can be used as a guideline for the synthesis of new solid solutions.^[22]

Herein, we present the synthesis of the solid solutions $M_2A_xA'_{1-x}C$ ($M = V, Nb$; $A, A' = In, Ge, Sn, P, As, S$) and $(V_xNb_{1-x})_2SC$, which are listed in Table 3-1. The substitution causes structural changes, which are linear with x and conclusive with trends of other known solid solutions. EDX measurements verified the stoichiometries of the MAX phases. Magnetic measurements reveal that $Nb_2As_xS_{1-x}C$ are superconductors for $x \geq 0.7$, while the other solid solutions are Pauli paramagnets.

Experimental

The solid solutions $M_2A_xA'_{1-x}C$ ($M = V, Nb$; $A, A' = In, Ge, Sn, P, As, S$) and $(V_xNb_{1-x})_2SC$ were synthesized via solid-state reactions from the elements (see Table A-5). Stoichiometric mixtures were homogenized, and some of the samples were pressed to pellets (2 t, 120 min) before they were filled in crucibles. The reaction took place either in a chamber furnace or in a tube furnace. For the first reaction step, slow heating rates from 100 to 200 °C/h were chosen. For following annealing steps, the heating rates were increased up to 600 °C/h. The MAX phases were synthesized at high temperatures between 1100 °C and 1280 °C. After dwell times between 30 and 354 h, depending on the compound and the reaction temperature, the mixtures were quenched either in water or in air. Table 3-2 shows detailed reaction conditions for each solid solution.

All samples were annealed several times (2 – 9 times) at high temperatures. The reaction progress and the phase proportions of the MAX phase were determined by Rietveld refinement of the PXRD data collected at a Huber G670 diffractometer with Cu-K α_1 radiation ($\lambda = 1.54059 \text{ \AA}$) using the TOPAS software package.^[37] EDX measurements were conducted on a Zeiss EVO-MA 10 REM using a Bruker X-Flash 410-M. Magnetic measurements were performed either on an AC susceptometer, a Quantum Design Squid MPMS XL-5, or a Quantum Design PPMS-9 using the VSM option.

Table 3-2: Reaction conditions for the synthesis of $M_2A_xA'_{1-x}C$ ($M = Nb, V$; $A, A' = In, Ge, Sn, P, As, S$) and $(V_xNb_{1-x})_2SC$.

compound	heating rate (°C/h)	reaction temp. (°C)	dwel time (h)	quenching	crucible
$V_2(Ge_xP_{1-x})C$	200 – 600	1100	62 – 113	in air or in water	alumina
$V_2(Ge_xAs_{1-x})C$	200 – 500	1100	37 – 83	in air or in water	alumina
$V_2(P_xAs_{1-x})C$	200 – 600	1100	38 – 122	in water	alumina
$V_2(P_xS_{1-x})C$	100 – 200	1100	30 – 90	in air or in water	alumina
$V_2(As_xS_{1-x})C$	200 – 500	1100	32 – 108	in air or in water	alumina
$Nb_2(In_xSn_{1-x})C$	120 – 500	1150	34 – 63	in water	niobium
$Nb_2(Ge_xAs_{1-x})C$	120 – 500	1100 – 1280	65 – 256	in water	alumina
$Nb_2(P_xAs_{1-x})C$	120 – 500	1100 – 1200	34 – 118	in water	alumina
$Nb_2(As_xS_{1-x})C$	100 – 600	1150	39 – 130	in air or in water	alumina
$(V_xNb_{1-x})_2SC$	120	1100 – 1200	66 – 354	in air or in water	silica

Results and discussion

Synthesis and crystal structure

The phase pure synthesis of MAX phases is often challenging. High temperatures (> 1000 °C) are necessary for the formation, but they also start to decompose if the temperature is too high. Therefore arc melting is not suitable for most of the compounds. When it comes to solid solutions, the synthesis becomes even more difficult since the reaction needs additional time to form a homogeneous sample. For $M_2A_xA'_{1-x}C$ ($M = V, Nb$; $A, A' = In, Ge, Sn, P, As, S$) and $(V_xNb_{1-x})_2SC$ the boundary phases V_2GeC , V_2PC , V_2AsC , Nb_2InC , Nb_2SnC , Nb_2PC , Nb_2AsC and Nb_2SC are known from the literature (see Table 3-3), while Nb_2GeC was synthesized via solid-state reaction at 1200 °C within this thesis and V_2SC was not obtained until now.^[38-40]

Table 3-3: Boundary MAX phases known from the literature, including synthesis temperatures T , critical temperatures of superconductors (T_c), and references.

compound	T (°C)	T_c	reference
V ₂ GeC	1200	-	[38]
V ₂ PC	1000	-	[41]
V ₂ AsC	1100	-	[42]
Nb ₂ InC	1200	$T_c = 7.5$ K	[38, 43]
Nb ₂ GeC	1200	$T_c = 10$ K	[39]
Nb ₂ SnC	1200	$T_c = 7.8$ K	[38]
Nb ₂ PC	1150	-	[40]
Nb ₂ AsC	1150	$T_c = 2$ K	[40, 44-45]
Nb ₂ SC _{0.9}	1150	$T_c = 5$ K	[46-48]

The known boundary MAX phases were synthesized to determine the best reaction conditions. Rietveld refinements show that they form via solid-state reaction at 1000 – 1200 °C as described in the literature (see Figure A-1 and Figure A-28 – A-35). The compounds can be prepared with high phase proportions (84 – 100 wt.%) except for Nb₂PC, where the formation of Nb₃P₂C is preferred at longer reaction times. For the synthesis of the solid solutions given in Table 3-2, similar reaction temperatures 1100 – 1280 °C were chosen. Nevertheless, the reaction conditions need to be optimized for each solid solution separately.

For the first reaction step, a lower heating rate was chosen to prevent the A element from evaporation or sublimation. We found that rapid cooling rates result in higher phase proportions of the MAX phases. Therefore, the samples were quenched in water or air. Especially for solid solutions, it is advantageous to press the sample into pellets, as this shortens the diffusion paths during the reaction and thus significantly reduces the phase width of the MAX phase. For most of the reactions, we chose alumina crucibles. The only disadvantage is that the gas phase is in contact with the silica surface. It is known from literature that oxygen is bound to this surface in the form of water or hydroxide groups. At temperatures > 1000 °C, these can be released, which leads to the formation of metal oxides in the sample at long reaction times.^[49-50] The samples were annealed 2 – 9 times to obtain the desired solid solutions. Even though the MAX phase already forms in the first step, the annealing steps were necessary to increase the phase proportion and to reduce the peak broadening. The products are black powders with phase proportions of 67 – 100 wt.%. The Rietveld refinements of the PXRD data of the synthesized solid solutions are displayed in Figure A-28 – A-78.

211-type MAX phases crystallize in the hexagonal Cr_2AlC -type, which is build up by layers of M_6X octahedra alternately stacked with layers of the *A* element. Thereby, three different bonds arise, which vary in strength depending on the combination of elements. First, there is a metallic interaction between the *M* elements. The ionic interaction between *M* and *X* is strong, while the *M*—*A* interaction is weaker, which gives the opportunity of exfoliation to MXenes. This property also leads to the fact that the *M* site and especially the *A* site can easily be substituted and thus holds a great potential for tuning the properties of the system.

In $M_2A_xA'_{1-x}C$ ($M = \text{V, Nb}$; $A, A' = \text{In, Ge, Sn, P, As, S}$) and $(\text{V}_x\text{Nb}_{1-x})_2\text{SC}$ the substitution was achieved by reaction of the corresponding stoichiometric mixture of the elements, but the value of x needs to be verified. For $\text{V}_2(\text{Ge}_x\text{P}_{1-x})\text{C}$, $\text{V}_2(\text{P}_x\text{As}_{1-x})\text{C}$, $\text{V}_2(\text{As}_x\text{S}_{1-x})\text{C}$, $\text{Nb}_2(\text{P}_x\text{As}_{1-x})\text{C}$, $\text{Nb}_2(\text{As}_x\text{S}_{1-x})\text{C}$, $(\text{V}_x\text{Nb}_{1-x})_2\text{SC}$ the mixed occupancy can be refined using the Rietveld method, since the elements show significant differences in the electron count. The determined ratios are in good agreement to the nominal stoichiometries (see Table 3-4). However, the refined values correlate with absorption parameters and the thermal displacements of the atom sites. Therefore, we assume an error of ± 0.1 for x . EDX measurements verified x for some samples (see Table 3-4). The measured values of x correspond to the targeted x .

Nevertheless, the values determined from EDX measurements have to be treated with care, since the crystallite sizes are very small ($< 2 \mu\text{m}$). Thus, it cannot be excluded that the electron beam has targeted more than one particle. This can lead to falsification of the measured data, especially in samples with significant proportions of impurity phases. The results from Rietveld refinement, together with those of the EDX measurements, show that all stoichiometries can be synthesized by reaction of stoichiometric mixtures.

Besides the electron density, the substituted elements also differ in the size of the ion radii. The unit cell volume increases, with the increasing amount of the larger ion in the solid solution. These changes show a linear trend with x . However, the signs of the trends of the *a*- and *c*-axis can be opposing. In these cases, the *c*-axis change is greater than the *a*-axis change and, therefore, is decisive for the volume change. The lattice parameters can be traced from Table A-6 – A-15.

In contrast, the *A* atoms in $\text{V}_2(\text{Ge}_x\text{As}_{1-x})\text{C}$, $\text{V}_2(\text{P}_x\text{S}_{1-x})\text{C}$, $\text{Nb}_2(\text{In}_x\text{Sn}_{1-x})\text{C}$, $\text{Nb}_2(\text{Ge}_x\text{As}_{1-x})\text{C}$ show hardly any difference in electron density or atomic radii. However, the change in the total number of electrons in the compound still results in a change in the unit cell, as for $\text{Zr}_2\text{S}(\text{B,C})$, $\text{Hf}_2\text{S}(\text{B,C})$ and $\text{Nb}_2A(\text{B,C})$ ($A = \text{In, Sn, As, S}$) (see chapter 2).

Table 3-4: Target x and x determined from PXRD (with an estimated error) and EDX data for the solid solutions $M_2A_xA'_{1-x}C$ ($M = V, Nb$; $A, A' = Ge, P, As, S$) and $(V_xNb_{1-x})_2SC$ with a significant difference in electron count of the elements.

compound	target x	x from PXRD	x from EDX
$V_2(Ge_xP_{1-x})C$	0.8	0.73(10)	0.84(4)
$V_2(Ge_xP_{1-x})C$	0.5	0.50(10)	0.48(3)
$V_2(Ge_xP_{1-x})C$	0.2	0.13(10)	0.11(2)
$V_2(P_xAs_{1-x})C$	0.8	0.72(10)	0.66(10)
$V_2(P_xAs_{1-x})C$	0.5	0.57(10)	-
$V_2(P_xAs_{1-x})C$	0.2	0.17(10)	0.24(13)
$V_2(As_xS_{1-x})C$	0.8	0.75(10)	-
$V_2(As_xS_{1-x})C$	0.5	0.60(10)	0.56(3)
$Nb_2(P_xAs_{1-x})C$	0.8	0.70(10)	-
$Nb_2(P_xAs_{1-x})C$	0.5	0.38(10)	-
$Nb_2(P_xAs_{1-x})C$	0.2	0.19(10)	-
$Nb_2(As_xS_{1-x})C$	0.9	0.93(10)	0.89(3)
$Nb_2(As_xS_{1-x})C$	0.8	0.81(10)	0.82(5)
$Nb_2(As_xS_{1-x})C$	0.7	0.73(10)	-
$Nb_2(As_xS_{1-x})C$	0.6	0.62(10)	0.65(1)
$Nb_2(As_xS_{1-x})C$	0.5	0.57(10)	0.47(4)
$Nb_2(As_xS_{1-x})C$	0.4	0.44(10)	0.38(3)
$Nb_2(As_xS_{1-x})C$	0.3	0.34(10)	0.27(2)
$Nb_2(As_xS_{1-x})C$	0.2	0.26(10)	-
$Nb_2(As_xS_{1-x})C$	0.1	0.13(10)	0.13(6)
$(V_xNb_{1-x})_2SC$	0.05	0.03(10)	0.03(1)
$(V_xNb_{1-x})_2SC$	0.1	0.11(10)	0.12(2)
$(V_xNb_{1-x})_2SC$	0.15	0.15(10)	-
$(V_xNb_{1-x})_2SC$	0.2	0.18(10)	-
$(V_xNb_{1-x})_2SC$	0.25	0.23(10)	0.23(5)
$(V_xNb_{1-x})_2SC$	0.3	0.30(10)	-
$(V_xNb_{1-x})_2SC$	0.35	0.34(10)	0.35(5)
$(V_xNb_{1-x})_2SC$	0.4	0.40(10)	0.41(5)
$(V_xNb_{1-x})_2SC$	0.45	0.44(10)	0.47(4)
$(V_xNb_{1-x})_2SC$	0.5	0.48(10)	0.51(7)

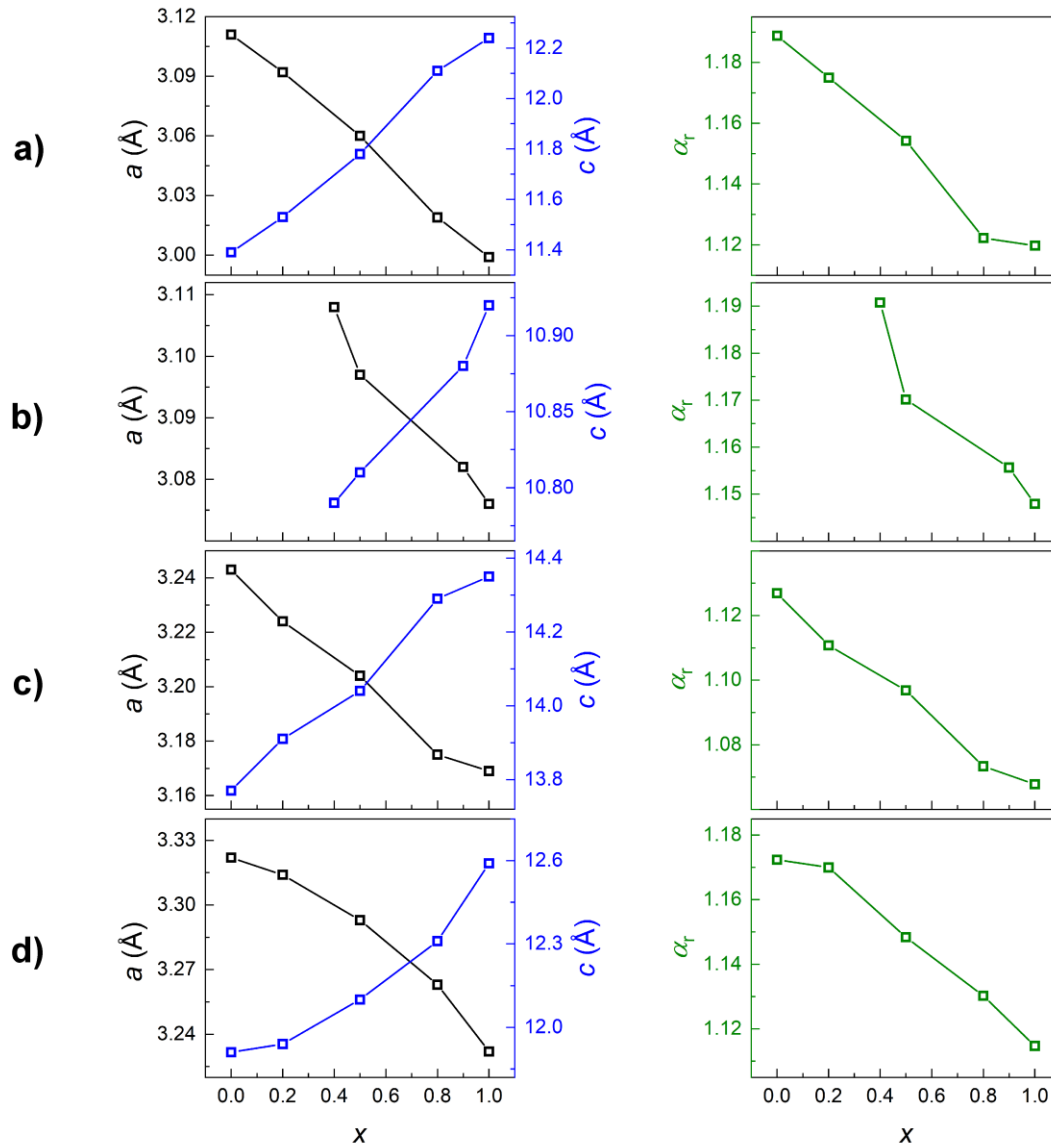


Figure 3-1: Change of the lattice parameters (a - and c -axis) and the distortion of the M_6X octahedra (α_r value) in a) $V_2(Ge_xAs_{1-x})C$, b) $V_2(P_xS_{1-x})C$, c) $Nb_2(In_xSn_{1-x})C$ and d) $Nb_2(Ge_xAs_{1-x})C$. The error bars are smaller than the spot sizes.

While the c -axis lengthens, the a -axis shortens with decreasing total electron number for the solid solutions $V_2(Ge_xAs_{1-x})C$, $V_2(P_xS_{1-x})C$, $Nb_2(In_xSn_{1-x})C$ and $Nb_2(Ge_xAs_{1-x})C$ (see Figure 3-1). This results in almost unchanged unit cell volumes. The thereby changed c/a ratio is decisive for the change of the M_6X polyhedron rather than the change of the coordinate of the metal atom \tilde{z}_M (see equation 2-1). The octahedron is less distorted for a higher total electron count, and the distortion shows a linear trend with x .

These changes clearly show the successful substitution, but the stoichiometry cannot be determined with certainty. For this purpose, EDX spectra were taken of all samples. The results confirm the successful substitution in all phases (see Table 3-5). They show that the desired compositions were achieved for all solid solutions in the range of the standard deviation.

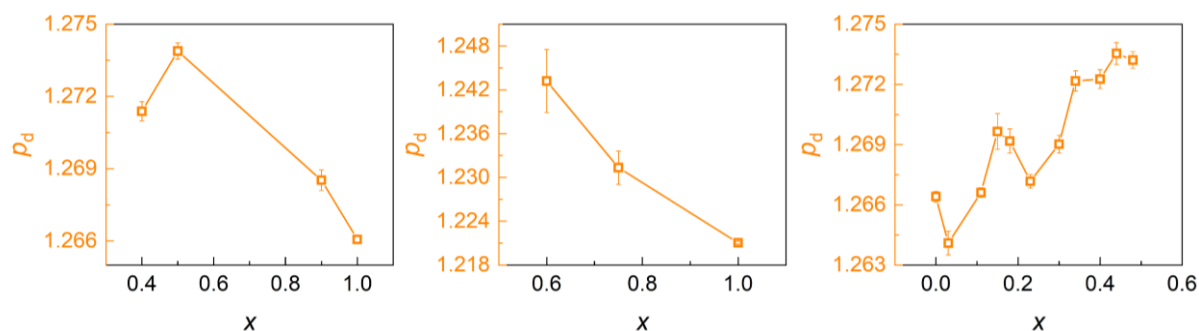


Figure 3-2: Distortion of the M_6A trigonal prism p_d in the solid solutions $V_2(P_xS_{1-x})C$ (left), $V_2(As_xS_{1-x})C$ (middle), and $(V_xNb_{1-x})_2SC$ (right). If the error bars are not shown, they are smaller than the spot sizes.

For the solid solutions $V_2(Ge_xP_{1-x})C$, $V_2(Ge_xAs_{1-x})C$, $V_2(P_xAs_{1-x})C$, $Nb_2(In_xSn_{1-x})C$, $Nb_2(Ge_xAs_{1-x})C$, $Nb_2(P_xAs_{1-x})C$ and $Nb_2(As_xS_{1-x})C$ both boundary phases are known. For these, the degree of substitution can be easily adjusted by the reaction of stoichiometric mixtures of the elements, as described above. However, several reaction steps are necessary to minimize the phase widths. Lapauw *et al.* proposed the theory that a solid solution can be synthesized, if the distortion of the trigonal prism M_6A reduces.^[22] However, this theory can only be applied if one boundary phase is not known, since the existence of both boundary phases indicate the stability of phases with both distortions. This is given for $V_2(P_xS_{1-x})C$, $V_2(As_xS_{1-x})C$, and $(V_xNb_{1-x})_2SC$, since V_2SC has not yet been synthesized. On the one hand, niobium in Nb_2SC can be substituted by vanadium up to $x_{max} = 0.5$. On the other hand, a substitution on the A site by sulfur is possible, as in $V_2(P_xS_{1-x})C$ ($x_{max} = 0.4$) and $V_2(As_xS_{1-x})C$ ($x_{max} = 0.5$).

In this case, the substitution leads to a stronger distortion of the trigonal prism p_d and not vice versa. These trends are shown in Figure 3-2, with the ideal value for p_d being 1 in a regular trigonal prism. However, the change of the polyhedron distortion is rather small. The limited solubility in these solid solutions suggests that the formation of the compound becomes unfavorable. We assume that a substitution is possible until the strain caused by the distortion becomes too large. Therefore, our results amplify the theory of Lapauw *et al.* and prove the dependence of the distortion of the trigonal prism on the stability of the MAX phase.

Table 3-5: Target x and x from EDX data for the solid solutions $M_2A_xA'_{1-x}C$ ($M = V, Nb$; $A, A' = Ge, In, Sn, P, As, S$).

compound	target x	x from EDX
$V_2(Ge_xAs_{1-x})C$	0.8	0.76(5)
$V_2(Ge_xAs_{1-x})C$	0.5	0.47(5)
$V_2(Ge_xAs_{1-x})C$	0.2	0.19(1)
$V_2(P_xS_{1-x})C$	0.9	0.88(5)
$V_2(P_xS_{1-x})C$	0.5	0.56(2)
$V_2(P_xS_{1-x})C$	0.4	0.41(4)
$Nb_2(In_xSn_{1-x})C$	0.8	0.81(1)
$Nb_2(In_xSn_{1-x})C$	0.5	0.45(6)
$Nb_2(In_xSn_{1-x})C$	0.2	0.24(2)
$Nb_2(Ge_xAs_{1-x})C$	0.8	0.75(5)
$Nb_2(Ge_xAs_{1-x})C$	0.5	0.46(8)
$Nb_2(Ge_xAs_{1-x})C$	0.2	0.19(8)

Magnetic properties

Besides the structural changes, substitutions in the MAX phases can affect the magnetic properties, as shown in chapter 2.1. Due to their good electrical conductivity, most of them exhibit Pauli paramagnetism, while some of them are low-temperature superconductors (see Table 3-3).^[51] For Nb_2SC_y , the critical temperature depends on y , with the maximum at $y = 0.9$ ($T_c = 5$ K), as already verified in chapter 2.1.^[48, 52] This is different for Nb_2AsC . In the literature, the compound is described with a T_c of 2 K, but the resistivity does not drop to zero, and the anomaly in the heat capacity is not very pronounced.^[45] Figure 3-3 shows the susceptibilities of the solid solutions $Nb_2(As_xS_{1-x})C$. Our measurements confirm that Nb_2SC_y is a superconductor with $T_c = 3.6$ K even though the critical temperature is lower than reported. This could be explained by an occupation of the C site deviating from the ideal value $y = 0.9$. Nb_2AsC , on the other hand, shows no superconductivity above 1.9 K. The solid solutions $Nb_2(As_xS_{1-x})C$ are superconducting up to $x = 0.7$ with the maximum T_c being 5.2 K occurring at $x = 0.2$, $Nb_2As_{0.2}S_{0.8}C$ (see Figure 3-3). The differences in the superconducting volume fraction show no trend with x and are therefore due to other effects such as a preferred orientation of the crystallites, shielding of particles or the inaccurate determination of the volume of the sample.

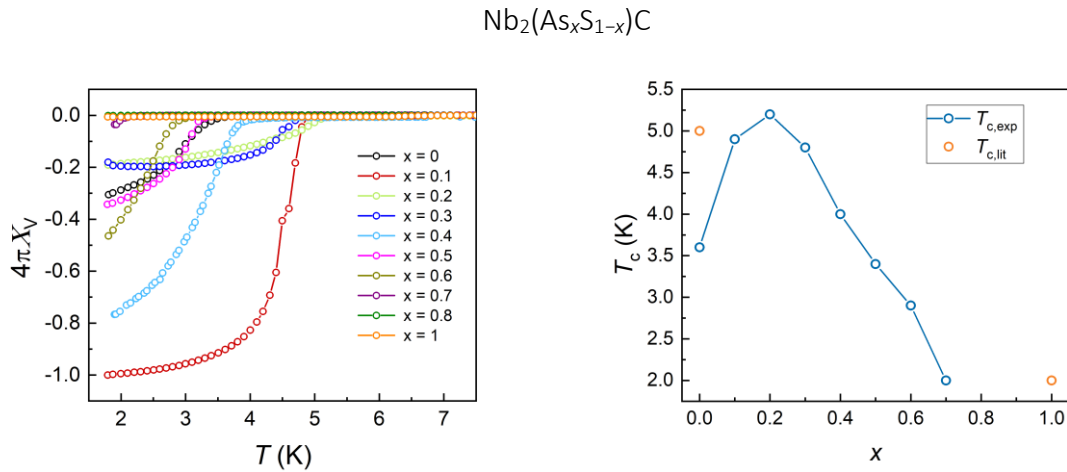


Figure 3-3: Magnetic susceptibility measurements of the solid solutions $\text{Nb}_2(\text{As}_x\text{S}_{1-x})\text{C}$ in the temperature range 1.9 – 8.0 K at 15 Oe (left). Critical temperatures $T_{c,exp}$ of the solid solutions $\text{Nb}_2(\text{As}_x\text{S}_{1-x})\text{C}$ and critical temperatures from the literature $T_{c,lit}$ for Nb_2AsC and Nb_2SC (right).

Furthermore, the superconducting MAX phases Nb_2GeC ($T_c = 10$ K), Nb_2InC ($T_c = 7.5$ K), and Nb_2SnC ($T_c = 7.8$ K) are known.^[39, 53-54] Contrary to these results, our measurements show no superconductivity of these MAX phases. Nb_2SnC has no transition above 3.5 K. In the case of Nb_2InC , the susceptibility decreases at 6.9 K. The volume susceptibility only drops about 7 vol.% and is, therefore, more likely due to the NbC ($T_c = 3.2 - 11.5$ K) impurity.^[39, 55-56]

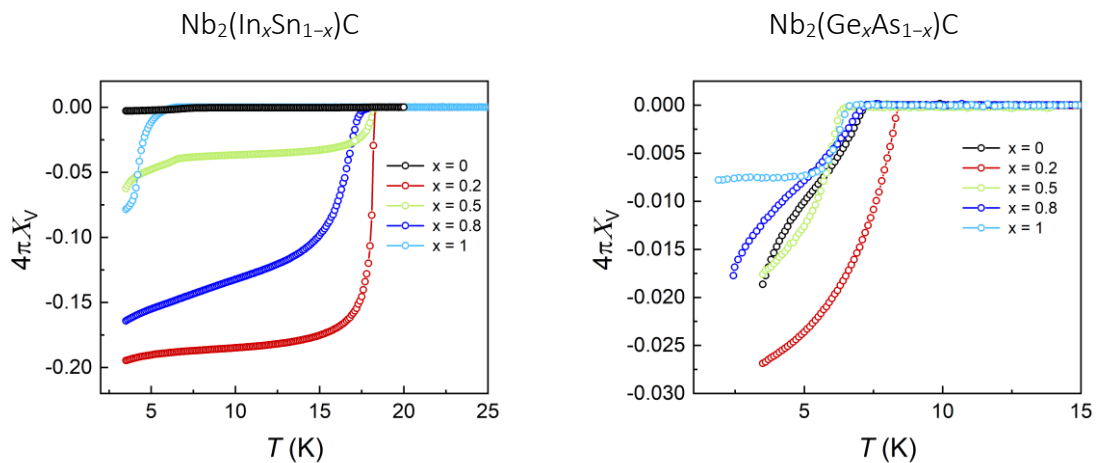


Figure 3-4: AC susceptibility measurements of the solid solutions $\text{Nb}_2(\text{In}_x\text{Sn}_{1-x})\text{C}$ from 3.5 to 25 K at 3 Oe (left). AC and VSM measurements of $\text{Nb}_2(\text{Ge}_x\text{As}_{1-x})\text{C}$ in the temperature range 1.9 - 8.0 K at 3 Oe and 15 Oe, respectively (right).

The same was found for Nb_2GeC (see Figure 3-4). This deviation from the behavior described in the literature is possibly due to changed synthesis conditions, which cause a slightly different product. For example, a lower occupation of the C-site can decrease the electron density on the

Fermi level and consequently affects the superconductivity. However, such changes could not be detected with the used analytic methods.

In summary, the susceptibility measurements reveal no superconductivity in the solid solutions $\text{Nb}_2(\text{In}_x\text{Sn}_{1-x})\text{C}$ and $\text{Nb}_2(\text{Ge}_x\text{As}_{1-x})\text{C}$. The impurity phases Nb_3Sn ($T_c = 18$ K) and NbC cause the diamagnetic signals (see Figure 3-4).^[57]

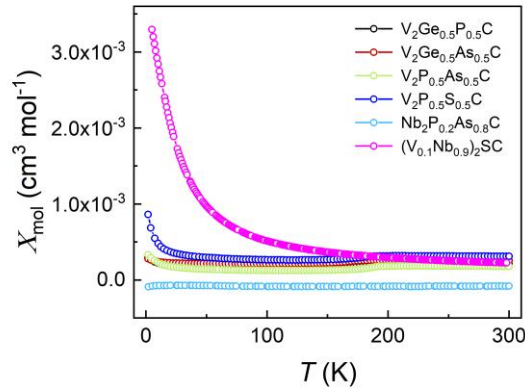


Figure 3-5: Magnetic susceptibility measurements at 20 kOe (1.8 – 300 K) of $\text{V}_2(\text{Ge}_{0.5}\text{P}_{0.5})\text{C}$, $\text{V}_2(\text{Ge}_{0.5}\text{As}_{0.5})\text{C}$, $\text{V}_2(\text{P}_{0.5}\text{As}_{0.5})\text{C}$ and $\text{V}_2(\text{P}_{0.5}\text{S}_{0.5})\text{C}$ (performed on a SQUID magnetometer) and at 30 kOe (1.9 – 300 K) of $\text{Nb}_2(\text{P}_{0.2}\text{As}_{0.8})\text{C}$ and $(\text{V}_{0.1}\text{Nb}_{0.9})_2\text{SC}$ (performed on a PPMS using the VSM option).

For the other solid solutions, $\text{V}_2(\text{Ge}_x\text{P}_{1-x})\text{C}$, $\text{V}_2(\text{Ge}_x\text{As}_{1-x})\text{C}$, $\text{V}_2(\text{P}_x\text{As}_{1-x})\text{C}$, $\text{V}_2(\text{P}_x\text{S}_{1-x})\text{C}$, $\text{Nb}_2(\text{P}_x\text{As}_{1-x})\text{C}$ and $(\text{V}_x\text{Nb}_{1-x})_2\text{SC}$ magnetic measurements were performed for only one compound representatively. They all exhibit Pauli paramagnetism above 2 K (see Figure 3-5). This was expected for $\text{V}_2(\text{Ge}_x\text{P}_{1-x})\text{C}$, $\text{V}_2(\text{Ge}_x\text{As}_{1-x})\text{C}$, $\text{V}_2(\text{P}_x\text{As}_{1-x})\text{C}$, $\text{V}_2(\text{P}_x\text{S}_{1-x})\text{C}$, and $\text{Nb}_2(\text{P}_x\text{As}_{1-x})\text{C}$, since the associated boundary phases are also Pauli paramagnetic. Surprisingly, however, the solid solutions $(\text{V}_x\text{Nb}_{1-x})_2\text{SC}$ are no longer superconducting. Even small amounts of vanadium seem to be enough to suppress superconductivity completely. This is unique since so far, small changes of the MAX phase, as in $\text{Nb}_2\text{S}(\text{B}_x\text{C}_{1-x})$ and $\text{Nb}_2(\text{As}_x\text{S}_{1-x})\text{C}$, had only a small impact on the critical temperature. This indicates that the $M-M$ interaction is important for superconductivity in MAX phases and that a minimal impact has a maximum effect.

Conclusion

The solid solutions $\text{V}_2(\text{Ge}_x\text{P}_{1-x})\text{C}$, $\text{V}_2(\text{Ge}_x\text{As}_{1-x})\text{C}$, $\text{V}_2(\text{P}_x\text{As}_{1-x})\text{C}$, $\text{V}_2(\text{P}_x\text{S}_{1-x})\text{C}$, $\text{Nb}_2(\text{Ge}_x\text{As}_{1-x})\text{C}$, $\text{Nb}_2(\text{In}_x\text{Sn}_{1-x})\text{C}$, $\text{Nb}_2(\text{P}_x\text{As}_{1-x})\text{C}$, $\text{Nb}_2(\text{As}_x\text{S}_{1-x})\text{C}$ and $(\text{V}_x\text{Nb}_{1-x})_2\text{SC}$ were synthesized via solid-state reactions starting from stoichiometric mixtures of the elements. High temperatures (1100 – 1280°C) and multiple reaction steps (2 – 9 times) are necessary to obtain the MAX phases with high phase proportions and reduced phase widths. However, it is not possible to

define an ideal synthesis route for these compounds. Rather, the conditions for each solid solution must be optimized individually.

The compounds crystallize in the hexagonal space group $P6_3/mmc$ (Cr_2AlC -type), like the corresponding boundary phases. Within the quaternary systems, lattice parameters change with the ion radii of the substituted elements and with the total number of electrons in the system, respectively. These changes are linear with the degree of substitution x . If possible, the compositions of the samples were determined from the PXRD data using Rietveld refinement. EDX measurements validated the stoichiometries. Both methods confirm the successful synthesis of the solid solution with the desired compositions.

Furthermore, measurements of the susceptibilities reveal the magnetic properties. $\text{Nb}_2(\text{As}_x\text{S}_{1-x})\text{C}$ are superconductors for $x \geq 0.7$ with a maximum T_c of 5.2 K at $x = 0.2$. The other solid solutions are non-superconducting Pauli paramagnets.

References

- [1] C. Hu, H. Zhang, F. Li, Q. Huang, Y. Bao, *Int. J. Refract. Met. Hard Mater.* **2013**, *36*, 300-312.
- [2] P. Eklund, J. Rosen, P. O. A. Persson, *J. Phys. D: Appl. Phys.* **2017**, *50*, 113001.
- [3] M. Sokol, V. Natu, S. Kota, M. W. Barsoum, *Trends Chem.* **2019**, *1*, 210-223.
- [4] M. Khazaei, A. Mishra, N. S. Venkataramanan, A. K. Singh, S. Yunoki, *Curr. Opin. Solid State Mater. Sci.* **2019**, 164-178.
- [5] C. Zhang, V. Nicolosi, *Energy Storage Mater.* **2019**, *16*, 102-125.
- [6] Y. Zhou, F. Meng, J. Zhang, *J. Am. Ceram. Soc.* **2008**, *91*, 1357-1360.
- [7] L. Zheng, J. Wang, X. Lu, F. Li, J. Wang, Y. Zhou, *J. Am. Ceram. Soc.* **2010**, *93*, 3068-3071.
- [8] A. S. Ingason, A. Mockute, M. Dahlgqvist, F. Magnus, S. Olafsson, U. B. Arnalds, B. Alling, I. A. Abrikosov, B. Hjörvarsson, P. O. Å. Persson, J. Rosen, *Phys. Rev. Lett.* **2013**, *110*, 195502.
- [9] Z. Liu, T. Waki, Y. Tabata, H. Nakamura, *Phys. Rev. B: Condens. Matter* **2014**, *89*, 054435.
- [10] A. Mockute, P. O. Å. Persson, F. Magnus, A. S. Ingason, S. Olafsson, L. Hultman, J. Rosen, *phys. status solidi – R* **2014**, *8*, 420-423.
- [11] C. M. Hamm, J. D. Bocarsly, G. Seward, U. I. Kramm, C. S. Birkel, *J. Mater. Chem. C* **2017**, *5*, 5700-5708.
- [12] C.-C. Lai, H. Fashandi, J. Lu, J. Palisaitis, P. O. Å. Persson, L. Hultman, P. Eklund, J. Rosen, *Nanoscale* **2017**, *9*, 17681-17687.
- [13] D. Horlait, S. C. Middleburgh, A. Chroneos, W. E. Lee, *Sci. Rep. - UK* **2016**, *6*, 18829.
- [14] M. Nechiche, T. Cabioc'h, E. N. Caspi, O. Rivin, A. Hoser, V. Gauthier-Brunet, P. Chartier, S. Dubois, *Inorg. Chem.* **2017**, *56*, 14388-14395.
- [15] B. Manoun, O. D. Leaffer, S. Gupta, E. N. Hoffman, S. K. Saxena, J. E. Spanier, M. W. Barsoum, *Solid State Commun.* **2009**, *149*, 1978-1983.
- [16] M. W. Barsoum, J. Golczewski, H. J. Seifert, F. Aldinger, *J. Alloys Compd.* **2002**, *340*, 173-179.
- [17] J. C. Schuster, H. Nowotny, C. Vaccaro, *J. Solid State Chem.* **1980**, *32*, 213-219.
- [18] S. Sridharan, H. Nowotny, *Z. Metallkd.* **1983**, *74*, 468-472.
- [19] I. Salama, T. El-Raghy, M. W. Barsoum, *J. Alloys Compd.* **2002**, *347*, 271-278.
- [20] R. Pan, J. Zhu, Y. Liu, *Mater. Sci. Technol.* **2018**, *34*, 1064-1069.

-
- [21] M. Naguib, G. W. Bentzel, J. Shah, J. Halim, E. N. Caspi, J. Lu, L. Hultman, M. W. Barsoum, *Mater. Res. Lett.* **2014**, *2*, 233-240.
- [22] T. Lapauw, B. Tunca, D. Potashnikov, A. Pesach, O. Ozeri, J. Vleugels, K. Lambrinou, *Sci. Rep. - UK* **2018**, *8*, 12801.
- [23] J. C. Schuster, H. Nowotny, *Z. Metallkd.* **1980**, *71*, 341-346.
- [24] E. a. N. Caspi, P. Chartier, F. Porcher, F. Damay, T. Cabioch, *Mater. Res. Lett.* **2015**, *3*, 100-106.
- [25] N. A. Phatak, S. K. Saxena, Y. Fei, J. Hu, *J. Alloys Compd.* **2009**, *475*, 629-634.
- [26] C. M. Hamm, M. Durrschnabel, L. Molina-Luna, R. Salikhov, D. Spoddig, M. Farle, U. Wiedwald, C. S. Birkel, *Mater. Chem. Front.* **2018**, *2*, 483-490.
- [27] J. Halim, J. Palisaitis, J. Lu, J. Thörnberg, E. J. Moon, M. Precner, P. Eklund, P. O. Å. Persson, M. W. Barsoum, J. Rosen, *ACS Appl. Nano Mater.* **2018**, *1*, 2455-2460.
- [28] C.-C. Lai, Q. Tao, H. Fashandi, U. Wiedwald, R. Salikhov, M. Farle, A. Petruhins, J. Lu, L. Hultman, P. Eklund, J. Rosen, *APL Mater.* **2018**, *6*, 026104.
- [29] D. Horlait, S. Grasso, A. Chronos, W. E. Lee, *Mater. Res. Lett.* **2016**, *4*, 137-144.
- [30] J. Etzkorn, M. Ade, D. Kotzott, M. Kleczek, H. Hillebrecht, *J. Solid State Chem.* **2009**, *182*, 995-1002.
- [31] W. Yu, S. Li, W. G. Sloof, *Mater. Sci. Eng., A* **2010**, *527*, 5997-6001.
- [32] T. Cabioch, P. Eklund, V. Mauchamp, M. Jaouen, M. W. Barsoum, *J. Eur. Ceram. Soc.* **2013**, *33*, 897-904.
- [33] C.-C. Lai, A. Petruhins, J. Lu, M. Farle, L. Hultman, P. Eklund, J. Rosen, *Mater. Res. Lett.* **2017**, *5*, 533-539.
- [34] T. Cabioch, P. Eklund, V. Mauchamp, M. Jaouen, *J. Eur. Ceram. Soc.* **2012**, *32*, 1803-1811.
- [35] M. A. Pietzka, J. C. Schuster, *J. Am. Ceram. Soc.* **1996**, *79*, 2321-2330.
- [36] T. Rackl, L. Eisenburger, R. Niklaus, D. Johrendt, *Phys. Rev. Mater.* **2019**, *3*, 054001.
- [37] A. Coelho, *TOPAS-Academic, Coelho Software* **2007**, *Version 4.1*.
- [38] H. Nowotny, W. Jeitschko, F. Benesovsky, *Planseeber. Pulvermetall.* **1964**, *12*, 31-43.
- [39] A. D. Bortolozzo, W. R. Osório, B. S. de Lima, C. A. M. Dos Santos, A. J. S. Machado, *Mater. Chem. Phys.* **2017**, *194*, 219-223.
- [40] O. Beckmann, H. Boller, H. Nowotny, *Monatsh. Chem.* **1968**, *99*, 1580-1583.
- [41] H. Boller, H. Nowotny, *Monatsh. Chem.* **1968**, *99*, 672-675.
- [42] H. Boller, H. Nowotny, *Monatsh. Chem.* **1966**, *97*, 1053-1058.

- [43] A. D. Bortolozzo, Z. Fisk, O. H. Sant'Anna, C. A. M. d. Santos, A. J. S. Machado, *Phys. C* **2009**, *469*, 256-258.
- [44] R. S. Kumar, S. Rekhi, A. L. Cornelius, M. W. Barsoum, *Appl. Phys. Lett.* **2005**, *86*, 111904.
- [45] S. E. Lofland, J. D. Hettinger, T. Meehan, A. Bryan, P. Finkel, S. Gupta, M. W. Barsoum, G. Hug, *Phys. Rev. B: Condens. Matter* **2006**, *74*, 174501.
- [46] O. Beckmann, H. Boller, H. Nowotny, *Monatsh. Chem.* **1968**, *99*, 1580-1583.
- [47] K. Sakamaki, H. Wada, H. Nozaki, Y. Ōnuki, M. Kawai, *Solid State Commun.* **1999**, *112*, 323-327.
- [48] K. Sakamaki, H. Wada, H. Nozaki, Y. Onuki, M. Kawai, *Mol. Cryst. Liq. Cryst. Sci. Technol. Sect. A* **2000**, *341*, 99-104.
- [49] E. L. Williams, *J. Am. Ceram. Soc.* **1965**, *48*, 190-194.
- [50] M. L. Hair, *J. Non-Cryst. Solids* **1975**, *19*, 299-309.
- [51] A. S. Ingason, M. Dahlqvist, J. Rosen, *J. Phys.: Condens. Matter* **2016**, *28*, 433003.
- [52] K. Sakamaki, H. Wada, H. Nozaki, Y. Ōnuki, M. Kawai, *Solid State Commun.* **2001**, *118*, 113-118.
- [53] A. D. Bortolozzo, G. Serrano, A. Serquis, D. Rodrigues, C. A. M. dos Santos, Z. Fisk, A. J. S. Machado, *Solid State Commun.* **2010**, *150*, 1364-1366.
- [54] A. D. Bortolozzo, O. H. Sant'Anna, M. S. da Luz, C. A. M. dos Santos, A. S. Pereira, K. S. Trentin, A. J. S. Machado, *Solid State Commun.* **2006**, *139*, 57-59.
- [55] B. W. Roberts, *J. Phys. Chem. Ref. Data* **1976**, *5*, 581-822.
- [56] R. Jha, V. P. S. Awana, *J. Supercond. Nov. Magn.* **2012**, *25*, 1421-1425.
- [57] B. T. Matthias, T. H. Geballe, S. Geller, E. Corenzwit, *Phys. Rev.* **1954**, *95*, 1435-1435.

4 Intercalated MAX phases M_3P_2C ($M = Nb, Ta$)

Abstract

The transition metal carbides M_3P_2C ($M = Nb, Ta$) were synthesized via solid-state reaction of the elements at high temperatures. Edge sharing layers of M_6C octahedra alternate with layers of edge-sharing P_6M trigonal prisms. STEM-HAADF imaging confirms the crystal structure and shows the “zigzag” stacking of the layers of octahedra. This stacking of layers is different from other MAX phases, which always showed a “zigzag” stacking of layers of M_6X octahedra and A element single layers so far. The crystal structure of these compounds exhibit a different stacking of the layers compared to MAX phases. Magnetic and resistivity measurements reveal Pauli paramagnetism and good electrical conductivity of $1.9 - 2.1 \cdot 10^{-6} \Omega m$.

Introduction

MAX phases are a group of compounds that share a similar composition of elements, a hexagonal crystal structure (space group $P6_3/mmc$), and unified properties of metals and ceramics. The M elements are early transition metals and lanthanoids. The A elements are mostly main group elements, but late transition metals like gold, copper, or palladium also incorporate into MAX phases. The X elements are boron, carbon, or nitrogen (see Figure 1-2). This enormous number of combinations of elements make the MAX phases a group of compounds with an impressive chemical diversity. Correlating to the changed compositions, they also alter physical properties or chemical reactivity.^[1-2] The probably most prominent example for this is that only those compounds with aluminum as the A element can be exfoliated to MXenes.^[3-4] In contrast to this chemical diversity, they are uniform in terms of crystal structure. All ternary MAX phases crystallize in the hexagonal space group $P6_3/mmc$. Layers of edge-sharing M_6X octahedra alternate with layers of A atoms. For $n = 1$ in $M_{n+1}AX_n$, there is a single layer of octahedra between the A atoms, for $n = 2$ a double, for $n = 3$ a triple.^[5-7] These metal-carbide layers are an excerpt from the corresponding binary compounds. As a result, the properties of $M_{n+1}AX_n$ compounds approach those of the rock salt MX phases with increasing n .^[2]

In 2017, Tao *et al.* showed an in-plane ordering of the metal atoms in $(Mo_{2/3}Sc_{1/3})_2AlC$. For the first time, this led to a symmetry reduction in MAX phases.^[8] All so-called *i*-MAX phases discovered so far crystallize in the space groups $C2/c$ or $Cmcm$.^[9-10]

However, the structural motif of layers of edge-sharing M_6X octahedra is also found in other phases. For example, Mo_2Ga_2C , Ta_2S_2C , Nb_2S_2C , Ti_2Au_2C and $Ti_3Au_2C_2$ exhibit a similar crystal structure and compositions to the MAX phases, although they differ in symmetry ($P\bar{3}m1$). Furthermore, they show a different stacking. Two A atom layers separate the MX layers, and they do not show the, for MAX phases typical, “zigzag” stacking of the layers of octahedra.^[11-14]

Herein, the synthesis, crystal structure, and some physical properties of M_3P_2C ($M = Nb, Ta$) are described. Measurements of the magnetic moments show Pauli paramagnetism and the absence of superconductivity in these compounds. Temperature-dependent measurements of the resistivity reveal good electrical conductivity of M_3P_2C ($M = Nb, Ta$).

Experimental

M_3P_2C ($M = Nb, Ta$) were synthesized via solid-state reaction. Stoichiometric mixtures of niobium (99.99 %, ~325 mesh, Alfa Aesar) or tantalum (99.98 %, ~100 mesh, Alfa Aesar), phosphorous (99.999 %, pieces, Chempur) and carbon (100 %, powder, ACROS Organics) were homogenized and pressed into pellets with a diameter of 5 mm (2 t, 5 min). A silica tube coated with a thin graphite layer, was used as a reaction vessel and sealed under vacuum. The sample was heated to 1280 °C within 2 h and a dwell time of 15 h, before cooling to room temperature within 2 h. This reaction step was repeated twice for Nb_3P_2C and five more times for Ta_3P_2C with intermediate homogenization steps. The products were polycrystalline black powders.

PXRD patterns were collected using a Huber G670 diffractometer ($Cu-K\alpha_1$, $\lambda = 1.54059 \text{ \AA}$, Ge-111 monochromator). For structure solution from the data of Nb_3P_2C , the TOPAS software package was used applying the charge flipping method. The same software package was used for Rietveld refinement of M_3P_2C ($M = Nb, Ta$).^[17]

For STEM-HAADF imaging a C_s dodecapole probe-corrected Titan Themis 300 (FEI, USA) TEM equipped with an extreme field emission gun, a postcolumn filter (Enfinium ER-799), an US1000XP/FT camera system (Gatan, Germany) and a windowless four-quadrant Super-X energy dispersive X-ray spectroscopy detector were used.

Magnetic and resistivity measurements were performed on a Quantum Design PPMS-9. The magnetic moments were determined from 1.9 – 20 K at an applied field of 15 Oe and from 2 – 300 K at an applied field of 30 kOe using the VSM option. The resistivity was determined in the temperature range from 2 – 300 K.

Results and discussion

Synthesis and crystal structure

The syntheses of M_3P_2C ($M = \text{Nb, Ta}$) were achieved via solid-state reactions of the elements. High temperatures (1280°C) and vacuum are necessary for the formation of these phases. Since the silica surface releases oxide ions under these conditions, it is essential to shield it from the reaction with a thin graphite layer.^[18-19] Furthermore, a reaction time longer than 15 h should be avoided, because the silica softens at these temperatures and becomes permeable to air. To increase the phase proportions of M_3P_2C ($M = \text{Nb, Ta}$) several reaction steps are necessary. The products were black polycrystalline powders. Rietveld refinement of the PXRD data revealed that $\text{Nb}_3\text{P}_2\text{C}$ (90 wt.%) was synthesized with the impurities Nb_2PC (8 wt.%) and NbC (2 wt.%), while $\text{Ta}_3\text{P}_2\text{C}$ (93 wt.%) was obtained with TaP (5 wt.%) and TaC (2 wt.%) (see Figure A-79 and A-80).

The crystal structure of $\text{Nb}_3\text{P}_2\text{C}$ was determined from PXRD data. $\text{Nb}_3\text{P}_2\text{C}$ crystallizes in the hexagonal space group $P6_3/mmc$ in a new structure type, to the best of our knowledge. It shows a layered structure, where layers of edge-sharing Nb_6C octahedra alternate with layers of edge-sharing P_6Nb trigonal prisms (see Figure 4-1). Rietveld refinement of the PXRD data revealed that $\text{Ta}_3\text{P}_2\text{C}$ exhibits the same structure. The lattice parameters with $a = 3.3 \text{ \AA}$ and $c = 18 \text{ \AA}$ are similar for both compounds (see Table 4-1).

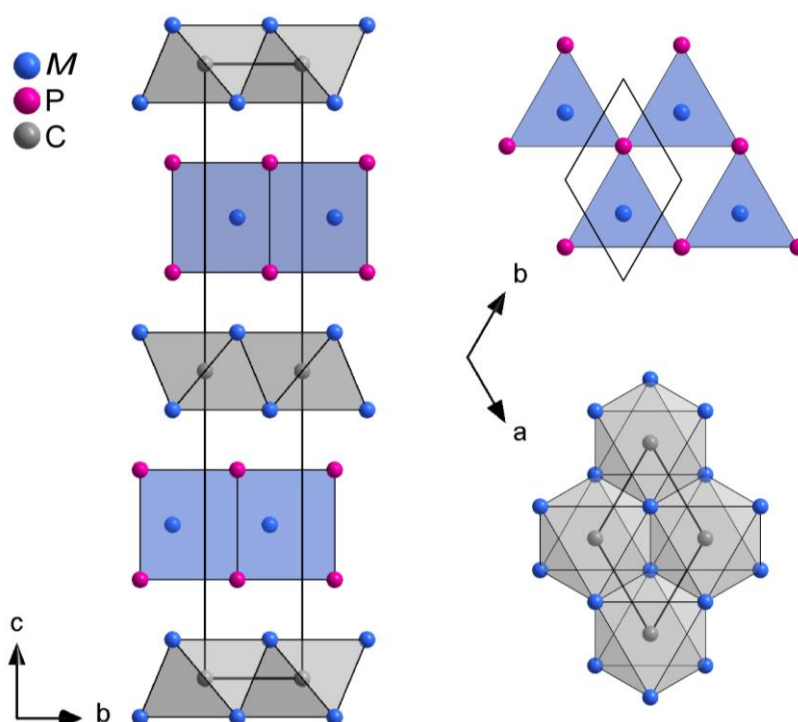


Figure 4-1: Crystal structure of M_3P_2C ($M = \text{Nb, Ta}$) with viewing direction along the a -axis (left) and layers of trigonal prisms as well as octahedra with viewing direction along the c -axis (right).

The structure can also be considered as a stacking of sections from the binary metal carbides (NbC, TaC) and metal phosphides (NbP, TaP). Thereby the interatomic distances in the octahedra of M_3P_2C (Nb1 — C: 2.226(1) Å, Ta1 — C: 2.219(1) Å) and of MC (Nb — C: 2.215 Å, Ta — C: 2.280 Å) are in good agreement to each other. Furthermore, the P — M2 distances in the trigonal-prism layers (Nb2 — P: 2.504(1) Å, Ta2 — P: 2.527(1) Å) correspond to those in the binary phosphides MP (Nb — P: 2.519 – 2.544 Å, Ta — P: 2.510 – 2.533 Å). In contrast, the M1 — P distance between the layers is longer (Nb — P: 2.601(1) Å, Ta — P: 2.555(2) Å). This suggests a pronounced two-dimensionality of these compounds.

Table 4-1: Crystallographic data of M_3P_2C ($M = Nb, Ta$) determined by Rietveld refinement of PXRD data.

Chemical formula	Nb ₃ P ₂ C	Ta ₃ P ₂ C				
M (g·mol ⁻¹)	352.68	616.80				
Crystal system, Space group	hexagonal, $P6_3/mmc$ (194)					
T (K)	293					
a (Å), c (Å)	3.3110(1), 18.0931(13)	3.2990(1), 18.0142(9)				
V (Å ³)	171.776(13)	169.788(11)				
Z	2					
Radiation type	Cu $K_{\alpha 1}$, $\lambda = 1.54056$ Å					
Diffractometer	Huber G670					
Monochromator	Ge-111					
R_p	1.680	1.746				
R_{wp}	2.494	2.528				
Goodness of fit	1.876	1.932				
Z_M	0.06311(2)	0.06328(2)				
Z_A	0.16062(9)	0.15784(12)				
Atom positions and equivalent isotropic displacement parameters (Å ²)						
Atom	Wyck.	x	y	z	U_{eq}	occ
$M1$	$4f$	1/3	2/3	Z_M	0.7	1
$M2$	$2c$	1/3	2/3	1/4	0.7	1
P	$4f$	2/3	1/3	Z_A	1	1
C	$2a$	0	0	0	3	1

The degree of distortion of the octahedra α_r (for a detailed explanation of this value see chapter 2.1) can be a measure of the stability of the layer, as shown for the solid solutions in chapter 2.3.^[20] Compared to the MAX phase Nb₂PC ($\alpha_r = 1.137$), the octahedra in Nb₃P₂C are stronger distorted ($\alpha_r = 1.158$). This trend might prevent the synthesis of further M_3A_2C phases. Since there is no MAX phase known in the Ta – P – C system, the distortion in Ta₃P₂C can only be compared to Nb₃P₂C. In both compounds, the octahedra are equally distorted (see Table 4-2).

Similar to α_r , the degree of distortion of the trigonal prism A_6M is given by the value β , which is the ratio of the $A - A$ distance in the basal plane ($d_{A-A} = a$), and the $A - M2$ distance (d_{A-M2}). By rearranging this formula, the value β depends on the lattice parameters and the z_A coordinate:

$$\beta_{\text{tp}} = \frac{d_{P-P}}{d_{P-M2}} = \frac{1}{\sqrt{\frac{1}{3} + (c/a)^2 (1/4 - z_A)^2}} \quad \text{Equation 4-1}$$

For an ideal trigonal prism, β_{tp} is 1. For M_3P_2C , the values are > 1 , which is equivalent to a compression along the c -axis. Even though the distortions for both compounds Nb₃P₂C ($\beta_{\text{tp}} = 1.322$) and Ta₃P₂C ($\beta_{\text{tp}} = 1.306$) are similar, they differ slightly, especially considering the unchanged octahedron distortion. In summary, both phases show similar unit cell dimensions, and the coordination polyhedra hardly differ. At the same time, the small difference in the crystal structure is most obvious in the layer of trigonal prisms. The distortions of the octahedra do not change, and the $M - M$ distances (corresponding to the a -axis) remain almost the same.

Table 4-2: Selected interatomic distances, the degree of distortion of the M_6C octahedra α_r , and of the P_6M trigonal prisms β in M_3P_2C ($M = \text{Nb, Ta}$).

	d_{C-M1} (Å)	d_{M1-P} (Å)	d_{P-M2} (Å)	d_{M-M} (Å)	α_r	β
Nb ₃ P ₂ C	2.226(1)	2.601(1)	2.504(1)	3.311(1)	1.158	1.322
Ta ₃ P ₂ C	2.219(1)	2.555(2)	2.527(1)	3.299(1)	1.157	1.306

Figure 4-2 shows the Nb₃P₂C structure perpendicular to [100] visualized by STEM-HAADF. Niobium can be assigned to the brightest and phosphorus to the darker intensity. Carbon cannot be located due to the small electron count and the environment of six niobium atoms. The for MAX phases characteristic “zigzag” stacking of the layers of Nb₆C octahedra is also observed for Nb₃P₂C, even though the layers are not only separated by one A atom, but by the three atom layers of the trigonal prisms $P_6\text{Nb}$.

Near the completion of this thesis, Chen et al. reported similar results about the compounds M_3P_2C ($M = Nb, Ta$) and M_3As_2C ($M = V, Nb$), that exhibit a structure similar to the MAX phases. Thereby, only Nb_3As_2C was prepared phase pure, M_3P_2C ($M = Nb, Ta$) with about 50 wt.%, and V_3As_2C only as a minor fraction. Furthermore, first-principle calculations reveal high bulk moduli, brittleness, high melting points, and outstanding stiffnesses.^[15-16]

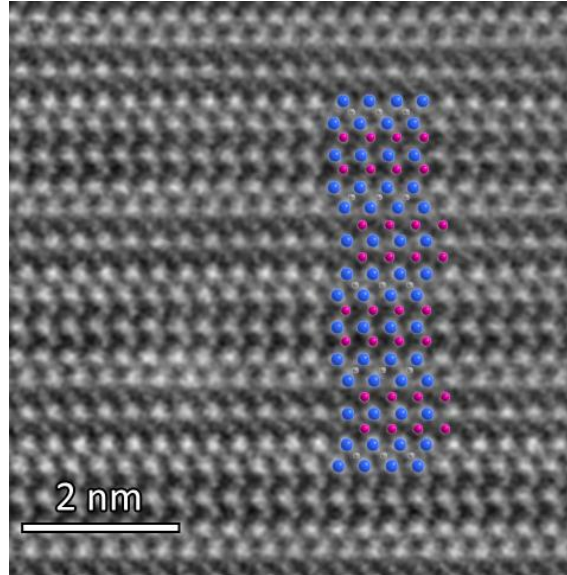


Figure 4-2: STEM-HAADF image of Nb_3P_2C perpendicular to $[100]$. The inset of the structure of Nb_3P_2C indicates the position of Nb (blue), P (pink), and C (gray) atoms.

Magnetic properties

Measurements of the magnetic moments for M_3P_2C ($M = Nb, Ta$) were performed on a Quantum Design PPMS using the VSM option (see Figure 4-3). The samples of the synthesis of Nb_3P_2C shows two ($T_{c,1} = 4.5$ K, $T_{c,2} = 9.0$ K) and of Ta_3P_2C shows one ($T_{c,3} = 6.6$ K) diamagnetic transition. Nevertheless, M_3P_2C ($M = Nb, Ta$) do not exhibit superconductivity above 2 K, due to the low volume fraction of these transitions in the volume susceptibility. $T_{c,1}$ cannot be assigned to a known impurity, $T_{c,2}$ is referred to unreacted niobium metal, and the TaC impurity causes the transition at $T_{c,3}$.^[21-22] Furthermore, measurements at an applied field of 30 kOe show small values, which are almost independent of temperature (see Figure A-81). This indicates a Pauli paramagnetic behavior of M_3P_2C ($M = Nb, Ta$).

The temperature-dependent measurements of the resistivity confirm the absence of superconductivity in M_3P_2C , since it does not reach zero even at low temperatures (see Figure 4-3). Nevertheless, the compounds are good metallic conductors with $2.1 \cdot 10^{-6} \Omega\text{m}$ ($\text{Nb}_3\text{P}_2\text{C}$) and $1.9 \cdot 10^{-6} \Omega\text{m}$ ($\text{Ta}_3\text{P}_2\text{C}$) at 300 K. These values are in the typical range of MAX phases, considering the impact of grain boundaries on the measurements.

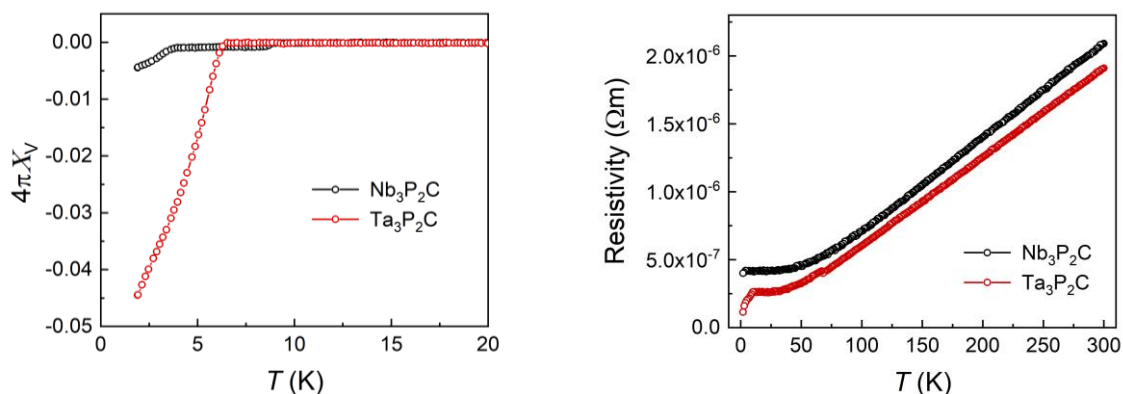


Figure 4-3: Volume susceptibility (*zfc*) from 2 – 20 K at 15 Oe (left) and resistivity from 2 – 300 K (right) of M_3P_2C ($M = \text{Nb}, \text{Ta}$).

Conclusion

M_3P_2C ($M = \text{Nb}, \text{Ta}$) were synthesized via solid-state reaction (1280°C). Starting from the elements, they were obtained as black polycrystalline powders with high phase proportions ($> 90 \text{ wt.}\%$). These carbides crystallize with a layered structure in the hexagonal space group $P6_3/mmc$. Layers of edge-sharing M_6C octahedra alternate with layers of edge-sharing P_6M trigonal prisms. Furthermore, STEM-HAADF imaging reveals the “zigzag” stacking of the layers of octahedra. Therefore M_3P_2C ($M = \text{Nb}, \text{Ta}$) show all characteristics of the MAX phases and can be assigned to these group of compounds. Magnetic and resistivity measurements show Pauli paramagnetism and a metallic behavior of the resistivity with $1.9 - 2.1 \cdot 10^{-6} \Omega\text{m}$ at 300 K.

References

- [1] M. Radovic, M. W. Barsoum, *Am. Ceram. Soc. Bull.* **2013**, *92*, 20-27.
- [2] M. Sokol, V. Natu, S. Kota, M. W. Barsoum, *Trends Chem.* **2019**, *1*, 210-223.
- [3] J.-C. Lei, X. Zhang, Z. Zhou, *Frontiers of Physics* **2015**, *10*, 276-286.
- [4] M. Khazaei, A. Mishra, N. S. Venkataramanan, A. K. Singh, S. Yunoki, *Curr. Opin. Solid State Mater. Sci.* **2019**, 164-178.
- [5] W. Jeitschko, H. Nowotny, F. Benesovsky, *Monatsh. Chem.* **1964**, *95*, 156-157.
- [6] W. Jeitschko, H. Nowotny, F. Benesovsky, *Monatsh. Chem.* **1964**, *95*, 178-179.
- [7] H. Nowotny, W. Jeitschko, F. Benesovsky, *Planseeber. Pulvermetall.* **1964**, *12*, 31-43.
- [8] M. Nechiche, T. Cabioc'h, E. N. Caspi, O. Rivin, A. Hoser, V. Gauthier-Brunet, P. Chartier, S. Dubois, *Inorg. Chem.* **2017**, *56*, 14388-14395.
- [9] M. Dahlgqvist, J. Lu, R. Meshkian, Q. Tao, L. Hultman, J. Rosen, *Science Advances* **2017**, *3*, e1700642.
- [10] M. Dahlgqvist, A. Petruhins, J. Lu, L. Hultman, J. Rosen, *ACS Nano* **2018**, *12*, 7761-7770.
- [11] C. Hu, C. C. Lai, Q. Tao, J. Lu, J. Halim, L. Sun, J. Zhang, J. Yang, B. Anasori, J. Wang, Y. Sakka, L. Hultman, P. Eklund, J. Rosen, M. W. Barsoum, *Chem. Commun.* **2015**, *51*, 6560-6563.
- [12] H. Fashandi, C. C. Lai, M. Dahlgqvist, J. Lu, J. Rosen, L. Hultman, G. Greczynski, M. Andersson, A. Lloyd Spetz, P. Eklund, *Chem. Commun.* **2017**, *53*, 9554-9557.
- [13] H. Boller, K. Hiebl, *J. Alloys Compd.* **1992**, *183*, 438-443.
- [14] O. Beckmann, H. Boller, H. Nowotny, *Monatsh. Chem.* **1970**, *101*, 945-955.
- [15] H. Chen, D. Yang, Q. Zhang, S. Jin, L. Guo, J. Deng, X. Li, X. Chen, *Angew. Chem. Int. Ed.* **2019**, *58*, 4576-4580.
- [16] M. A. Hadi, M. A. Rayhan, S. H. Naqib, A. Chroneos, A. K. M. A. Islam, in *arXiv e-prints*, **2019**.
- [17] A. Coelho, *TOPAS-Academic, Coelho Software* **2007**, *Version 4.1*.
- [18] M. L. Hair, *J. Non-Cryst. Solids* **1975**, *19*, 299-309.
- [19] E. L. Williams, *J. Am. Ceram. Soc.* **1965**, *48*, 190-194.
- [20] G. Hug, M. Jaouen, M. W. Barsoum, *Phys. Rev. B: Condens. Matter* **2005**, *71*, 024105.
- [21] D. K. Finnemore, T. F. Stromberg, C. A. Swenson, *Phys. Rev.* **1966**, *149*, 231-243.
- [22] R. H. Willens, E. Buehler, B. T. Matthias, *Phys. Rev.* **1967**, *159*, 327-330.

5 Summary

In this thesis, new members of the MAX phase family were prepared and investigated. Thereby, boron was successfully incorporated as the X element in these phases for the first time. In the first part, the syntheses of the ternary phases M_2SB ($M = \text{Zr, Hf, Nb}$) and of the solid solutions $\text{Nb}_2A(\text{B,C})$ ($A = \text{In, Sn, As, S}$) via solid-state reactions and the flux method are described. Moreover, magnetic and resistivity measurements, as well as DFT calculations, reveal typical MAX phase properties. The second part of this thesis focuses on the syntheses of solid solutions of MAX phases by independently altering the M and A elements. These compounds were analyzed by means of changes in the crystal structure and physical properties. Finally, within the third part the syntheses and crystal structure of the intercalated MAX phases M_3P_2C ($M = \text{Nb, Ta}$) are presented. An overview of all compounds synthesized and characterized within this thesis is given in Figure 5-1, and a summary of each chapter is provided below.

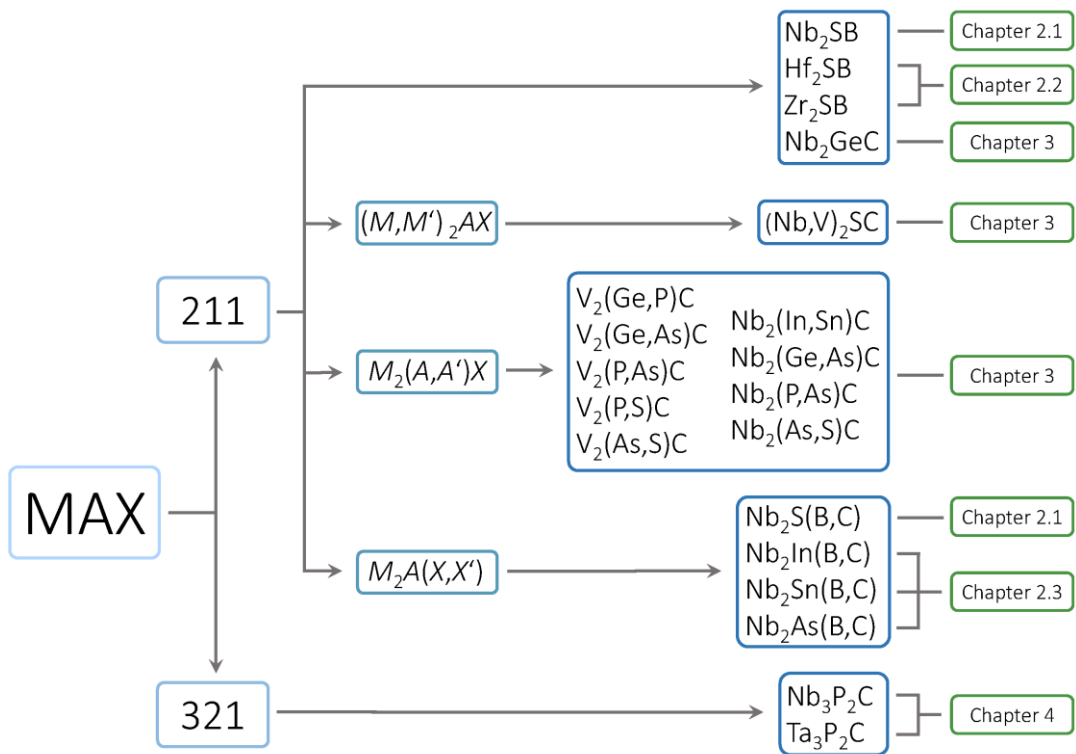


Figure 5-1: Overview of the compounds discussed in this thesis with reference to the corresponding chapter. MAX phases categorized according to their stoichiometry (211- and 321-type). The 211-type is further divided into ternary phases and solid solutions of the M [$(M, M')_2AX$], A [$M_2(A, A')X$], and X [$M_2A(X, X')$] elements.

MAX phase borides

Within Chapter 2, the syntheses and characterization of the first MAX phase borides are presented in three separate sections. The isomorphous compounds M_2SB ($M = \text{Zr, Hf, Nb}$) were synthesized via solid-state reaction. For Nb_2SB , it is advantageous to use a pre-reacted “ Nb_2S ”-mixture, whereas the pure elements serve as starting materials for M_2SB ($M = \text{Zr, Hf}$). The crystal structures were determined from PXRD data, revealing the space group $P6_3/mmc$ and the Cr_2AlC structure type. M_2SB ($M = \text{Zr, Hf, Nb}$) show a laminated structure of layers of edge-sharing M_6X octahedra and sulfur layers, as confirmed by STEM-HAADF imaging. The boride phases feature increased unit cell volumes (+3.9 – 6.6 %) and less distorted M_6X octahedra (–1.9 – 4.1 %), when compared to the corresponding carbide phases. M_2SB ($M = \text{Zr, Hf, Nb}$) are Pauli paramagnets and metallic conductors. Ab-initio calculations of the electronic band structure confirm the metallic state, with the $d-d$ interaction of the metals being dominant at the Fermi-level. The calculated Poisson’s ratios indicate an ionic bonding characteristic of MAX phase borides. These results agree with the calculations of the electron localization function (ELF). Furthermore, the elastic constants suggest M_2SB ($M = \text{Zr, Hf, Nb}$) to be brittle materials with lower melting points, reduced thermal conductivities, and less pronounced anisotropy, compared to the corresponding carbides.

Besides the ternary phases M_2SB ($M = \text{Zr, Hf, Nb}$), the solid solutions $\text{Nb}_2A(\text{B,C})$ ($A = \text{In, Sn, As, S}$) were successfully synthesized. The arsenic and sulfur compounds were synthesized via solid-state reaction, whereas the indium and tin compounds were prepared by the flux method using an excess of indium and tin, respectively. This method increases the phase proportion of the MAX phase and the homogeneity of the sample within the same reaction time. The excess indium or tin was dissolved using concentrated hydrochloric acid. During this dissolution process, the surface of the MAX phase passivates by forming a thin Nb_3Sn layer, which renders the compound chemically inert and also provides a thin superconducting layer ($T_c = 18 \text{ K}$). The solid solutions $\text{Nb}_2A(\text{B,C})$ ($A = \text{In, Sn, As, S}$) were investigated using Rietveld refinements of the PXRD data, which revealed the hexagonal Cr_2AlC structure type of all phases. By the substitution of carbon by boron, the total electron count of the compound decreases. This results in a linear increase of the unit cell dimensions and less distorted M_6X octahedra. The solid solutions $\text{Nb}_2A(\text{B,C})$ ($A = \text{Sn, As}$) show the same trend, but the cell dimensions of $\text{Nb}_2\text{In}(\text{B,C})$ remain unchanged upon substitution. Nevertheless, the high phase proportions (94 – 100 wt.%) together with product yields of 70 – 83 % indicate an incorporation of boron. The B:C ratio in $\text{Nb}_2A(\text{B,C})$ ($A = \text{In, Sn, As}$), however, could not be determined and the boundary phases Nb_2AB ($A = \text{In, Sn, As}$) remain unknown, thus far.

Magnetic and resistivity measurements render the solid solutions $\text{Nb}_2\text{SB}_x\text{C}_{1-x}$ as superconductors for $x = 0 - 0.6$ with a decreasing T_c for increasing boron content from 4.8 – 2.6 K. DFT calculations indicate the lowering of the density of states upon substitution of carbon by boron, which might be the main reason for the decreasing critical temperatures. The elastic constants and Debye temperatures of Nb_2SB and Nb_2SC are similar and, thus, cannot account for the absence of superconductivity in Nb_2SB . The solid solutions $\text{Nb}_2\text{A}(\text{B,C})$ ($\text{A} = \text{In, Sn, As}$) are not superconducting, even though the carbides Nb_2AC ($\text{A} = \text{In, Sn, As}$) are described as superconductors in the literature.

***M* and *A* site substitutions in MAX phases**

The possibility of forming solid solutions is a great attribute of MAX phases, as it allows the tuning and implementation of desired properties. Chapter 3 presents optimized synthetic procedures for the preparation of samples with high phase proportions. The solid solutions $M_2\text{A}_x\text{A}'_{1-x}\text{C}$ ($M = \text{V, Nb}$; $\text{A, A}' = \text{In, Ge, Sn, P, As, S}$) and $(\text{V}_x\text{Nb}_{1-x})_2\text{SC}$, as well as the boundary phase Nb_2GeC , were prepared via solid-state reactions. Although the solid solutions form at similar temperatures as the boundary phases (1100 – 1280 °C), individual reaction conditions were optimized for each compound.

The crystal structures of the as-obtained MAX phases were determined by means of Rietveld refinements of the PXRD data. All solid solutions crystallize in the hexagonal space group $P6_3/mmc$ (Cr_2AlC -type). For $\text{V}_2(\text{Ge}_x\text{P}_{1-x})\text{C}$, $\text{V}_2(\text{P}_x\text{As}_{1-x})\text{C}$, $\text{V}_2(\text{As}_x\text{S}_{1-x})\text{C}$, $\text{Nb}_2(\text{P}_x\text{As}_{1-x})\text{C}$, $\text{Nb}_2(\text{As}_x\text{S}_{1-x})\text{C}$, and $(\text{V}_x\text{Nb}_{1-x})_2\text{SC}$ the mixed occupancies (x) were refined. Additionally, EDX spectra were conducted, which support the X-ray data and confirm the targeted stoichiometries. Due to the lack of a significant difference in the electron count of the *A* elements in $\text{V}_2(\text{Ge}_x\text{As}_{1-x})\text{C}$, $\text{V}_2(\text{P}_x\text{S}_{1-x})\text{C}$, $\text{Nb}_2(\text{In}_x\text{Sn}_{1-x})\text{C}$, and $\text{Nb}_2(\text{Ge}_x\text{As}_{1-x})\text{C}$, we were not able to determine x by Rietveld refinement. However, the EDX data support the targeted value of x . The substitution of the *M* or the *A* element causes a change of cell dimensions in both the solid solutions with distinct differences of the atom sizes (e.g., $\text{V}_2(\text{Ge}_x\text{P}_{1-x})\text{C}$) and those with different electron counts (e.g., $\text{V}_2(\text{Ge}_x\text{As}_{1-x})\text{C}$). The refined lattice parameters a and c depend linearly on the degree of substitution x . Therefore, they can be used to estimate the degree of substitution if other methods cannot specify it. The change in the crystal structure (polyhedra distortion) can further be applied to estimate the stability of solid solutions and the corresponding boundary phases. For $\text{V}_2(\text{P}_x\text{S}_{1-x})\text{C}$, $\text{V}_2(\text{As}_x\text{S}_{1-x})\text{C}$, and $(\text{V}_x\text{Nb}_{1-x})_2\text{SC}$, the boundary phase V_2SC is not known. Limits of substitution are at $x_{\text{max}} = 0.4$ for $\text{V}_2(\text{P}_x\text{S}_{1-x})\text{C}$, $x_{\text{max}} = 0.5$ for $\text{V}_2(\text{As}_x\text{S}_{1-x})\text{C}$ and $x_{\text{max}} = 0.5$ for $(\text{V}_x\text{Nb}_{1-x})_2\text{SC}$. The substitution in these phases is attended by a distortion of the trigonal prism

M_6A . The substitution in MAX phases with unknown boundary phases may thus be limited by the strain that is caused by the distortion of the M_6A prisms.

Besides the structural changes, the impact of substitution on the magnetic properties was investigated. In line with the corresponding boundary phases, $V_2(\text{Ge}_x\text{P}_{1-x})\text{C}$, $V_2(\text{Ge}_x\text{As}_{1-x})\text{C}$, $V_2(\text{P}_x\text{As}_{1-x})\text{C}$, $V_2(\text{P}_x\text{S}_{1-x})\text{C}$, and $\text{Nb}_2(\text{P}_x\text{As}_{1-x})\text{C}$ exhibit Pauli paramagnetism. The reported superconductivity of Nb_2InC , Nb_2GeC , Nb_2SnC , and Nb_2AsC could not be confirmed within this thesis. Accordingly, the solid solutions $\text{Nb}_2(\text{In}_x\text{Sn}_{1-x})\text{C}$ and $\text{Nb}_2(\text{Ge}_x\text{As}_{1-x})\text{C}$ do not show superconductivity as well. Contrary, $\text{Nb}_2(\text{As}_x\text{S}_{1-x})\text{C}$ are superconductors for $x = 0 - 0.7$ and exhibit a maximum critical temperature of 5.2 K at $x = 0.2$. The impact on the magnetic behavior increases, if niobium rather than sulfur is substituted in Nb_2SC (e.g. $(\text{V}_x\text{Nb}_{1-x})_2\text{SC}$). Even minimal amounts of vanadium ($x < 0.05$) completely suppress superconductivity. This renders the $M - M$ interaction as important for superconductivity in MAX phases. In summary, the absence of superconductivity in $\text{Nb}_2(\text{In}_x\text{Sn}_{1-x})\text{C}$ and $\text{Nb}_2(\text{Ge}_x\text{As}_{1-x})\text{C}$ might be due to slightly changed synthesis conditions compared to the literature. For example, these changes cause a lower occupation of the C site, which causes a reduction of the electron density at the Fermi level and thus lowers T_c .

Intercalated MAX Phases M_3P_2C ($M = \text{Nb}, \text{Ta}$)

Structural changes like in ordered MAX phases and the formation of new stacking types are rare. Chapter 4 is about a unique type of MAX phases. The carbides M_3P_2C ($M = \text{Nb}, \text{Ta}$) form via solid-state reaction of the elements and feature P_6M interlayers that have not been observed in MAX phases. Just as all MAX phases, M_3P_2C ($M = \text{Nb}, \text{Ta}$) crystallize in the hexagonal space group $P6_3/mmc$, but exhibit a different stacking. Layers of edge-sharing M_6C octahedra alternate with layers of edge-sharing trigonal P_6M prisms, reminiscent to the crystal structures of the respective carbides (NbC , TaC) and phosphides (NbP , TaP). Thereby, the interatomic distances in M_3P_2C ($M = \text{Nb}, \text{Ta}$) accord to those of the binary phases. Compared to the interatomic distances in the trigonal prisms, however, the $M - P$ distances between the layers are elongated, suggesting a quasi-two-dimensional character. STEM-HAADF imaging of $\text{Nb}_3\text{P}_2\text{C}$ confirms the stacking of the layers and further illustrates the typical “zigzag” stacking of the layers of octahedra in MAX phases. In summary, the compounds M_3P_2C ($M = \text{Nb}, \text{Ta}$) exhibit all structural criteria of MAX phases and can, therefore, be assigned to this family, although the composition differs from the general formula $M_{n+1}AX_n$. Magnetic and resistivity measurements reveal Pauli paramagnetism and a high electrical conductivity of $1.9 - 2.1 \cdot 10^{-6} \Omega\text{m}$.

6 Conclusion

This thesis covers the synthesis of numerous new members of the MAX phase family that have been studied extensively concerning their structural and materials properties. For the first time, boron was incorporated into MAX phases, which extends the elemental diversity in this compound class. On account of a detailed study of the synthesis conditions of M_2SB ($M = \text{Zr, Hf, Nb}$) and $\text{Nb}_2A(\text{B,C})$ ($A = \text{In, Sn, As, S}$) the preparation of further MAX phase borides was enabled. Physical properties such as superconductivity, anisotropy, and elastic properties were altered by the substitution of carbon by boron. To entirely determine the changed properties and to develop a possible pathway to quasi-two-dimensional MXene borides. However, additional investigations are necessary.

Besides the incorporation of boron in the MAX phase family, the solid solutions $M_2A_xA'_{1-x}C$ ($M = \text{V, Nb; } A, A' = \text{In, Ge, Sn, P, As, S}$) and $(\text{V}_x\text{Nb}_{1-x})_2\text{SC}$ were systematically investigated, to achieve phase pure samples that are required for potential applications. The trends in crystal structure changes can be used to determine x and to estimate the stability of solid solutions, where one boundary phase is not accessible. The substitution in MAX phases may thus be limited by the strain caused by the distortion of the M_6A prisms. Furthermore, we could show that superconductivity in MAX phases depends on the synthesis method and that the $M - M$ interaction is crucial for the critical temperature. These results extend the knowledge about superconductivity in MAX phases, which has only sparsely been investigated for these compounds.

The carbides M_3P_2C ($M = \text{Nb, Ta}$) exhibit a novel and expanded stacking of layers. These compounds are new members within the MAX phase family and increase their structural diversity. The fact that an interlayer of P_6M trigonal prisms can alternate with the layers of M_6C octahedra raises the question of whether other interlayers may be feasible as well.

The results of this thesis significantly increase both the elemental and structural diversity of MAX phases. Systematic and strategic research can further expand this material family, even by conventional synthesis methods like solid-state reaction. Due to unified properties of metals, ceramics and 2D-materials, MAX phases and MXenes are in focus of current research, while their number is steadily increasing. Through the cooperation of chemists, physicists, and materials scientists, they have the potential to improve our technologies in many areas.

A Appendix

A. 1 Crystallographic data, Rietveld refinement, magnetization measurements and phonon DOS of $\text{Nb}_2\text{SB}_x\text{C}_{1-x}$ ($x = 0 - 1$)

A.1.1 Crystallographic data

Table A-1: Crystallographic data, coordinate z_M of the M atom and aspect ratio α_r of $\text{Nb}_2\text{SB}_x\text{C}_{1-x}$ ($x = 0 - 0.8$).

Chemical formula	Nb_2SC	$\text{Nb}_2\text{SB}_{0.05}\text{C}_{0.95}$	$\text{Nb}_2\text{SB}_{0.2}\text{C}_{0.8}$
M (g·mol ⁻¹)	229.90	229.84	229.66
Crystal system,	hexagonal,	hexagonal,	hexagonal,
Space group	$P6_3/mmc$ (194)	$P6_3/mmc$ (194)	$P6_3/mmc$ (194)
T (K)	293	293	293
a (Å), c (Å)	3.279(1), 11.49(1)	3.284(1), 11.50(1)	3.293(1), 11.51(1)
V (Å ³)	107.0(1)	107.5(1)	108.1(1)
Z	2	2	2
Radiation type	Cu- $K_{\alpha 1}$, $\lambda = 1.54056$ Å	Cu- $K_{\alpha 1}$, $\lambda = 1.54056$ Å	Cu- $K_{\alpha 1}$, $\lambda = 1.54056$ Å
Diffractometer	Huber G670	Huber G670	Huber G670
Monochromator	Ge-111	Ge-111	Ge-111
R_p	2.293	2.162	2.072
R_{wp}	3.283	3.119	2.928
Goodness of fit	1.722	1.739	1.538
z_M	0.09716(6)	0.09717(5)	0.09758(6)
α_r	1.171	1.171	1.169
Chemical formula	$\text{Nb}_2\text{SB}_{0.4}\text{C}_{0.6}$	$\text{Nb}_2\text{SB}_{0.6}\text{C}_{0.4}$	$\text{Nb}_2\text{SB}_{0.8}\text{C}_{0.2}$
M (g·mol ⁻¹)	229.42	229.18	228.94
Crystal system,	hexagonal,	hexagonal,	hexagonal,
Space group	$P6_3/mmc$ (194)	$P6_3/mmc$ (194)	$P6_3/mmc$ (194)
T (K)	293	293	293
a (Å), c (Å)	3.298(1), 11.52(1)	3.304(1), 11.52(1)	3.320(1), 11.54(1)
V (Å ³)	108.5(1)	108.9(1)	110.1(1)
Z	2	2	2
Radiation type	Cu- $K_{\alpha 1}$, $\lambda = 1.54056$ Å	Cu- $K_{\alpha 1}$, $\lambda = 1.54056$ Å	Cu- $K_{\alpha 1}$, $\lambda = 1.54056$ Å
Diffractometer	Huber G670	Huber G670	Huber G670
Monochromator	Ge-111	Ge-111	Ge-111
R_p	2.516	1.529	2.060
R_{wp}	3.753	2.159	2.864
Goodness of fit	2.129	1.202	1.466
z_M	0.09849(4)	0.09944(5)	0.1008(1)
α_r	1.161	1.153	1.143

Table A-2: Crystallographic data, coordinate z_M of the M atom and aspect ratio α_r of $\text{Nb}_2\text{SB}_x\text{C}_{1-x}$ ($x = 0 - 0.8$).

Chemical formula	$\text{Nb}_2\text{SB}_{0.95}\text{C}_{0.05}$	Nb_2SB
M ($\text{g}\cdot\text{mol}^{-1}$)	228.76	228.70
Crystal system,	hexagonal,	hexagonal,
Space group	$P6_3/mmc$ (194)	$P6_3/mmc$ (194)
T (K)	293	293
a (\AA), c (\AA)	3.331(1), 11.53(1)	3.335(1), 11.55(1)
V (\AA^3)	110.8(1)	111.2(1)
Z	2	2
Radiation type	$\text{Cu-K}\alpha_1$, $\lambda = 1.54056 \text{ \AA}$	$\text{Cu-K}\alpha_1$, $\lambda = 1.54056 \text{ \AA}$
Diffractometer	Huber G670	Huber G670
Monochromator	Ge-111	Ge-111
R_p	2.557	2.287
R_{wp}	3.841	3.443
Goodness of fit	2.140	1.923
z_M	0.1020(1)	0.1032(1)
α_r	1.135	1.124

The Rietveld refinements of the powder patterns of all synthesized $\text{Nb}_2\text{SB}_x\text{C}_{1-x}$ compounds are displayed in Figure A-1 – A-8. The small hills at about 18° , 21° and 24° are due to the measuring set up of the Huber G670 diffractometer. Most of the samples contain impurity phases, namely NbC, NbB, and $\text{Nb}_{0.92}\text{S}$, which are stated in each pattern. Furthermore, for $x \geq 0.6$, unidentified phases are present in the powder patterns.

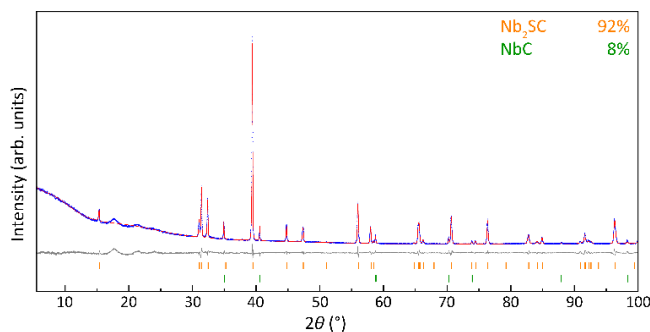


Figure A-1: X-ray powder pattern of Nb_2SC (blue) with Rietveld fit (red) and difference curve (gray).

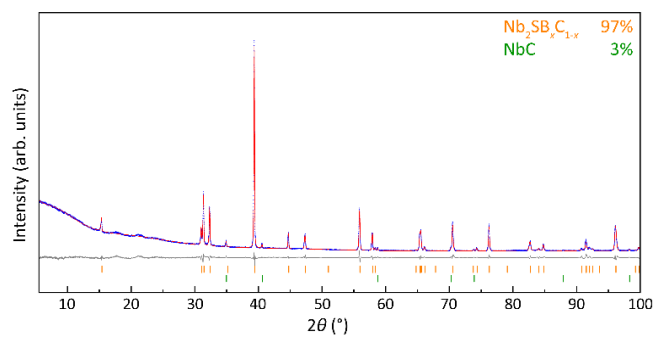


Figure A-2: X-ray powder pattern of $\text{Nb}_2\text{SB}_{0.05}\text{C}_{0.95}$ (blue) with Rietveld fit (red) and difference curve (gray).

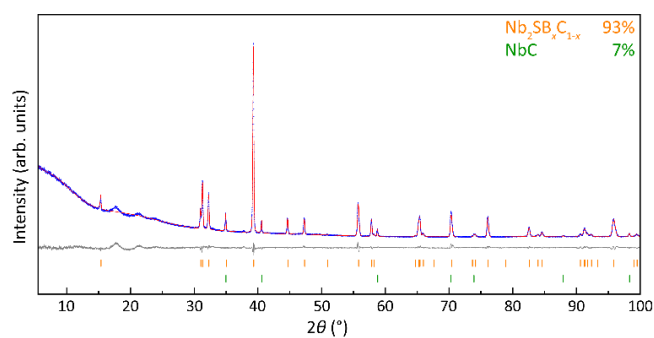


Figure A-3: X-ray powder pattern of $\text{Nb}_2\text{SB}_{0.2}\text{C}_{0.8}$ (blue) with Rietveld fit (red) and difference curve (gray).

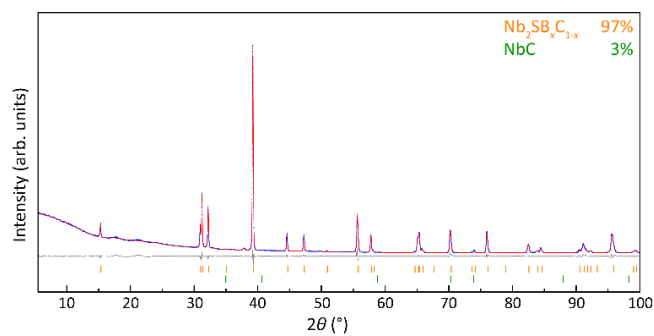


Figure A-4: X-ray powder pattern of $\text{Nb}_2\text{SB}_{0.4}\text{C}_{0.6}$ (blue) with Rietveld fit (red) and difference curve (gray).

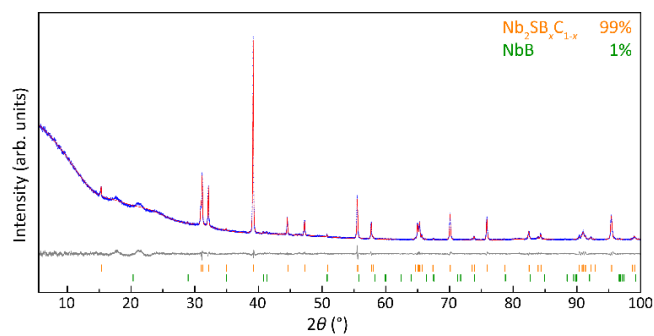


Figure A-5: X-ray powder pattern of $\text{Nb}_2\text{SB}_{0.6}\text{C}_{0.4}$ (blue) with Rietveld fit (red) and difference curve (gray).

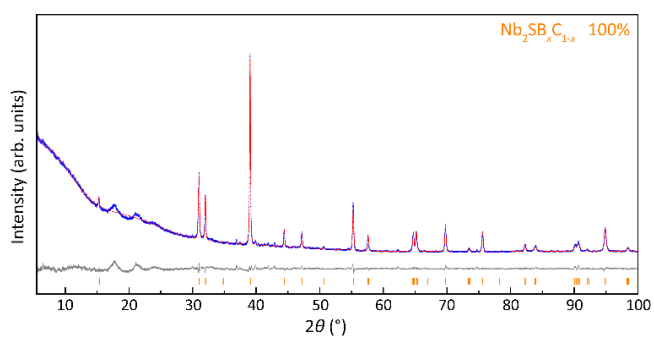


Figure A-6: X-ray powder pattern of $\text{Nb}_2\text{SB}_{0.8}\text{C}_{0.2}$ (blue) with Rietveld fit (red) and difference curve (gray).

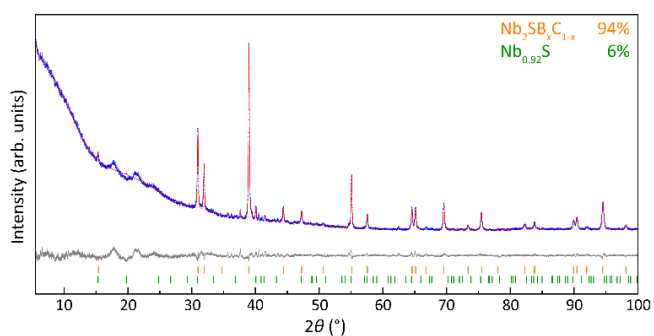


Figure A-7: X-ray powder pattern of $\text{Nb}_2\text{SB}_{0.95}\text{C}_{0.05}$ (blue) with Rietveld fit (red) and difference curve (gray).

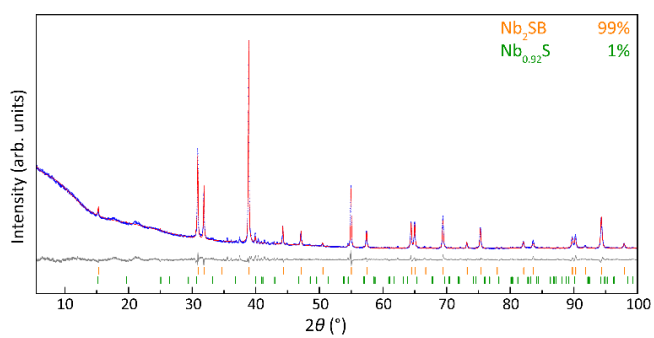
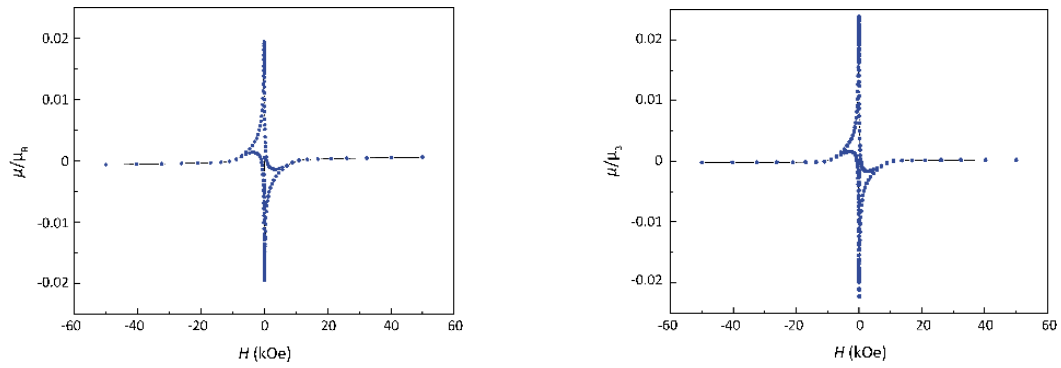
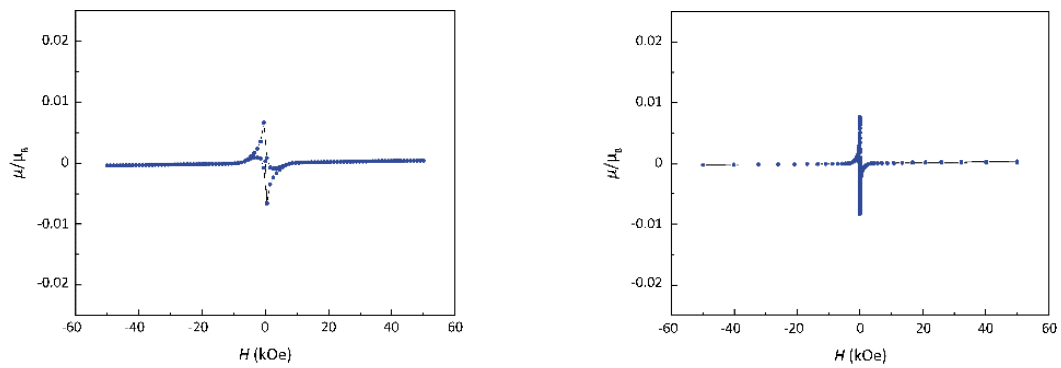
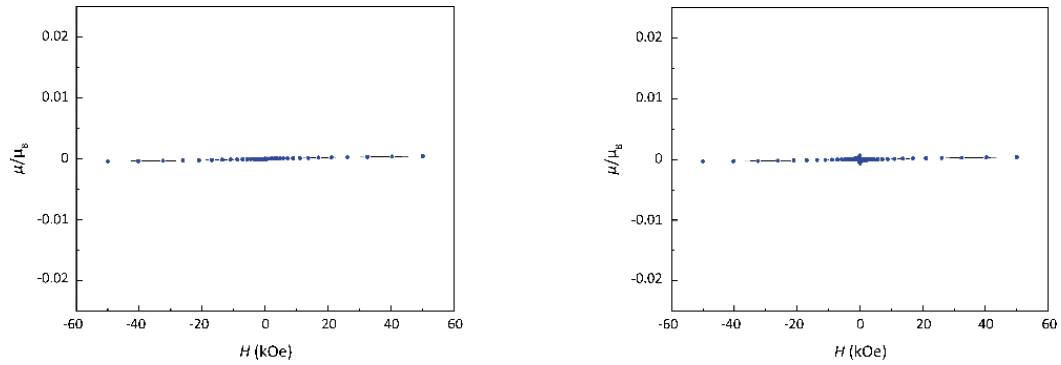
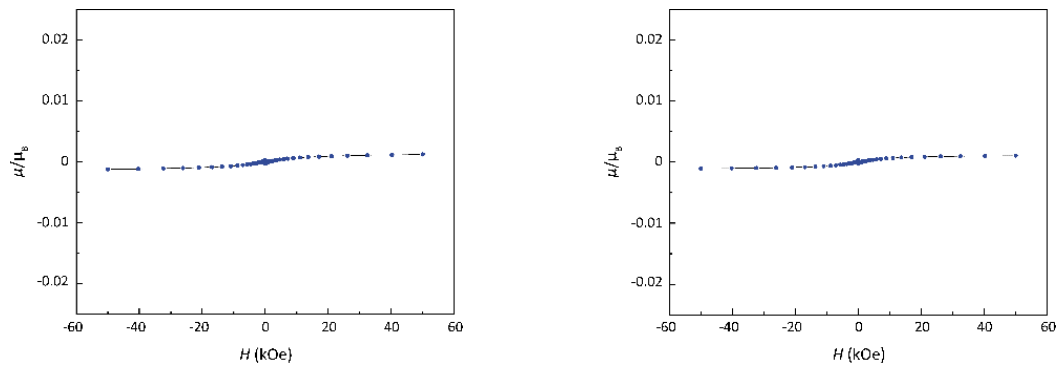


Figure A-8: X-ray powder pattern of Nb_2SB (blue) with Rietveld fit (red) and difference curve (gray).

A.1.2 Magnetization Isotherms

Figure A-9: Magnetization isotherm of Nb₂SC (left) and Nb₂SB_{0.05}C_{0.95} (right) at 1.9 K.Figure A-10: Magnetization isotherm of Nb₂SB_{0.2}C_{0.8} (left) and Nb₂SB_{0.4}C_{0.6} (right) at 1.9 K.Figure A-11: Magnetization isotherm of Nb₂SB_{0.6}C_{0.4} (left) and Nb₂SB_{0.8}C_{0.2} (right) at 1.9 K.Figure A-12: Magnetization isotherm of Nb₂SB_{0.95}C_{0.05} (left) and Nb₂SB (right) at 1.9 K.

A.1.3 Phonon DOS

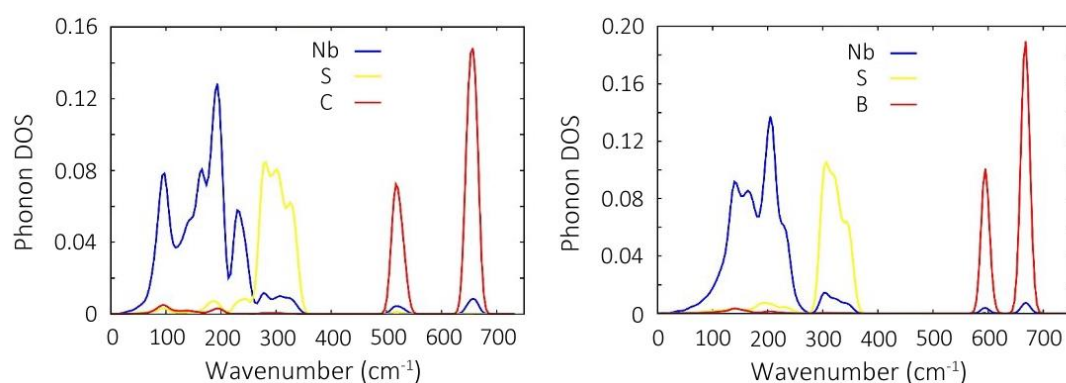


Figure A-13: Projected phonon density of states for Nb_2SC and Nb_2SB as calculated from supercells within the VASP program and evaluated by PHONOPY.

Phonon calculations were carried out after structural relaxations with the Vienna ab initio simulation package (VASP).^[1-3] Exchange correlation was treated in terms of the generalized gradient approximation (GGA) of Perdew, Burke, and Ernzerhof (PBE) revised for solids (PBEsol) and the projector-augmented-wave (PAW) method.^[4-8] Brillouin sampling was carried out on a Γ -centered k -mesh of $16 \times 16 \times 6$, while the plane-wave cut-off was set to 535 eV. Total energies of the unit cells were converged to 10^{-7} eV/atom with the residual atomic forces below 1×10^{-3} eV/Å. For the phonon calculations, $2 \times 2 \times 2$ supercells were calculated with a k -mesh sampling of $8 \times 8 \times 3$. Calculations of force sets and lattice vibrations were subsequently calculated from the PHONOPY program.^[9-10]

A. 2 Crystallographic data and Rietveld refinement of Nb₂A(B,C) (A = As, In, Sn)

A.2.1 Crystallographic data

Table A-3: Crystallographic data of Nb₂AsB_xC_{1-x} (x = 0.2, 0.4, 0.6, 0.8) and Nb₂SnB_xC_{1-x} (x = 0, 0.2) determined from PXRD data using Rietveld refinement.

Chemical formula	Nb ₂ AsB _{0.2} C _{0.8}	Nb ₂ AsB _{0.4} C _{0.6}	Nb ₂ AsB _{0.6} C _{0.4}
<i>M</i> (g·mol ⁻¹)	272.51	272.27	272.03
Crystal system,	hexagonal,	hexagonal,	hexagonal,
Space group	<i>P6₃/mmc</i> (194)	<i>P6₃/mmc</i> (194)	<i>P6₃/mmc</i> (194)
<i>T</i> (K)	293	293	293
<i>a</i> (Å), <i>c</i> (Å)	3.3275(1), 11.9259(1)	3.3329(1), 11.9257(1)	3.3368(1), 11.9258(1)
<i>V</i> (Å ³)	114.352(1)	114.722(1)	114.997(1)
<i>Z</i>	2	2	2
Radiation type	Cu-K _{α1} , λ = 1.54056 Å	Cu-K _{α1} , λ = 1.54056 Å	Cu-K _{α1} , λ = 1.54056 Å
Diffractionmeter	Huber G670	Huber G670	Huber G670
Monochromator	Ge-111	Ge-111	Ge-111
<i>R_p</i>	2.406	2.83	2.537
<i>R_{wp}</i>	3.884	4.433	3.432
Goodness of fit	2.07	2.391	1.817
<i>z_M</i>	0.09578(3)	0.09638(4)	0.09702(6)
<i>α_r</i>	1.163	1.158	1.153
Chemical formula	Nb ₂ AsB _{0.8} C _{0.2}	Nb ₂ SnC	Nb ₂ SnB _{0.2} C _{0.8}
<i>M</i> (g·mol ⁻¹)	271.79	316.54	316.3
Crystal system,	hexagonal,	hexagonal,	hexagonal,
Space group	<i>P6₃/mmc</i> (194)	<i>P6₃/mmc</i> (194)	<i>P6₃/mmc</i> (194)
<i>T</i> (K)	293	293	293
<i>a</i> (Å), <i>c</i> (Å)	3.3434(1), 11.9313(1)	3.2465(1), 13.7711(6)	3.2444(1), 13.7824(1)
<i>V</i> (Å ³)	115.506(1)	125.697(9)	125.640(1)
<i>Z</i>	2	2	2
Radiation type	Cu-K _{α1} , λ = 1.54056 Å	Cu-K _{α1} , λ = 1.54056 Å	Cu-K _{α1} , λ = 1.54056 Å
Diffractionmeter	Huber G670	Huber G670	Huber G670
Monochromator	Ge-111	Ge-111	Ge-111
<i>R_p</i>	2.724	1.953	2.066
<i>R_{wp}</i>	4.045	2.8	3.085
Goodness of fit	2.165	1.402	1.56
<i>z_M</i>	0.09761(5)	0.08368(12)	0.08379(9)
<i>α_r</i>	1.148	1.13	1.127

Table A-4: Crystallographic data of $\text{Nb}_2\text{SnB}_x\text{C}_{1-x}$ ($x = 0.4, 0.6, 0.8$) and $\text{Nb}_2\text{InB}_x\text{C}_{1-x}$ ($x = 0, 0.2, 0.4, 0.6, 0.8$) determined from PXRD data using Rietveld refinement.

Chemical formula	$\text{Nb}_2\text{SnB}_{0.4}\text{C}_{0.6}$	$\text{Nb}_2\text{SnB}_{0.6}\text{C}_{0.4}$	$\text{Nb}_2\text{SnB}_{0.8}\text{C}_{0.2}$
M ($\text{g}\cdot\text{mol}^{-1}$)	316.06	315.82	315.58
Crystal system,	hexagonal,	hexagonal,	hexagonal,
Space group	$P6_3/mmc$ (194)	$P6_3/mmc$ (194)	$P6_3/mmc$ (194)
T (K)	293	293	293
a (Å), c (Å)	3.2456(2), 13.7824(4)	3.2459(2), 13.7845(9)	3.2549(1), 13.7957(6)
V (Å ³)	125.732(11)	125.775(20)	126.573(6)
Z	2	2	2
Radiation type	Cu- $K_{\alpha 1}$, $\lambda = 1.54056$ Å	Cu- $K_{\alpha 1}$, $\lambda = 1.54056$ Å	Cu- $K_{\alpha 1}$, $\lambda = 1.54056$ Å
Diffractometer	Huber G670	Huber G670	Huber G670
Monochromator	Ge-111	Ge-111	Ge-111
R_p	2.319	2.472	2.649
R_{wp}	3.564	3.707	3.857
Goodness of fit	1.819	9.525	1.913
z_M	0.08384(10)	0.08396(11)	0.08462(23)
α_r	1.127	1.125	1.12
Chemical formula	Nb_2InC	$\text{Nb}_2\text{InB}_{0.2}\text{C}_{0.8}$	$\text{Nb}_2\text{InB}_{0.4}\text{C}_{0.6}$
M ($\text{g}\cdot\text{mol}^{-1}$)	312.65	312.41	312.17
Crystal system,	hexagonal,	hexagonal,	hexagonal,
Space group	$P6_3/mmc$ (194)	$P6_3/mmc$ (194)	$P6_3/mmc$ (194)
T (K)	293	293	293
a (Å), c (Å)	3.1729(1), 14.3733(1)	3.1734(1), 14.3736(1)	3.1735(1), 14.3724(2)
V (Å ³)	125.311(1)	125.354(1)	125.356(3)
Z	2	2	2
Radiation type	Cu- $K_{\alpha 1}$, $\lambda = 1.54056$ Å	Cu- $K_{\alpha 1}$, $\lambda = 1.54056$ Å	Cu- $K_{\alpha 1}$, $\lambda = 1.54056$ Å
Diffractometer	Huber G670	Huber G670	Huber G670
Monochromator	Ge-111	Ge-111	Ge-111
R_p	2.265	2.248	1.685
R_{wp}	3.178	3.326	2.247
Goodness of fit	1.637	1.674	1.14
z_M	0.08384(13)	0.08350(9)	0.08467(37)
α_r	1.066	1.07	1.063

Chemical formula	$\text{Nb}_2\text{InB}_{0.6}\text{C}_{0.4}$	$\text{Nb}_2\text{InB}_{0.8}\text{C}_{0.2}$
M ($\text{g}\cdot\text{mol}^{-1}$)	311.93	311.69
Crystal system,	hexagonal,	hexagonal,
Space group	$P6_3/mmc$ (194)	$P6_3/mmc$ (194)
T (K)	293	293
a (\AA), c (\AA)	3.1722(1), 14.3677(1)	3.1724(1), 14.3676(7)
V (\AA^3)	125.213(1)	125.226(8)
Z	2	2
Radiation type	$\text{Cu-K}\alpha_1$, $\lambda = 1.54056 \text{ \AA}$	$\text{Cu-K}\alpha_1$, $\lambda = 1.54056 \text{ \AA}$
Diffractometer	Huber G670	Huber G670
Monochromator	Ge-111	Ge-111
R_p	2.009	9.739
R_{wp}	2.878	18.072
Goodness of fit	1.472	9.017
Z_M	0.08338(11)	0.08480(107)
α_r	1.073	1.055

A.2.2 PXRD data including Rietveld refinement

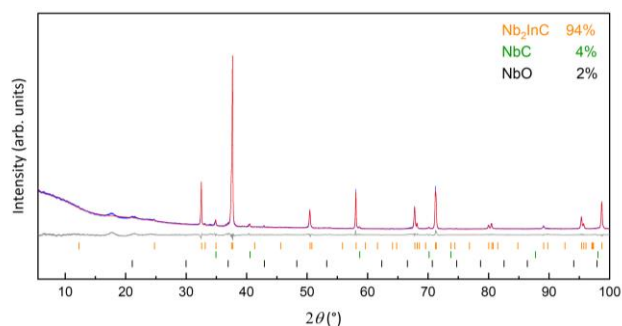


Figure A-14: X-ray powder pattern of Nb_2InC (blue) synthesized by flux synthesis with Rietveld fit (red) and difference curve (gray).

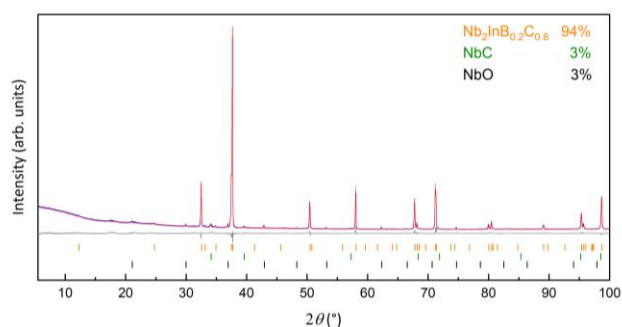


Figure A-15: X-ray powder pattern of $\text{Nb}_2\text{InB}_{0.2}\text{C}_{0.8}$ (blue) synthesized by flux synthesis with Rietveld fit (red) and difference curve (gray).

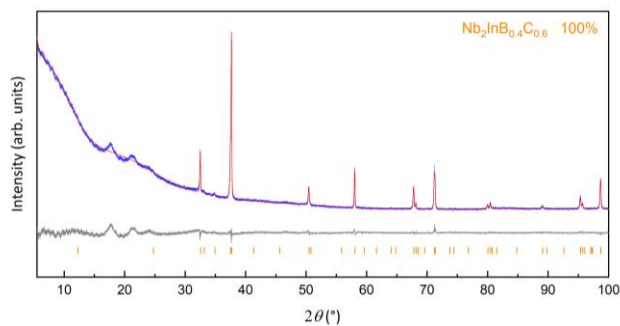


Figure A-16: X-ray powder pattern of Nb₂InB_{0.4}C_{0.6} (blue) synthesized by flux synthesis with Rietveld fit (red) and difference curve (gray).

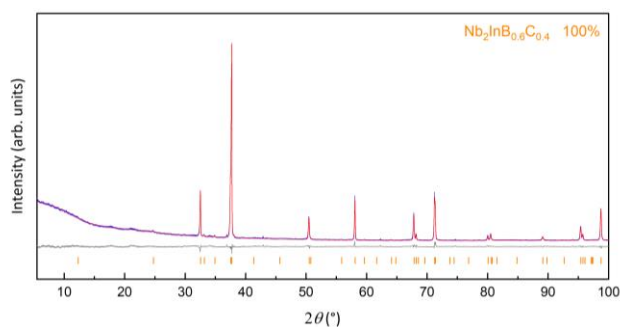


Figure A-17: X-ray powder pattern of Nb₂InB_{0.6}C_{0.4} (blue) synthesized by flux synthesis with Rietveld fit (red) and difference curve (gray).

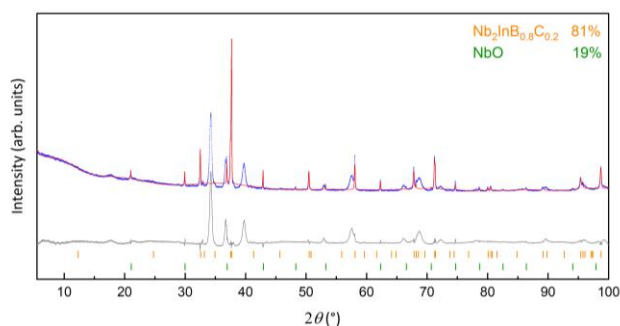


Figure A-18: X-ray powder pattern of Nb₂InB_{0.8}C_{0.2} (blue) synthesized by flux synthesis with Rietveld fit (red) and difference curve (gray).

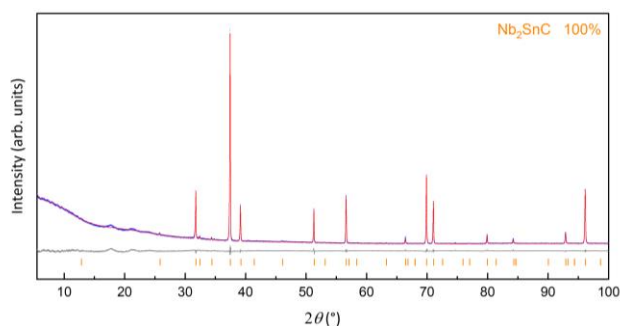


Figure A-19: X-ray powder pattern of Nb₂SnC (blue) synthesized by flux synthesis with Rietveld fit (red) and difference curve (gray).

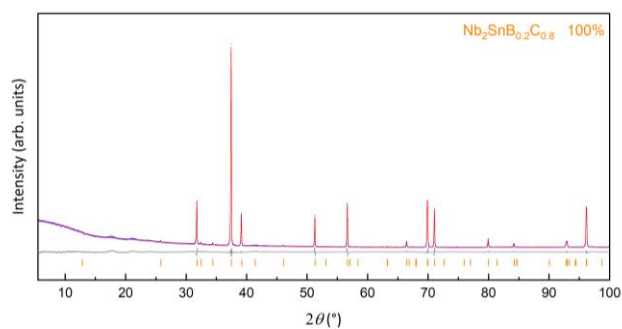


Figure A-20: X-ray powder pattern of $\text{Nb}_2\text{SnB}_{0.2}\text{C}_{0.8}$ (blue) synthesized by flux synthesis with Rietveld fit (red) and difference curve (gray).

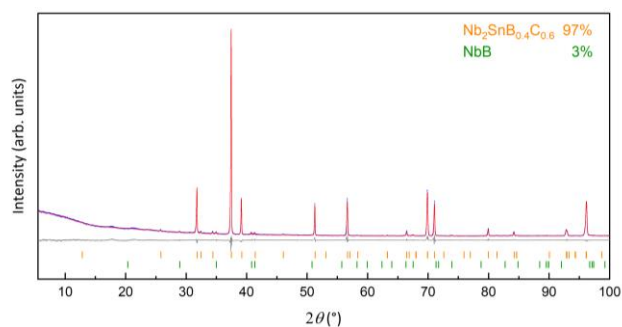


Figure A-21: X-ray powder pattern of $\text{Nb}_2\text{SnB}_{0.4}\text{C}_{0.6}$ (blue) synthesized by flux synthesis with Rietveld fit (red) and difference curve (gray).

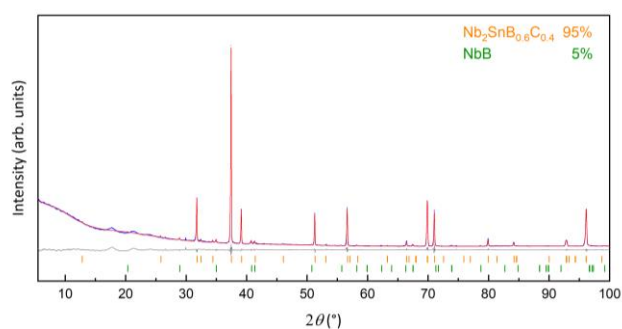


Figure A-22: X-ray powder pattern of $\text{Nb}_2\text{SnB}_{0.6}\text{C}_{0.4}$ (blue) synthesized by flux synthesis with Rietveld fit (red) and difference curve (gray).

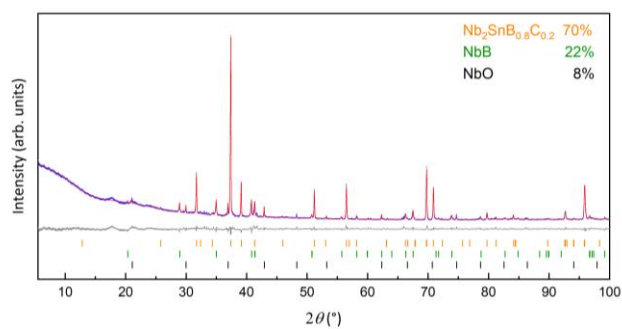


Figure A-23: X-ray powder pattern of $\text{Nb}_2\text{SnB}_{0.8}\text{C}_{0.2}$ (blue) synthesized by flux synthesis with Rietveld fit (red) and difference curve (gray).

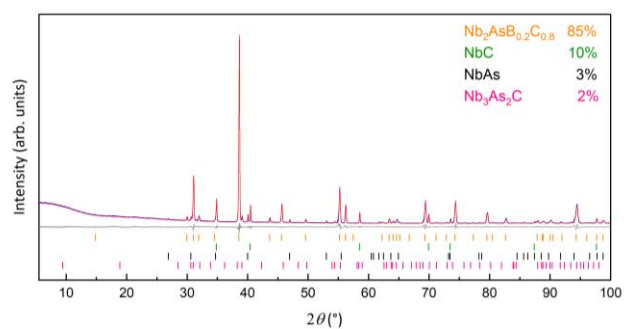


Figure A-24: X-ray powder pattern of $\text{Nb}_2\text{AsB}_{0.2}\text{C}_{0.8}$ (blue) with Rietveld fit (red) and difference curve (gray).

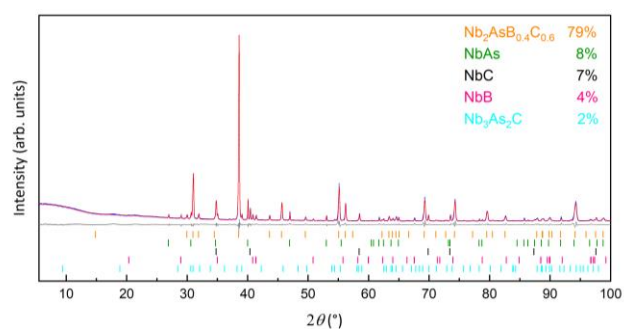


Figure A-25: X-ray powder pattern of $\text{Nb}_2\text{AsB}_{0.4}\text{C}_{0.6}$ (blue) with Rietveld fit (red) and difference curve (gray).

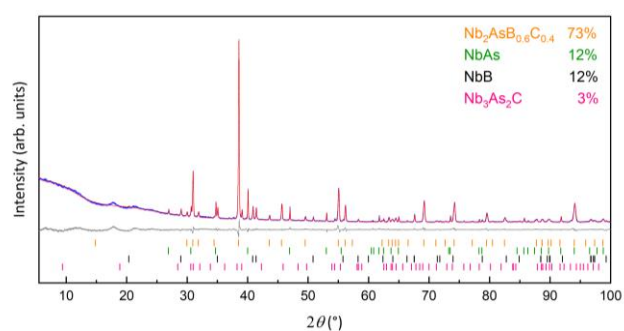


Figure A-26: X-ray powder pattern of $\text{Nb}_2\text{AsB}_{0.6}\text{C}_{0.4}$ (blue) with Rietveld fit (red) and difference curve (gray).

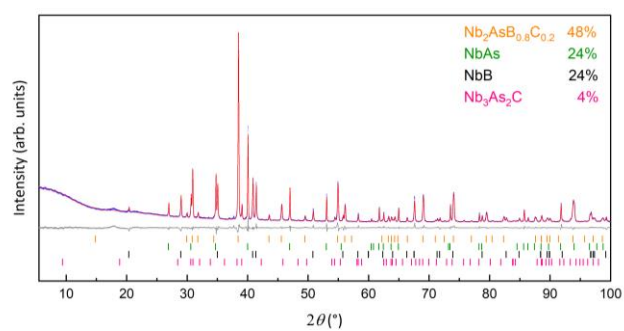


Figure A-27: X-ray powder pattern of $\text{Nb}_2\text{AsB}_{0.8}\text{C}_{0.2}$ (blue) with Rietveld fit (red) and difference curve (gray).

A. 3 Starting materials, crystallographic data and Rietveld refinement of $M_2A_xA'_{1-x}C$ ($M = V, Nb$; $A, A' = In, Ge, Sn, P, As, S$) and $(V_xNb_{1-x})_2SC$

Table A-5: Used elements for the syntheses of the solid solutions $M_2A_xA'_{1-x}C$ ($M = V, Nb$; $A, A' = In, Ge, Sn, P, As, S$) and $(V_xNb_{1-x})_2SC$.

element	Purity (%)	morphology	supplier
niobium	99.99	powder	Alfa Aesar
vanadium	99.5	powder	abcr
indium	99.99	powder	abcr
germanium	99.99	chips	VWR
tin	99.99	powder	Alfa Aesar
phosphorous	99.999	pieces	Chempur
arsenic	99.999	pieces	Alfa Aesar
sulfur	99.99	flakes	Sigma Aldrich
carbon	100	powder	ACROS Organics

Table A-6: Crystallographic data of V_2GeC , V_2PC , V_2AsC determined from PXRD data using Rietveld refinement.

Chemical formula	V_2GeC	V_2PC	V_2AsC
M (g·mol ⁻¹)	186.53	144.87	188.82
Crystal system,	hexagonal,	hexagonal,	hexagonal,
Space group	$P6_3/mmc$ (194)	$P6_3/mmc$ (194)	$P6_3/mmc$ (194)
T (K)	293	293	293
a (Å), c (Å)	2.9989(1), 12.2425(1)	3.0763(1), 10.9155(2)	3.1112(1), 11.3901(1)
V (Å ³)	95.353(1)	89.458(3)	95.479(1)
Z	2	2	2
Radiation type	Cu- $K_{\alpha 1}$, $\lambda = 1.54056$ Å	Cu- $K_{\alpha 1}$, $\lambda = 1.54056$ Å	Cu- $K_{\alpha 1}$, $\lambda = 1.54056$ Å
Diffractometer	Huber G670	Huber G670	Huber G670
Monochromator	Ge-111	Ge-111	Ge-111
R_p	2.199	2.041	2.123
R_{wp}	3.052	3.698	3.131
Goodness of fit	2.087	2.650	2.211
Z_M	0.08790(7)	0.09817(10)	0.09135(5)
α_r	1.120	1.148	1.189
p_d	1.139	1.266	1.221

Table A-7: Crystallographic data of Nb₂InC, Nb₂GeC, Nb₂SnC Nb₂PC, Nb₂AsC and Nb₂SC determined from PXRD data using Rietveld refinement.

Chemical formula	Nb ₂ InC	Nb ₂ GeC	Nb ₂ SnC
<i>M</i> (g·mol ⁻¹)	312.64	207.46	316.53
Crystal system,	hexagonal,	hexagonal,	hexagonal,
Space group	<i>P6₃/mmc</i> (194)	<i>P6₃/mmc</i> (194)	<i>P6₃/mmc</i> (194)
<i>T</i> (K)	293	293	293
<i>a</i> (Å), <i>c</i> (Å)	3.1690(1), 14.3517(1)	3.2325(1), 12.5913(1)	3.2433(1), 13.7742(1)
<i>V</i> (Å ³)	124.820(2)	113.937(2)	125.479(1)
<i>Z</i>	2	2	2
Radiation type	Cu-K _{α1} , λ = 1.54056 Å	Cu-K _{α1} , λ = 1.54056 Å	Cu-K _{α1} , λ = 1.54056 Å
Diffractionmeter	Huber G670	Huber G670	Huber G670
Monochromator	Ge-111	Ge-111	Ge-111
<i>R_p</i>	2.585	1.432	3.379
<i>R_{wp}</i>	3.541	1.940	5.243
Goodness of fit	2.164	1.211	3.290
<i>z_M</i>	0.08369(10)	0.09258(6)	0.08387(10)
<i>α_r</i>	1.068	1.115	1.127
<i>ρ_d</i>	1.054	1.187	1.097
Chemical formula	Nb ₂ PC	Nb ₂ AsC	Nb ₂ SC
<i>M</i> (g·mol ⁻¹)	228.80	272.75	229.89
Crystal system,	hexagonal,	hexagonal,	hexagonal,
Space group	<i>P6₃/mmc</i> (194)	<i>P6₃/mmc</i> (194)	<i>P6₃/mmc</i> (194)
<i>T</i> (K)	293	293	293
<i>a</i> (Å), <i>c</i> (Å)	3.2868(1), 11.5531(3)	3.3216(1), 11.9114(2)	3.2989(1), 11.5694(1)
<i>V</i> (Å ³)	108.086(5)	113.812(3)	109.036(2)
<i>Z</i>	2	2	2
Radiation type	Cu-K _{α1} , λ = 1.54056 Å	Cu-K _{α1} , λ = 1.54056 Å	Cu-K _{α1} , λ = 1.54056 Å
Diffractionmeter	Huber G670	Huber G670	Huber G670
Monochromator	Ge-111	Ge-111	Ge-111
<i>R_p</i>	1.948	1.847	2.293
<i>R_{wp}</i>	2.921	2.689	3.283
Goodness of fit	1.822	1.445	1.722
<i>z_M</i>	0.10029(10)	0.09483(1)	0.09716(6)
<i>α_r</i>	1.137	1.172	1.171
<i>ρ_d</i>	1.280	1.247	1.270

Table A-8: Crystallographic data of $V_2Ge_xP_{1-x}C$ ($x = 0.8, 0.5, 0.2$) and $V_2Ge_xAs_{1-x}C$ ($x = 0.8, 0.5, 0.2$), determined from PXRD data using Rietveld refinement.

Chemical formula	$V_2Ge_{0.8}P_{0.2}C$	$V_2Ge_{0.5}P_{0.5}C$	$V_2Ge_{0.2}P_{0.8}C$
M (g·mol ⁻¹)	178.17	165,68	153,19
Crystal system,	hexagonal,	hexagonal,	hexagonal,
Space group	$P6_3/mmc$ (194)	$P6_3/mmc$ (194)	$P6_3/mmc$ (194)
T (K)	293	293	293
a (Å), c (Å)	3.0060(1), 12.1936(3)	3.0343(1), 11.5928(1)	3.0718(1), 10.9877(2)
V (Å ³)	95.419(4)	92.434(2)	89.791(3)
Z	2	2	2
Radiation type	Cu- $K_{\alpha 1}$, $\lambda = 1.54056$ Å	Cu- $K_{\alpha 1}$, $\lambda = 1.54056$ Å	Cu- $K_{\alpha 1}$, $\lambda = 1.54056$ Å
Diffractionmeter	Huber G670	Huber G670	Huber G670
Monochromator	Ge-111	Ge-111	Ge-111
R_p	2.040	2.017	2.118
R_{wp}	3.269	2.710	3.058
Goodness of fit	2.273	1.843	2.116
Z_M	0.09960(14)	0.09394(9)	0.09191(13)
α_r	1.010	1.119	1.206
p_d	1.191	1.205	1.237
x	0.73(10)	0.50(10)	0.13(10)
Chemical formula	$V_2Ge_{0.8}As_{0.2}C$	$V_2Ge_{0.5}As_{0.5}C$	$V_2Ge_{0.2}As_{0.8}C$
M (g·mol ⁻¹)	186,96	187,66	188,35
Crystal system,	hexagonal,	hexagonal,	hexagonal,
Space group	$P6_3/mmc$ (194)	$P6_3/mmc$ (194)	$P6_3/mmc$ (194)
T (K)	293	293	293
a (Å), c (Å)	3.0188(1), 12.1115(1)	3.0602(1), 11.7840(1)	3.0922(1), 11.5282(2)
V (Å ³)	95.588(2)	95.573(2)	95.460(2)
Z	2	2	2
Radiation type	Cu- $K_{\alpha 1}$, $\lambda = 1.54056$ Å	Cu- $K_{\alpha 1}$, $\lambda = 1.54056$ Å	Cu- $K_{\alpha 1}$, $\lambda = 1.54056$ Å
Diffractionmeter	Huber G670	Huber G670	Huber G670
Monochromator	Ge-111	Ge-111	Ge-111
R_p	1.968	2.330	1.952
R_{wp}	2.600	3.010	2.520
Goodness of fit	1.779	1.971	1.662
Z_M	0.08921(9)	0.08995(1)	0.09093(10)
α_r	1.122	1.154	1.175
p_d	1.155	1.184	1.208

Table A-9: Crystallographic data of $V_2P_xAs_{1-x}C$ ($x = 0.8, 0.5, 0.2$) and $V_2P_xS_{1-x}C$ ($x = 0.9, 0.5, 0.4$) determined from PXRD data using Rietveld refinement.

Chemical formula	$V_2P_{0.8}As_{0.2}C$	$V_2P_{0.5}As_{0.5}C$	$V_2P_{0.2}As_{0.8}C$
M (g·mol ⁻¹)	153,65	166,84	180,02
Crystal system,	hexagonal,	hexagonal,	hexagonal,
Space group	$P6_3/mmc$ (194)	$P6_3/mmc$ (194)	$P6_3/mmc$ (194)
T (K)	293	293	293
a (Å), c (Å)	3.0855(1), 11.0371(2)	3.0897(1), 11.1001(1)	3.1071(1), 11.3339(1)
V (Å ³)	91.000(3)	91.769(2)	94.761(2)
Z	2	2	2
Radiation type	Cu- $K_{\alpha 1}$, $\lambda = 1.54056$ Å	Cu- $K_{\alpha 1}$, $\lambda = 1.54056$ Å	Cu- $K_{\alpha 1}$, $\lambda = 1.54056$ Å
Diffractionmeter	Huber G670	Huber G670	Huber G670
Monochromator	Ge-111	Ge-111	Ge-111
R_p	1.735	1.870	1.825
R_{wp}	2.315	2.465	2.388
Goodness of fit	1.575	1.671	1.603
z_M	0.09723(10)	0.09568(6)	0.09272(9)
α_r	1.150	1.162	1.178
p_d	1.258	1.249	1.229
x	0.72(10)	0.57(10)	0.17(10)
Chemical formula	$V_2P_{0.9}S_{0.1}C$	$V_2P_{0.5}S_{0.5}C$	$V_2P_{0.4}S_{0.6}C$
M (g·mol ⁻¹)	144,97	145,41	145,52
Crystal system,	hexagonal,	hexagonal,	hexagonal,
Space group	$P6_3/mmc$ (194)	$P6_3/mmc$ (194)	$P6_3/mmc$ (194)
T (K)	293	293	293
a (Å), c (Å)	3.0825(1), 10.8849(1)	3.0974(1), 10.8115(1)	3.1080(1), 10.7920(1)
V (Å ³)	89.570(2)	89.828(2)	90.278(2)
Z	2	2	2
Radiation type	Cu- $K_{\alpha 1}$, $\lambda = 1.54056$ Å	Cu- $K_{\alpha 1}$, $\lambda = 1.54056$ Å	Cu- $K_{\alpha 1}$, $\lambda = 1.54056$ Å
Diffractionmeter	Huber G670	Huber G670	Huber G670
Monochromator	Ge-111	Ge-111	Ge-111
R_p	1.460	1.269	1.440
R_{wp}	2.051	1.697	1.898
Goodness of fit	1.384	1.144	1.238
z_M	0.09795(6)	0.09762(8)	0.09614(7)
α_r	1.156	1.170	1.191
p_d	1.269	1.274	1.271

Table A-10: Crystallographic data of $V_2As_xS_{1-x}C$ ($x = 0.8, 0.5, 0.2$), $Nb_2In_xSn_{1-x}C$ ($x = 0.8, 0.5, 0.2$) determined from PXRD data using Rietveld refinement.

Chemical formula	$V_2As_{0.8}S_{0.2}C$	$V_2As_{0.5}S_{0.5}C$	$V_2As_{0.2}S_{0.8}C$
M (g·mol ⁻¹)	180,24	167,39	154,53
Crystal system,	hexagonal,	hexagonal,	hexagonal,
Space group	$P6_3/mmc$ (194)	$P6_3/mmc$ (194)	$P6_3/mmc$ (194)
T (K)	293	293	293
a (Å), c (Å)	3.1107(2), 11.3382(13)	3.1175(1), 11.1729(1)	3.1109(3), 11.3281(16)
V (Å ³)	95.015(24)	94.036(1)	94.943(20)
Z	2	2	2
Radiation type	Cu- $K_{\alpha 1}$, $\lambda = 1.54056$ Å	Cu- $K_{\alpha 1}$, $\lambda = 1.54056$ Å	Cu- $K_{\alpha 1}$, $\lambda = 1.54056$ Å
Diffractionmeter	Huber G670	Huber G670	Huber G670
Monochromator	Ge-111	Ge-111	Ge-111
R_p	59.619	1.493	2.092
R_{wp}	72.189	2.105	2.807
Goodness of fit	17.004	1.463	1.814
Z_M	0.09331(57)	0.09371(9)	0.07008(105)
α_r	1.172	1.185	1.477
p_d	1.231	1.243	1.145
x	0.75(10)	0.60(10)	1.00(10)
Chemical formula	$Nb_2In_{0.8}Sn_{0.2}C$	$Nb_2In_{0.5}Sn_{0.5}C$	$Nb_2In_{0.2}Sn_{0.8}C$
M (g·mol ⁻¹)	313.43	314.60	315.76
Crystal system,	hexagonal,	hexagonal,	hexagonal,
Space group	$P6_3/mmc$ (194)	$P6_3/mmc$ (194)	$P6_3/mmc$ (194)
T (K)	293	293	293
a (Å), c (Å)	3.1769(1), 14.3035(1)	3.2036(1), 14.0677(1)	3.2236(1), 13.9066(1)
V (Å ³)	125.019(2)	125.033(1)	125.152(2)
Z	2	2	2
Radiation type	Cu- $K_{\alpha 1}$, $\lambda = 1.54056$ Å	Cu- $K_{\alpha 1}$, $\lambda = 1.54056$ Å	Cu- $K_{\alpha 1}$, $\lambda = 1.54056$ Å
Diffractionmeter	Huber G670	Huber G670	Huber G670
Monochromator	Ge-111	Ge-111	Ge-111
R_p	2.058	2.585	1.999
R_{wp}	2.796	3.781	2.651
Goodness of fit	1.295	2.243	1.231
Z_M	0.08370(13)	0.08386(8)	0.08393(18)
α_r	1.073	1.097	1.111
p_d	1.058	1.076	1.087

Table A-11: Crystallographic data of $\text{Nb}_2\text{Ge}_x\text{As}_{1-x}\text{C}$ ($x = 0.8, 0.5, 0.2$) and $\text{Nb}_2\text{P}_x\text{As}_{1-x}\text{C}$ ($x = 0.8, 0.5, 0.2$) determined from PXRD data using Rietveld refinement.

Chemical formula	$\text{Nb}_2\text{Ge}_{0.8}\text{As}_{0.2}\text{C}$	$\text{Nb}_2\text{Ge}_{0.5}\text{As}_{0.5}\text{C}$	$\text{Nb}_2\text{Ge}_{0.2}\text{As}_{0.8}\text{C}$
M ($\text{g}\cdot\text{mol}^{-1}$)	270.90	271.60	272.29
Crystal system,	hexagonal,	hexagonal,	hexagonal,
Space group	$P6_3/mmc$ (194)	$P6_3/mmc$ (194)	$P6_3/mmc$ (194)
T (K)	293	293	293
a (\AA), c (\AA)	3.2632(1), 12.3150(1)	3.2934(1), 12.1004(1)	3.3145(1), 11.9432(1)
V (\AA^3)	113.569(1)	113.665(2)	113.627(1)
Z	2	2	2
Radiation type	$\text{Cu-K}\alpha_1$, $\lambda = 1.54056 \text{ \AA}$	$\text{Cu-K}\alpha_1$, $\lambda = 1.54056 \text{ \AA}$	$\text{Cu-K}\alpha_1$, $\lambda = 1.54056 \text{ \AA}$
Diffractometer	Huber G670	Huber G670	Huber G670
Monochromator	Ge-111	Ge-111	Ge-111
R_p	2.776	1.940	2.643
R_{wp}	3.761	2.926	3.647
Goodness of fit	2.016	1.805	2.249
z_M	0.09407(5)	0.09480(5)	0.09459(4)
α_r	1.130	1.148	1.170
ρ_d	1.213	1.232	1.243
Chemical formula	$\text{Nb}_2\text{P}_{0.8}\text{As}_{0.2}\text{C}$	$\text{Nb}_2\text{P}_{0.5}\text{As}_{0.5}\text{C}$	$\text{Nb}_2\text{P}_{0.2}\text{As}_{0.8}\text{C}$
M ($\text{g}\cdot\text{mol}^{-1}$)	237.59	250.78	263.96
Crystal system,	hexagonal,	hexagonal,	hexagonal,
Space group	$P6_3/mmc$ (194)	$P6_3/mmc$ (194)	$P6_3/mmc$ (194)
T (K)	293	293	293
a (\AA), c (\AA)	3.2980(1), 11.6474(3)	3.3066(1), 11.7762(1)	3.3133(1), 11.8594(1)
V (\AA^3)	109.711(4)	111.509(2)	112.751(1)
Z	2	2	2
Radiation type	$\text{Cu-K}\alpha_1$, $\lambda = 1.54056 \text{ \AA}$	$\text{Cu-K}\alpha_1$, $\lambda = 1.54056 \text{ \AA}$	$\text{Cu-K}\alpha_1$, $\lambda = 1.54056 \text{ \AA}$
Diffractometer	Huber G670	Huber G670	Huber G670
Monochromator	Ge-111	Ge-111	Ge-111
R_p	2.966	4.444	2.323
R_{wp}	4.320	6.689	3.308
Goodness of fit	2.639	3.723	1.553
z_M	0.09898(13)	0.09687(6)	0.09548(5)
α_r	1.145	1.158	1.167
ρ_d	1.272	1.259	1.251
x	0.70(10)	0.38(10)	0.19(10)

Table A-12: Crystallographic data of Nb₂As_xS_{1-x}C (x = 0.9, 0.8, 0.7, 0.6, 0.5, 0.4) determined from PXRD data using Rietveld refinement.

Chemical formula	Nb ₂ As _{0.9} S _{0.1} C	Nb ₂ As _{0.8} S _{0.2} C	Nb ₂ As _{0.7} S _{0.3} C
<i>M</i> (g·mol ⁻¹)	268.47	264.18	259.90
Crystal system,	hexagonal,	hexagonal,	hexagonal,
Space group	<i>P6₃/mmc</i> (194)	<i>P6₃/mmc</i> (194)	<i>P6₃/mmc</i> (194)
<i>T</i> (K)	293	293	293
<i>a</i> (Å), <i>c</i> (Å)	3.3143(1), 11.8461(3)	3.3157(1), 11.8272(1)	3.3165(1), 11.7884(1)
<i>V</i> (Å ³)	112.690(4)	112.608(1)	112.293(2)
<i>Z</i>	2	2	2
Radiation type	Cu- <i>K</i> _{α1} , λ = 1.54056 Å	Cu- <i>K</i> _{α1} , λ = 1.54056 Å	Cu- <i>K</i> _{α1} , λ = 1.54056 Å
Diffractionmeter	Huber G670	Huber G670	Huber G670
Monochromator	Ge-111	Ge-111	Ge-111
<i>R_p</i>	5.416	3.052	2.025
<i>R_{wp}</i>	9.679	4.324	2.773
Goodness of fit	6.175	2.762	1.322
<i>Z_M</i>	0.09654(14)	0.09501(3)	0.09548(6)
<i>α_r</i>	1.157	1.175	1.174
<i>ρ_d</i>	1.255	1.251	1.255
<i>x</i>	0.93(10)	0.81(10)	0.73(10)
Chemical formula	Nb ₂ As _{0.6} S _{0.4} C	Nb ₂ As _{0.5} S _{0.5} C	Nb ₂ As _{0.4} S _{0.6} C
<i>M</i> (g·mol ⁻¹)	255.61	251.33	247.04
Crystal system,	hexagonal,	hexagonal,	hexagonal,
Space group	<i>P6₃/mmc</i> (194)	<i>P6₃/mmc</i> (194)	<i>P6₃/mmc</i> (194)
<i>T</i> (K)	293	293	293
<i>a</i> (Å), <i>c</i> (Å)	3.3167(1), 11.7492(1)	3.3137(1), 11.7169(1)	3.3144(1), 11.6913(2)
<i>V</i> (Å ³)	111.931(1)	111.419(1)	111.224(3)
<i>Z</i>	2	2	2
Radiation type	Cu- <i>K</i> _{α1} , λ = 1.54056 Å	Cu- <i>K</i> _{α1} , λ = 1.54056 Å	Cu- <i>K</i> _{α1} , λ = 1.54056 Å
Diffractionmeter	Huber G670	Huber G670	Huber G670
Monochromator	Ge-111	Ge-111	Ge-111
<i>R_p</i>	2.140	2.439	1.962
<i>R_{wp}</i>	2.992	3.494	2.648
Goodness of fit	1.834	2.203	1.260
<i>Z_M</i>	0.09561(4)	0.09562(3)	0.09648(7)
<i>α_r</i>	1.176	1.178	1.171
<i>ρ_d</i>	1.257	1.258	1.263
<i>x</i>	0.62(10)	0.57(10)	0.44(10)

Table A-13: Crystallographic data of $\text{Nb}_2\text{As}_x\text{S}_{1-x}\text{C}$ ($x = 0.3, 0.2, 0.1$) and $(\text{V}_x\text{Nb}_{1-x})_2\text{SC}$ ($x = 0.05, 0.1, 0.15$) determined from PXRD data using Rietveld refinement.

Chemical formula	$\text{Nb}_2\text{As}_{0.3}\text{S}_{0.7}\text{C}$	$\text{Nb}_2\text{As}_{0.2}\text{S}_{0.8}\text{C}$	$\text{Nb}_2\text{As}_{0.1}\text{S}_{0.9}\text{C}$
M ($\text{g}\cdot\text{mol}^{-1}$)	242.76	238.47	234.19
Crystal system,	hexagonal,	hexagonal,	hexagonal,
Space group	$P6_3/mmc$ (194)	$P6_3/mmc$ (194)	$P6_3/mmc$ (194)
T (K)	293	293	293
a (\AA), c (\AA)	3.3082(1), 11.6488(1)	3.3108(1), 11.6431(5)	3.2948(1), 11.5632(1)
V (\AA^3)	110.409(1)	110.525(7)	108.706(2)
Z	2	2	2
Radiation type	$\text{Cu-}K_{\alpha 1}$, $\lambda = 1.54056 \text{ \AA}$	$\text{Cu-}K_{\alpha 1}$, $\lambda = 1.54056 \text{ \AA}$	$\text{Cu-}K_{\alpha 1}$, $\lambda = 1.54056 \text{ \AA}$
Diffractionmeter	Huber G670	Huber G670	Huber G670
Monochromator	Ge-111	Ge-111	Ge-111
R_p	2.814	2.828	3.432
R_{wp}	4.296	3.732	4.863
Goodness of fit	2.735	2.359	3.101
z_M	0.09585(3)	0.09602(4)	0.09647(3)
α_r	1.179	1.179	1.177
p_d	1.262	1.264	1.266
x	0.34(10)	0.26(10)	0.13(10)
Chemical formula	$(\text{V}_{0.05}\text{Nb}_{0.95})_2\text{SC}$	$(\text{V}_{0.1}\text{Nb}_{0.9})_2\text{SC}$	$(\text{V}_{0.15}\text{Nb}_{0.85})_2\text{SC}$
M ($\text{g}\cdot\text{mol}^{-1}$)	225.7	221.51	217.31
Crystal system,	hexagonal,	hexagonal,	hexagonal,
Space group	$P6_3/mmc$ (194)	$P6_3/mmc$ (194)	$P6_3/mmc$ (194)
T (K)	293	293	293
a (\AA), c (\AA)	3.2959(1), 11.5524(2)	3.2867(1), 11.4994(1)	3.2829(12), 11.4677(62)
V (\AA^3)	108.678(2)	107.577(1)	107.032(97)
Z	2	2	2
Radiation type	$\text{Cu-}K_{\alpha 1}$, $\lambda = 1.54056 \text{ \AA}$	$\text{Cu-}K_{\alpha 1}$, $\lambda = 1.54056 \text{ \AA}$	$\text{Cu-}K_{\alpha 1}$, $\lambda = 1.54056 \text{ \AA}$
Diffractionmeter	Huber G670	Huber G670	Huber G670
Monochromator	Ge-111	Ge-111	Ge-111
R_p	1.536	1.965	1.679
R_{wp}	2.195	2.733	2.148
Goodness of fit	0.934	1.175	0.924
z_M	0.09567(11)	0.09608(5)	0.09666(12)
α_r	1.186	1.184	1.179
p_d	1.264	1.267	1.270
x	0.03(10)	0.11(10)	0.15(10)

Table A-14: Crystallographic data of $(V_xNb_{1-x})_2SC$ ($x = 0.2, 0.25, 0.3, 0.35, 0.4, 0.45$) determined from PXRD data using Rietveld refinement.

Chemical formula	$(V_{0.2}Nb_{0.8})_2SC$	$(V_{0.25}Nb_{0.75})_2SC$	$(V_{0.3}Nb_{0.7})_2SC$
M (g·mol ⁻¹)	213.11	208.92	204.72
Crystal system,	hexagonal,	hexagonal,	hexagonal,
Space group	$P6_3/mmc$ (194)	$P6_3/mmc$ (194)	$P6_3/mmc$ (194)
T (K)	293	293	293
a (Å), c (Å)	3.2815(1), 11.4612(3)	3.2683(1), 11.3925(3)	3.2599(1), 11.3503(3)
V (Å ³)	106.884(4)	105.386(3)	104.460(4)
Z	2	2	2
Radiation type	Cu- $K_{\alpha 1}$, $\lambda = 1.54056$ Å	Cu- $K_{\alpha 1}$, $\lambda = 1.54056$ Å	Cu- $K_{\alpha 1}$, $\lambda = 1.54056$ Å
Diffractionmeter	Huber G670	Huber G670	Huber G670
Monochromator	Ge-111	Ge-111	Ge-111
R_p	1.619	1.454	1.925
R_{wp}	2.073	1.924	2.498
Goodness of fit	0.893	0.823	1.088
Z_M	0.09645(11)	0.09564(6)	0.09596(10)
α_r	1.182	1.192	1.190
p_d	1.269	1.267	1.269
x	0.18(10)	0.23(10)	0.30(10)
Chemical formula	$(V_{0.35}Nb_{0.65})_2SC$	$(V_{0.4}Nb_{0.6})_2SC$	$(V_{0.45}Nb_{0.55})_2SC$
M (g·mol ⁻¹)	200.52	196.32	192.13
Crystal system,	hexagonal,	hexagonal,	hexagonal,
Space group	$P6_3/mmc$ (194)	$P6_3/mmc$ (194)	$P6_3/mmc$ (194)
T (K)	293	293	293
a (Å), c (Å)	3.2618(1), 11.3524(5)	3.2452(1), 11.2733(2)	3.2332(3), 11.1941(9)
V (Å ³)	104.598(6)	102.816(3)	101.340(22)
Z	2	2	2
Radiation type	Cu- $K_{\alpha 1}$, $\lambda = 1.54056$ Å	Cu- $K_{\alpha 1}$, $\lambda = 1.54056$ Å	Cu- $K_{\alpha 1}$, $\lambda = 1.54056$ Å
Diffractionmeter	Huber G670	Huber G670	Huber G670
Monochromator	Ge-111	Ge-111	Ge-111
R_p	1.886	1.804	1.827
R_{wp}	2.473	2.308	2.357
Goodness of fit	1.072	0.996	1.013
Z_M	0.09669(8)	0.09643(8)	0.09624(7)
α_r	1.183	1.187	1.193
p_d	1.272	1.272	1.274
x	0.34(10)	0.40(10)	0.44(10)

Table A-15: Crystallographic data of $(V_xNb_{1-x})_2SC$ ($x = 0.5$) determined from PXRD data using Rietveld refinement.

Chemical formula	$(V_{0.5}Nb_{0.5})_2SC$
M ($\text{g}\cdot\text{mol}^{-1}$)	187.93
Crystal system,	hexagonal,
Space group	$P6_3/mmc$ (194)
T (K)	293
a (\AA), c (\AA)	3.2344(1), 11.2144(2)
V (\AA^3)	101.599(2)
Z	2
Radiation type	$\text{Cu-K}\alpha_1$, $\lambda = 1.54056 \text{ \AA}$
Diffractometer	Huber G670
Monochromator	Ge-111
R_p	1.622
R_{wp}	2.100
Goodness of fit	0.920
Z_M	0.09638(6)
α_r	1.190
ρ_d	1.273
x	0.48(10)

A.3.1 PXRD data including Rietveld refinement

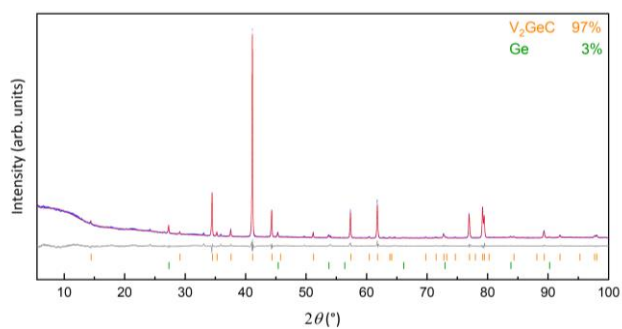


Figure A-28: X-ray powder pattern of V_2GeC (blue) with Rietveld fit (red) and difference curve (gray).

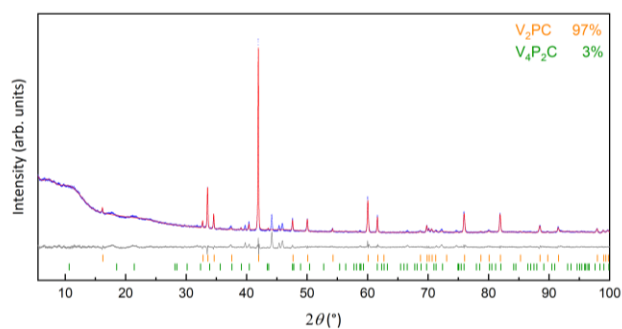


Figure A-29: X-ray powder pattern of V_2PC (blue) with Rietveld fit (red) and difference curve (gray).

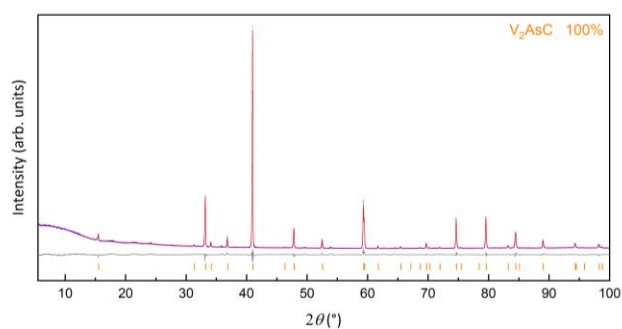


Figure A-30: X-ray powder pattern of V_2AsC (blue) with Rietveld fit (red) and difference curve (gray).

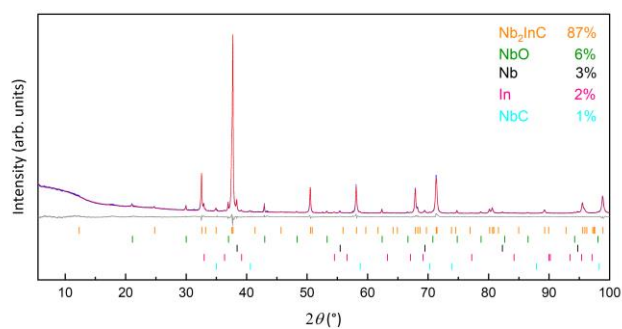


Figure A-31: X-ray powder pattern of Nb_2InC (blue) with Rietveld fit (red) and difference curve (gray).

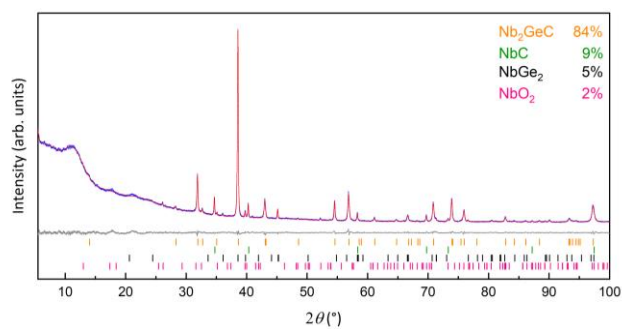


Figure A-32: X-ray powder pattern of Nb_2GeC (blue) with Rietveld fit (red) and difference curve (gray).

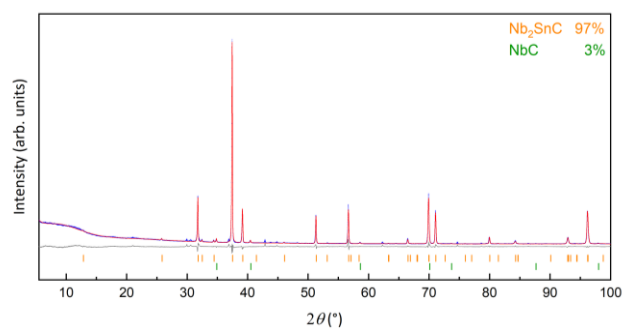


Figure A-33: X-ray powder pattern of Nb₂SnC (blue) with Rietveld fit (red) and difference curve (gray).

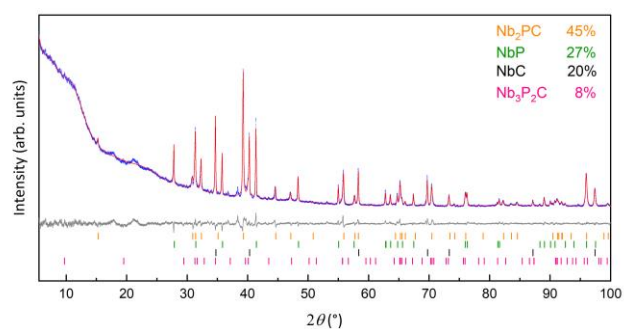


Figure A-34: X-ray powder pattern of Nb₂PC (blue) with Rietveld fit (red) and difference curve (gray).

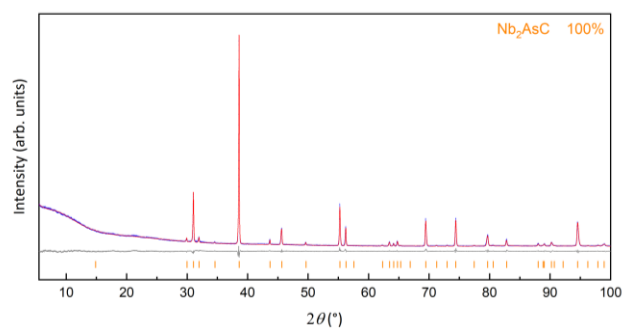


Figure A-35: X-ray powder pattern of Nb₂AsC (blue) with Rietveld fit (red) and difference curve (gray).

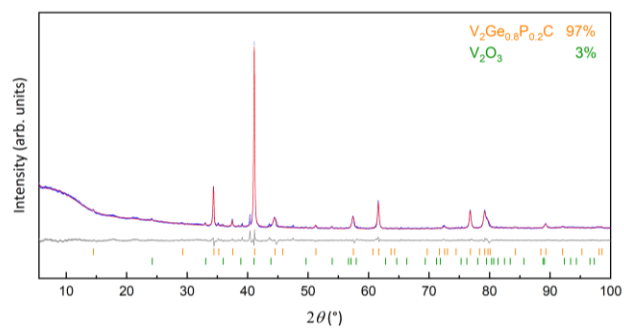


Figure A-36: X-ray powder pattern of V₂Ge_{0.8}P_{0.2}C (blue) with Rietveld fit (red) and difference curve (gray).

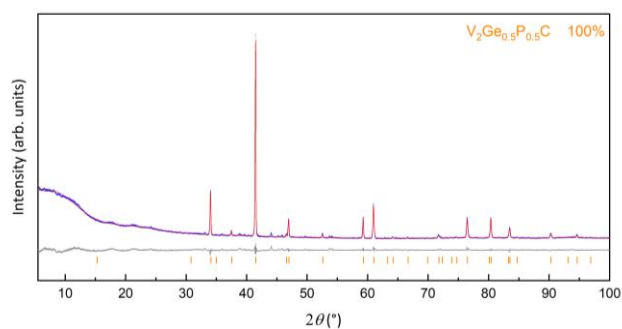


Figure A-37: X-ray powder pattern of $V_2Ge_{0.5}P_{0.5}C$ (blue) with Rietveld fit (red) and difference curve (gray).

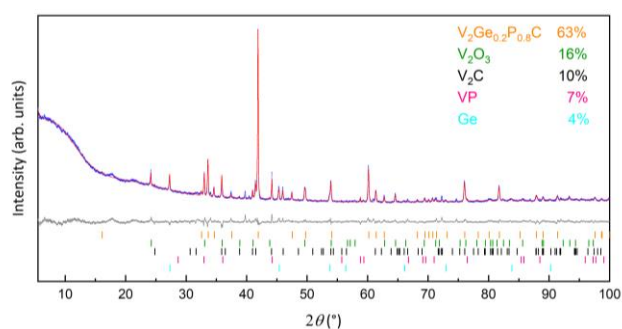


Figure A-38: X-ray powder pattern of $V_2Ge_{0.2}P_{0.8}C$ (blue) with Rietveld fit (red) and difference curve (gray).

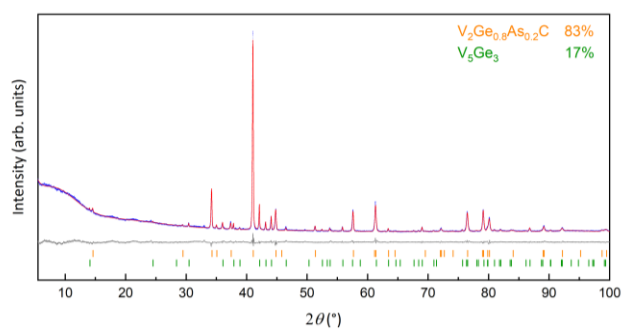


Figure A-39: X-ray powder pattern of $V_2Ge_{0.8}As_{0.2}C$ (blue) with Rietveld fit (red) and difference curve (gray).

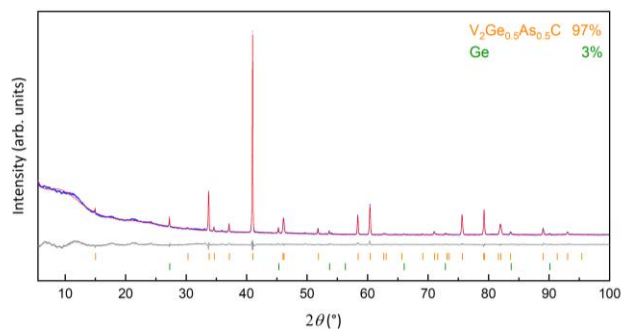


Figure A-40: X-ray powder pattern of $V_2Ge_{0.5}As_{0.5}C$ (blue) with Rietveld fit (red) and difference curve (gray).

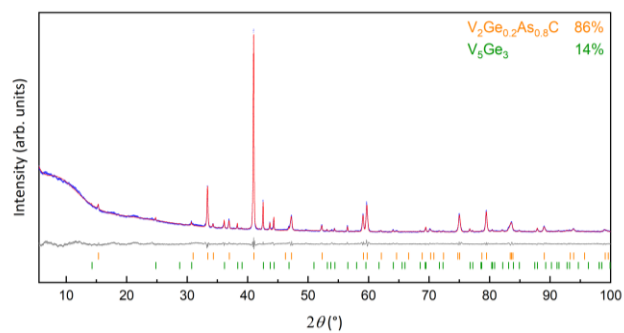


Figure A-41: X-ray powder pattern of $V_2Ge_{0.2}As_{0.8}C$ (blue) with Rietveld fit (red) and difference curve (gray).

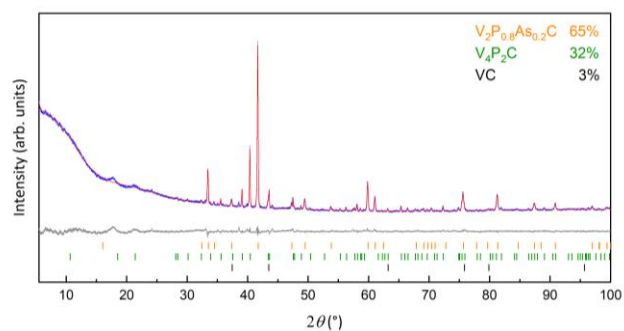


Figure A-42: X-ray powder pattern of $V_2P_{0.8}As_{0.2}C$ (blue) with Rietveld fit (red) and difference curve (gray).

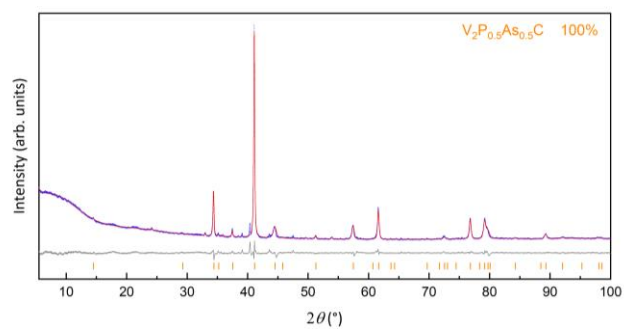


Figure A-43: X-ray powder pattern of $V_2P_{0.5}As_{0.5}C$ (blue) with Rietveld fit (red) and difference curve (gray).

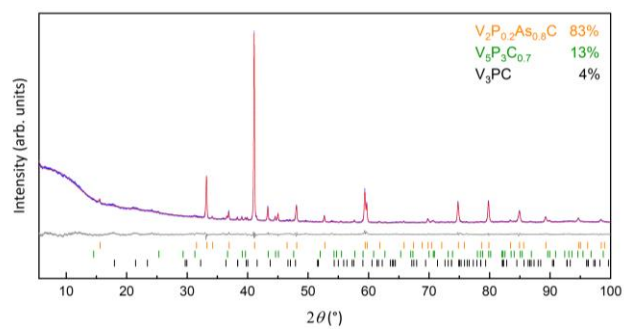


Figure A-44: X-ray powder pattern of $V_2P_{0.2}As_{0.8}C$ (blue) with Rietveld fit (red) and difference curve (gray).

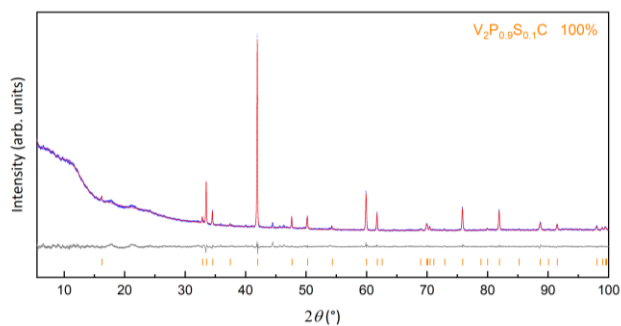


Figure A-45: X-ray powder pattern of $V_2P_{0.9}S_{0.1}C$ (blue) with Rietveld fit (red) and difference curve (gray).

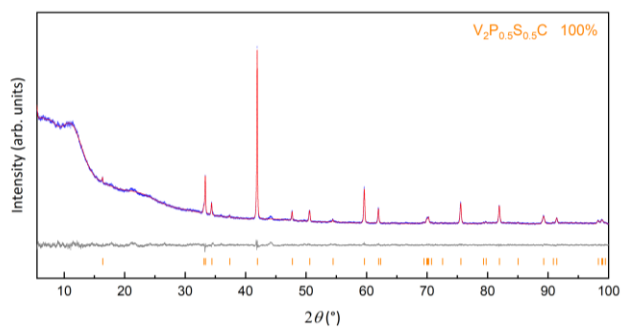


Figure A-46: X-ray powder pattern of $V_2P_{0.5}S_{0.5}C$ (blue) with Rietveld fit (red) and difference curve (gray).

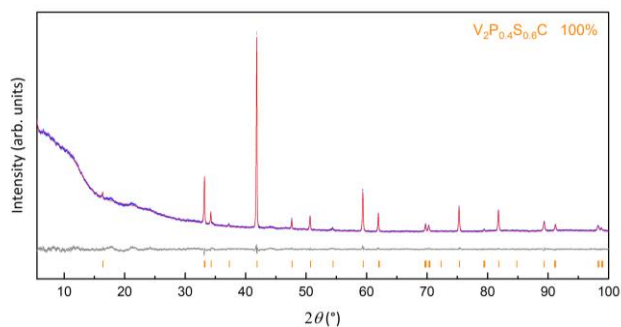


Figure A-47: X-ray powder pattern of $V_2P_{0.4}S_{0.6}C$ (blue) with Rietveld fit (red) and difference curve (gray).

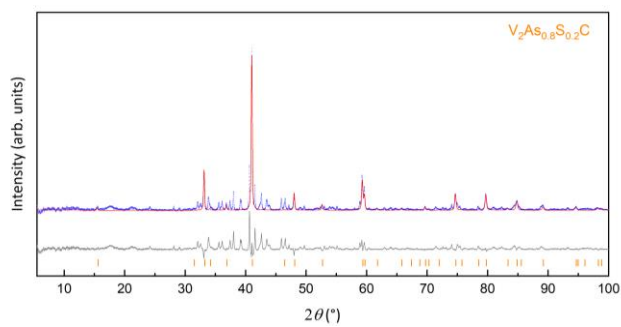


Figure A-48: X-ray powder pattern of $V_2As_{0.8}S_{0.2}C$ (blue) with Rietveld fit (red) and difference curve (gray).

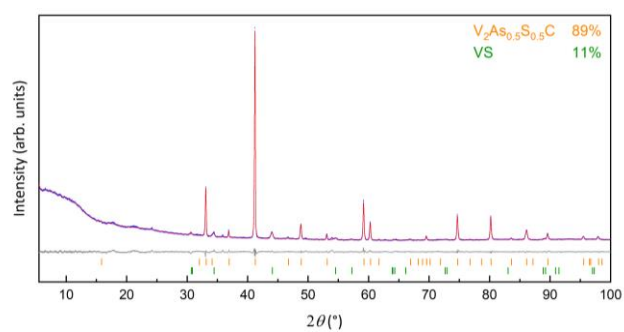


Figure A-49: X-ray powder pattern of $V_2As_{0.5}S_{0.5}C$ (blue) with Rietveld fit (red) and difference curve (gray).

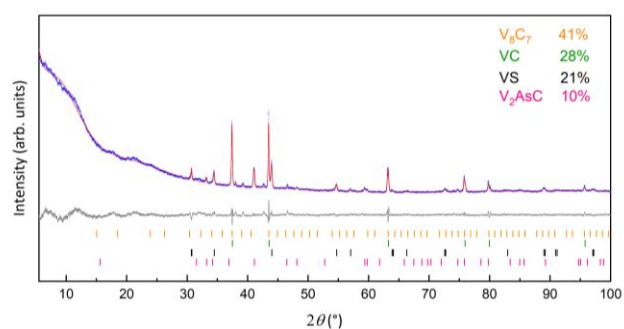


Figure A-50: X-ray powder pattern of $V_2As_{0.2}S_{0.8}C$ (blue) with Rietveld fit (red) and difference curve (gray).

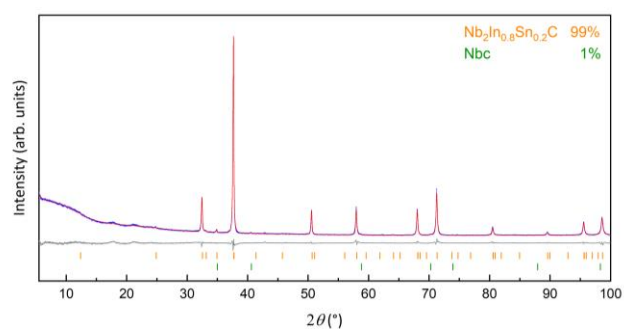


Figure A-51: X-ray powder pattern of $Nb_2In_{0.8}Sn_{0.2}C$ (blue) with Rietveld fit (red) and difference curve (gray).

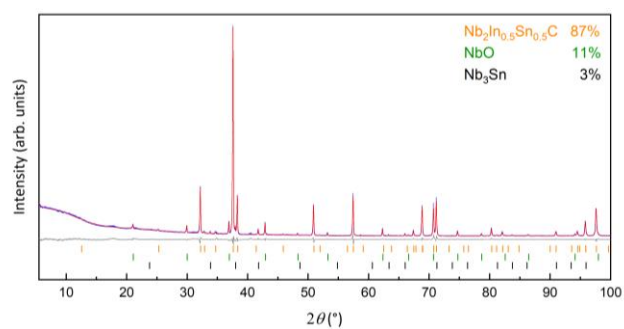


Figure A-52: X-ray powder pattern of $Nb_2In_{0.5}Sn_{0.5}C$ (blue) with Rietveld fit (red) and difference curve (gray).

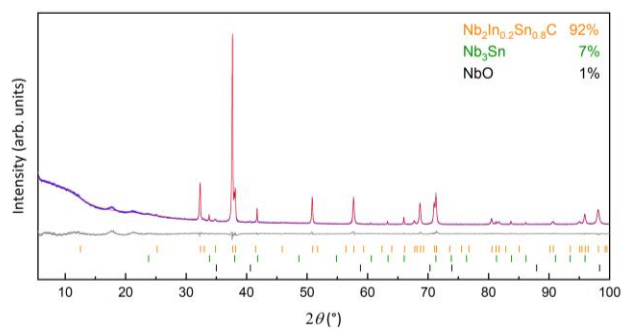


Figure A-53: X-ray powder pattern of $\text{Nb}_2\text{In}_{0.2}\text{Sn}_{0.8}\text{C}$ (blue) with Rietveld fit (red) and difference curve (gray).

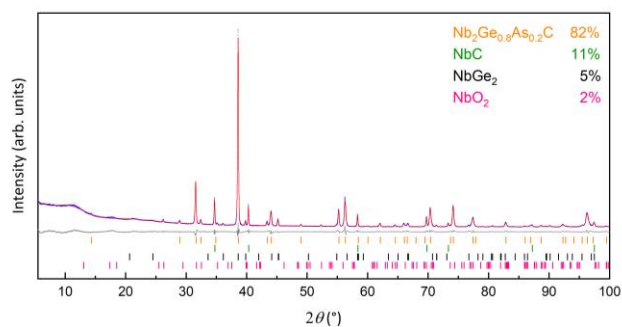


Figure A-54: X-ray powder pattern of $\text{Nb}_2\text{Ge}_{0.8}\text{As}_{0.2}\text{C}$ (blue) with Rietveld fit (red) and difference curve (gray).

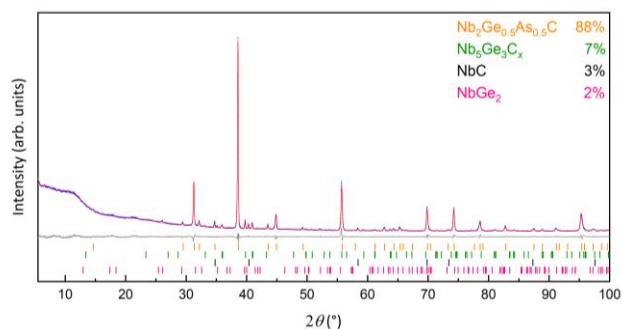


Figure A-55: X-ray powder pattern of $\text{Nb}_2\text{Ge}_{0.5}\text{As}_{0.5}\text{C}$ (blue) with Rietveld fit (red) and difference curve (gray).

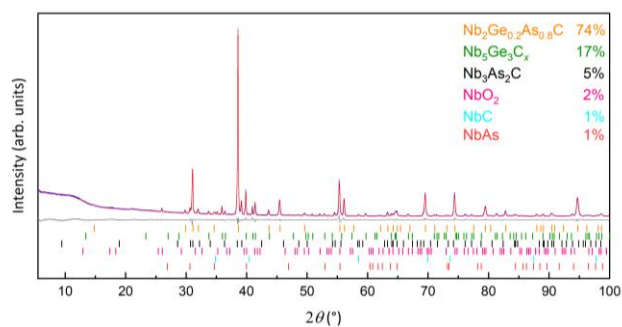


Figure A-56: X-ray powder pattern of $\text{Nb}_2\text{Ge}_{0.2}\text{As}_{0.8}\text{C}$ (blue) with Rietveld fit (red) and difference curve (gray).

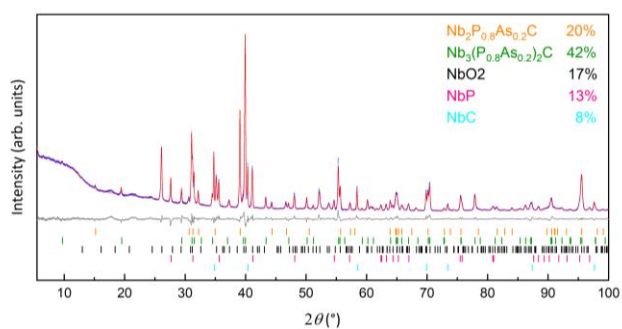


Figure A-57: X-ray powder pattern of $\text{Nb}_2\text{P}_{0.8}\text{As}_{0.2}\text{C}$ (blue) with Rietveld fit (red) and difference curve (gray).

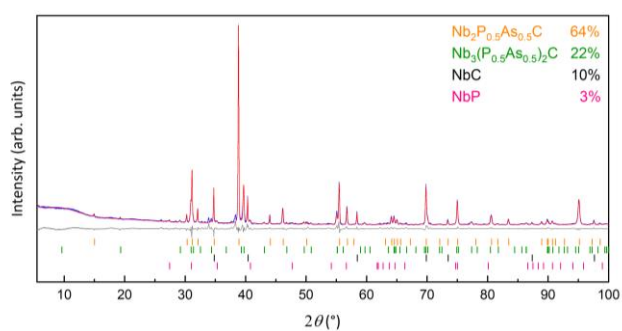


Figure A-58: X-ray powder pattern of $\text{Nb}_2\text{P}_{0.5}\text{As}_{0.5}\text{C}$ (blue) with Rietveld fit (red) and difference curve (gray).

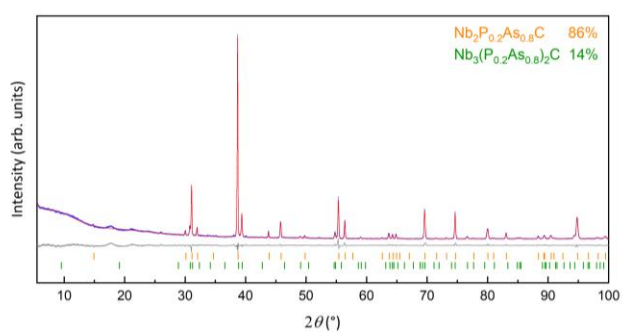


Figure A-59: X-ray powder pattern of $\text{Nb}_2\text{P}_{0.2}\text{As}_{0.8}\text{C}$ (blue) with Rietveld fit (red) and difference curve (gray).

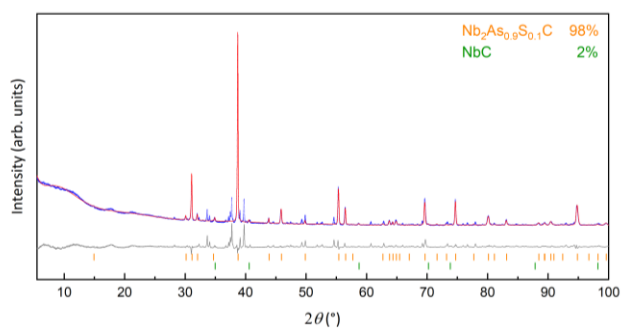


Figure A-60: X-ray powder pattern of $\text{Nb}_2\text{As}_{0.9}\text{S}_{0.1}\text{C}$ (blue) with Rietveld fit (red) and difference curve (gray).

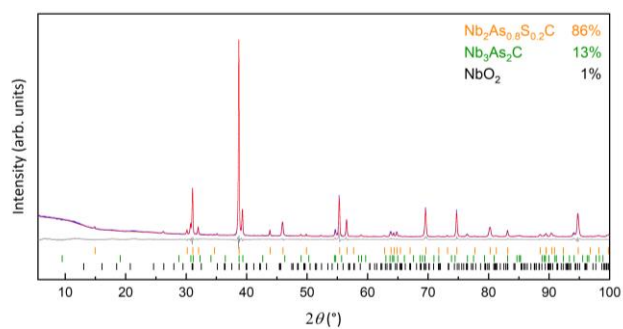


Figure A-61: X-ray powder pattern of $\text{Nb}_2\text{As}_{0.8}\text{S}_{0.2}\text{C}$ (blue) with Rietveld fit (red) and difference curve (gray).

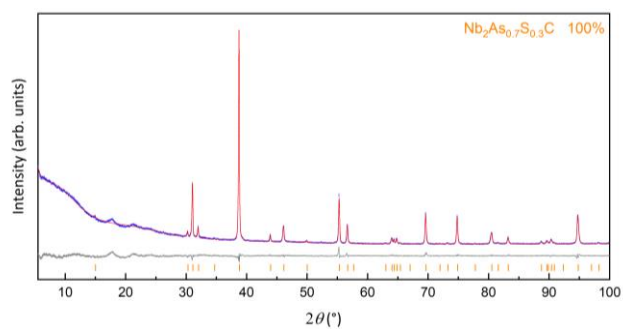


Figure A-62: X-ray powder pattern of $\text{Nb}_2\text{As}_{0.7}\text{S}_{0.3}\text{C}$ (blue) with Rietveld fit (red) and difference curve (gray).

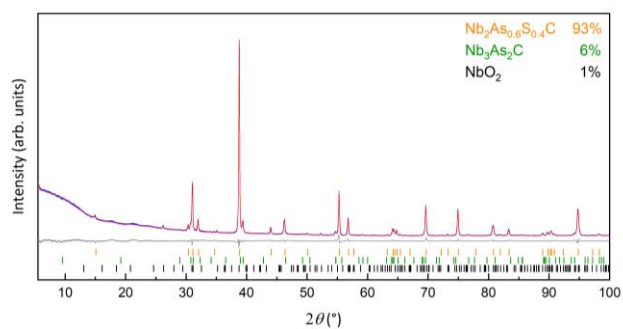


Figure A-63: X-ray powder pattern of $\text{Nb}_2\text{As}_{0.6}\text{S}_{0.4}\text{C}$ (blue) with Rietveld fit (red) and difference curve (gray).

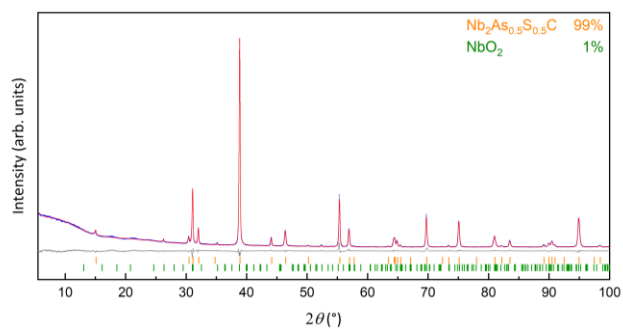


Figure A-64: X-ray powder pattern of $\text{Nb}_2\text{As}_{0.5}\text{S}_{0.5}\text{C}$ (blue) with Rietveld fit (red) and difference curve (gray).

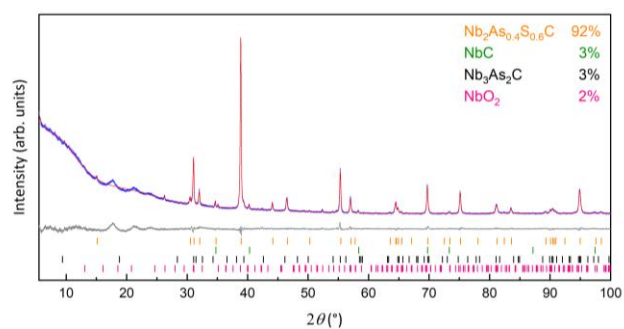


Figure A-65: X-ray powder pattern of $\text{Nb}_2\text{As}_{0.4}\text{S}_{0.6}\text{C}$ (blue) with Rietveld fit (red) and difference curve (gray).

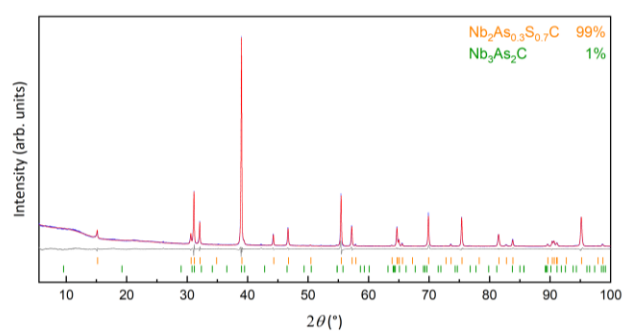


Figure A-66: X-ray powder pattern of $\text{Nb}_2\text{As}_{0.3}\text{S}_{0.7}\text{C}$ (blue) with Rietveld fit (red) and difference curve (gray).

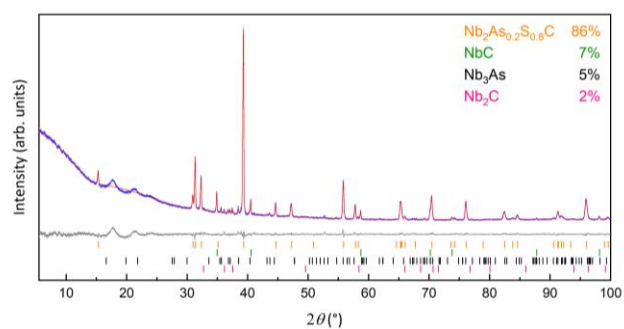


Figure A-67: X-ray powder pattern of $\text{Nb}_2\text{As}_{0.2}\text{S}_{0.8}\text{C}$ (blue) with Rietveld fit (red) and difference curve (gray).

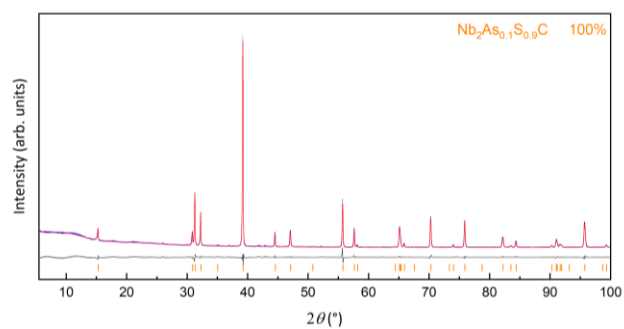


Figure A-68: X-ray powder pattern of $\text{Nb}_2\text{As}_{0.1}\text{S}_{0.9}\text{C}$ (blue) with Rietveld fit (red) and difference curve (gray).

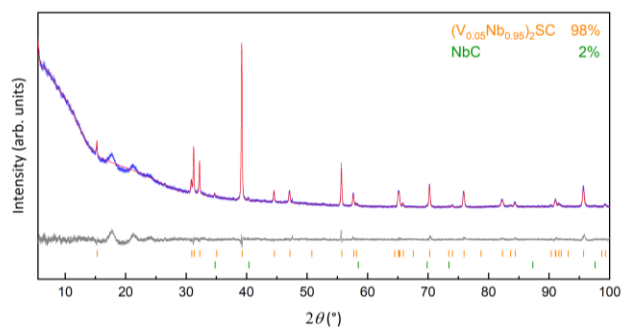


Figure A-69: X-ray powder pattern of $(V_{0.05}Nb_{0.95})_2SC$ (blue) with Rietveld fit (red) and difference curve (gray).

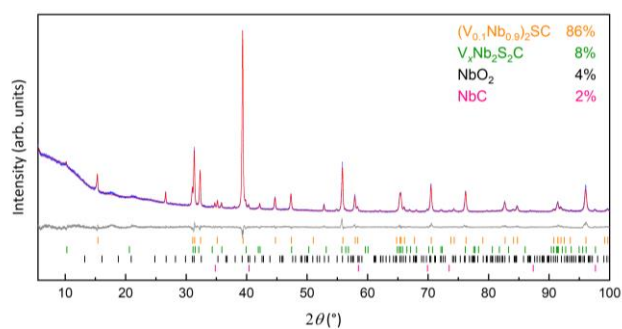


Figure A-70: X-ray powder pattern of $(V_{0.1}Nb_{0.9})_2SC$ (blue) with Rietveld fit (red) and difference curve (gray).

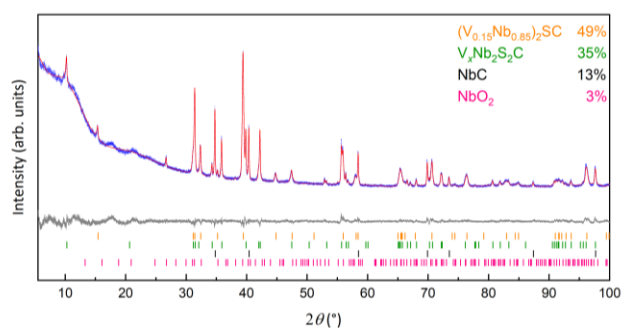


Figure A-71: X-ray powder pattern of $(V_{0.15}Nb_{0.85})_2SC$ (blue) with Rietveld fit (red) and difference curve (gray).

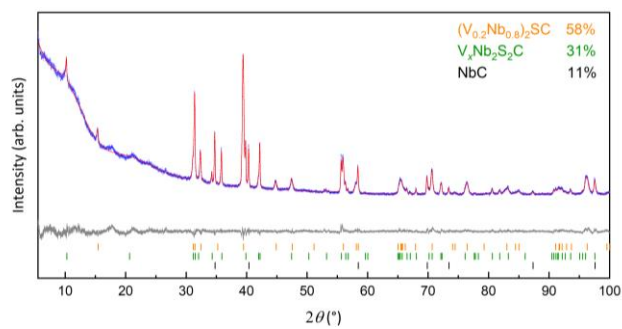


Figure A-72: X-ray powder pattern of $(V_{0.2}Nb_{0.8})_2SC$ (blue) with Rietveld fit (red) and difference curve (gray).

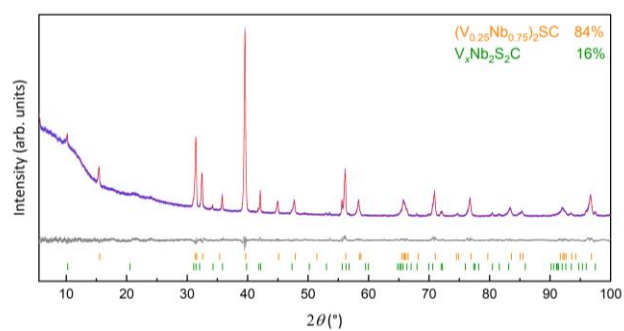


Figure A-73: X-ray powder pattern of $(V_{0.25}Nb_{0.75})_2SC$ (blue) with Rietveld fit (red) and difference curve (gray).

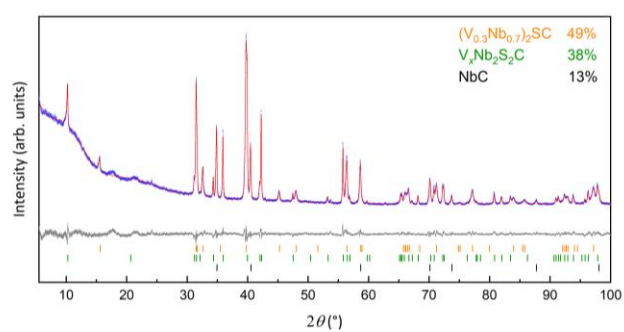


Figure A-74: X-ray powder pattern of $(V_{0.3}Nb_{0.7})_2SC$ (blue) with Rietveld fit (red) and difference curve (gray).

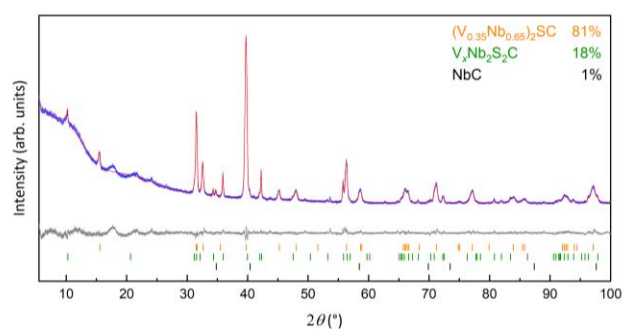


Figure A-75: X-ray powder pattern of $(V_{0.35}Nb_{0.65})_2SC$ with Rietveld fit (red) and difference curve (gray).

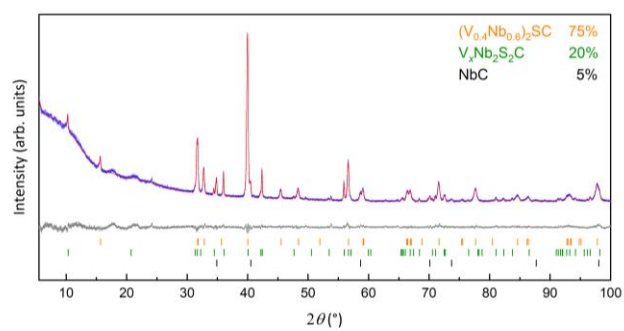


Figure A-76: X-ray powder pattern of $(V_{0.4}Nb_{0.6})_2SC$ (blue) with Rietveld fit (red) and difference curve (gray).

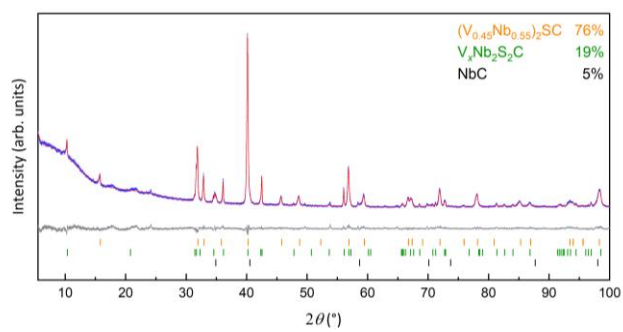


Figure A-77: X-ray powder pattern of $(V_{0.45}Nb_{0.55})_2SC$ (blue) with Rietveld fit (red) and difference curve (gray).

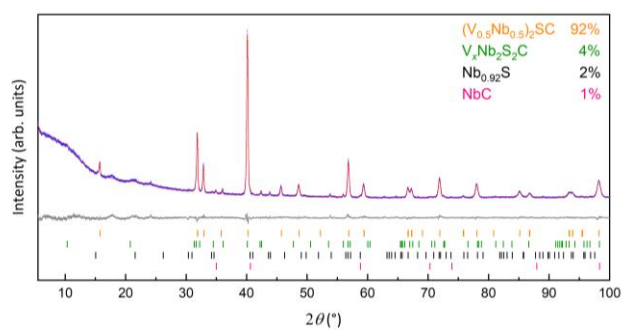


Figure A-78: X-ray powder pattern of $(V_{0.5}Nb_{0.5})_2SC$ (blue) with Rietveld fit (red) and difference curve (gray)

A. 4 Rietveld refinement and magnetic measurements of M_3P_2C ($M = Nb, Ta$)

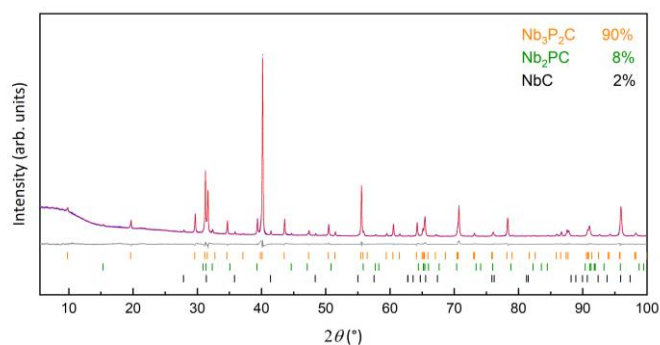


Figure A-79: X-ray powder pattern of Nb_3P_2C (blue) with Rietveld fit (red) and difference curve (gray).

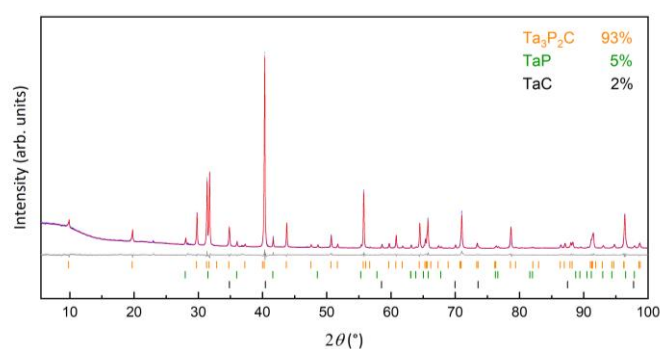


Figure A-80: X-ray powder pattern of Ta_3P_2C (blue) with Rietveld fit (red) and difference curve (gray).

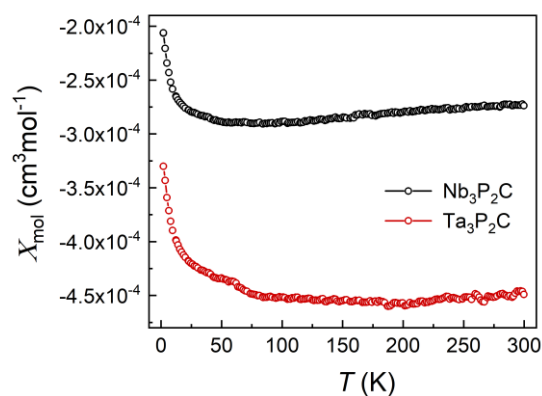


Figure A-81: Molar susceptibility of M_3P_2C ($M = Nb, Ta$) at an applied field of 30 kOe in the temperature range 2 – 300 K.

References

- [1] G. Kresse, J. Hafner, *Phys. Rev. B: Condens. Matter* **1993**, *47*, 558-561.
- [2] G. Kresse, J. Hafner, *Phys. Rev. B: Condens. Matter* **1994**, *49*, 14251-14269.
- [3] G. Kresse, J. Furthmüller, *Comput. Mater. Sci.* **1996**, *6*, 15-50.
- [4] J. P. Perdew, K. Burke, M. Ernzerhof, *Phys. Rev. Lett.* **1996**, *77*, 3865-3868.
- [5] J. P. Perdew, K. Burke, M. Ernzerhof, *Phys. Rev. Lett.* **1997**, *78*, 1396-1396.
- [6] J. P. Perdew, A. Ruzsinszky, G. I. Csonka, O. A. Vydrov, G. E. Scuseria, L. A. Constantin, X. Zhou, K. Burke, *Phys. Rev. Lett.* **2008**, *100*, 136406.
- [7] P. E. Blöchl, *Phys. Rev. B: Condens. Matter* **1994**, *50*, 17953-17979.
- [8] G. Kresse, D. Joubert, *Phys. Rev. B: Condens. Matter* **1999**, *59*, 1758-1775.
- [9] V. L. Deringer, R. P. Stoffel, A. Togo, B. Eck, M. Meven, R. Dronskowski, *CrystEngComm* **2014**, *16*, 10907-10915.
- [10] A. Togo, I. Tanaka, *Scripta Mater.* **2015**, *108*, 1-5.

Scientific Contributions

Publications

Syntheses and physical properties of the MAX phase boride Nb₂SB and the solid solutions Nb₂SB_xC_{1-x} (x = 0 – 1)

T. Rackl, L. Eisenburger, R. Niklaus, and D. Johrendt

Physical Review Materials, **2019**, *3*, 054001

For this publication, synthesis and sample preparation of Nb₂SB_xC_{1-x} (x = 0 – 1), powder X-ray diffraction, Rietveld refinement, magnetic measurements, resistivity measurements and data analysis were performed by Tobias Rackl. The STEM-HAADF imaging was performed by Lucien Eisenburger. DFT calculations were done by Robin Niklaus and Dirk Jobrendt. The manuscript was written by Tobias Rackl and Dirk Jobrendt.

The MAX phase borides Zr₂SB and Hf₂SB

T. Rackl, and D. Johrendt

Soild State Sciences, **2020**, *106316*

Synthesis and sample preparation of Zr₂SB and Hf₂SB, powder X-ray diffraction, Rietveld refinement, magnetic and resistivity measurements, as well as data analysis were done by Tobias Rackl. DFT calculations were performed by Dirk Jobrendt. The manuscript was written by Tobias Rackl and Dirk Jobrendt.

Alkali chalcogenido ortho manganates(II) A_6MnQ_4 ($A = Rb, Cs$; $Q = S, Se, Te$)

M. Langenmaier, T. Rackl, D. Johrendt, and C. Röhr

Zeitschrift für Naturforschung B, **2018**, *73*, 837 – 848

For this publication, synthesis and sample preparation of A_6MnQ_4 ($A = Rb, Cs$; $Q = S, Se, Te$), single crystal X-ray diffraction, powder X-ray diffraction, Rietveld refinement and data evaluation were done by Micheal Langenmaier. Magnetic measurements were performed and interpreted by Tobias Rackl and revised by Dirk Johrendt. The manuscript was written by Micheal Langenmaier and Carolin Röhr.

Solid Solutions of Grimm–Sommerfeld Analogous Nitride Semiconductors $II-IV-N_2$ ($II = Mg, Mn, Zn$; $IV = Si, Ge$): Ammonothermal Synthesis and DFT Calculations

M. Mallmann, R. Niklaus, T. Rackl, M. Benz, T. G. Chau, D. Johrendt, J. Minár, and W. Schnick

Chemistry A European Journal, **2019**, *25*, 15887

Sample syntheses and analyses were performed by Mathias Mallmann with assistance of Maximilian Benz and Thanh Giang Chau. DFT calculations and evaluation of the data were conducted by Robin Niklaus and Ján Minár. Tobias Rackl performed and interpreted the magnetic measurements and supervision of Dirk Johrendt. The manuscript was written by Mathias Mallmann and Robin Niklaus, and revised by Wolfgang Schnick.

Conference contributions

Eisenantimonide [talk]

T. Rackl

2. Obergurgl-Seminar Festkörperchemie, Obergurgl, Austria, **2016**

Superconductivity in the solid solution $\text{Nb}_2\text{As}_x\text{S}_{1-x}\text{C}$ ($x = 0 - 1$) MAX-phases

[*poster*]

T. Rackl, S. Baumann, and D. Johrendt

16th European Conference on Solid State Chemistry, Glasgow, UK, **2017**

Substitution in Nb MAX-Phasen [*talk*]

T. Rackl, S. Baumann

3. Obergurgl-Seminar Festkörperchemie, Obergurgl, Austria, **2018**

Substitution in Nb MAX-Phasen [*talk*]

T. Rackl, S. Baumann

47. Hirschegg Festkörperchemiesymposium, Hirschegg, Austria, **2018**

 $\text{Nb}_3\text{P}_2\text{C}_2$ – Das beste 2D-Netz [*talk*]

T. Rackl

4. Obergurgl-Seminar Festkörperchemie, Obergurgl, Austria, **2019**

MAX und BORitz [*talk*]

T. Rackl, M. Pfeiffer, L. Eisenburger, and D. Johrendt

5. Obergurgl-Seminar Festkörperchemie, Obergurgl, Austria, **2020**